UNIVERSITY OF CALIFORNIA

Los Angeles

Scale-up characteristics of salinity gradient power technologies

A dissertation submitted in partial satisfaction

of the requirements for the degree Doctor of Philosophy

in Civil Engineering

by

Benjamin Jacob Feinberg

2014

ABSTRACT OF THE DISSERTATION

Scale-up Characteristics of Salinity Gradient Power Technologies

by

Benjamin Jacob Feinberg

Doctor of Philosophy in Civil Engineering

University of California, Los Angeles, 2014

Professor Eric M. V. Hoek, Chair

Salinity gradient power (SGP), the controlled mixing of streams with different salinity, is a potential route for clean and renewable base-load power generation. The two most popular forms of SGP production, pressure retarded osmosis (PRO) and reverse electrodialysis (RED), have received renewed research interest in recent years. While previous modeling work has focused on the application of simple mathematical models to these processes, in order to accurately predict process performance on scale-up, robust models must be developed. The objective and focus of this dissertation is to understand through mathematical modeling the practical performance that can be achieved in PRO and RED as the technology transitions from the laboratory scale to full-scale implementation.

First, the thermodynamics of mixing are discussed for both PRO and RED, with the intrinsic differences highlighted for each process. Using simple thermodynamic models, the integration of PRO and RED with reverse osmosis (RO) is discussed as a method for reducing the specific energy consumption (SEC) of seawater desalination. This "osmotic energy

recovery" (OER) is evaluated in a seawater RO plant that includes state-of-the-art RO membranes, plant designs, operating conditions, and hydraulic energy recovery (HER) technology. We assume the use of treated wastewater effluent as the OER dilute feed, which may not be available in suitable quality or quantity to allow operation of the coupled process. A two-stage OER configuration could reduce the SEC of seawater RO plants to well below the theoretical minimum work of separation for state-of- the-art RO-HER configurations with a breakeven OER capital expenditure (CAPEX) equivalent to 42% of typical RO-HER plant cost suggesting significant cost savings may also be realized. At present, there is no commercially viable OER technology; hence, the feasibility of using OER at seawater RO plants remains speculative, however attractive.

In order to probe scale up characteristics of SGP, a process model has been developed for PRO accounting for full-scale system losses such as viscous dissipation, external mass transfer and equipment efficiency. Also, an existing model for RED is adapted to account for analogous full-scale systems losses. We project practical power densities and process efficiencies. The projected power density for PRO (using best available membranes) is much lower than generally predicted by extrapolation of experimental data. For example, a power density of 5 W/m^2 extrapolated from laboratory experiments actually yielded negative power at full-scale. Hydraulic energy recovery device (HER) efficiency doubles the maximum power density for HER efficiency increase from 90% to 99%. Furthermore, the operating pressure, load voltage, and crossflow velocities typically applied in laboratory studies appear much too high to be practical in full-scale PRO and RED systems. RED systems should be designed with relatively short lengths compared to PRO. For both processes, energy efficiency does not occur at thermodynamic equilibrium due to hydraulic losses. Finally, maximum power density appears

an inadequate parameter for assessing full-scale PRO/RED process feasibility because both processes could produce the same maximum power density, but different power outputs and efficiencies with different system sizes.

While there has been a significant amount of laboratory work focused on improving membrane performance in PRO, there has been little emphasis on developing novel PRO process configurations that might dramatically improve overall process performance. Here, we introduce a novel PRO configuration and apply the developed process model in order to evaluate the performance of the process. This "staged" configuration has the potential to dramatically improve the performance of PRO with up to 33% higher water flux over the standard PRO configuration. In this new arrangement, intermodule hydroturbines are placed strategically in order to modulate the applied pressure over the length of the system. The additional hydroturbines match the applied pressure to the optimum flux condition over each segment and substantially increase the total water recovery. The impact on energy efficiency is significant for some mixing regimes, with seawater-river water and brine-river water mixing corresponding to efficiency increases from 31% to 44% and 34% to 50%, respectively, versus the standard PRO configuration. Of course, performance improvements must be considered in light of the increased capital costs arising from the additional hydroturbines.

Finally, the PRO process model is integrated with cost data in order to determine the change in energy production cost with system size. Since existing cost correlations from the literature are often outdated, new correlations have been developed for each plant component by contacting suppliers and manufacturers. Linking these correlations with power output data, energy cost has been evaluated under different operating conditions and with membrane properties. The results suggest that there is still significant room for improvement in membrane

design in order to further reduce the cost of PRO. Furthermore, from an economic perspective, brine-river water mixing appears to be a much more promising mixing regime than seawater-river mixing.

The dissertation of Benjamin Jacob Feinberg is approved.

Shaily Mahendra

Keith D. Stolzenbach

Richard B. Kaner

Eric M.V. Hoek, Committee Chair

University of California, Los Angeles

2014

Table of Contents

List of Figures

List of Tables

ACKNOWLEGEMENTS

I would first like to thank my advisor, Prof. Eric Hoek, for his insight and encouragement. His advice and guidance have been an invaluable part of my growth as a researcher. I also would like to thank the other members of my doctoral committee, including Prof. Shaily Mahendra, Prof. Keith Stolzenbach, and Prof. Richard Kaner. Thank you also to Prof. Diana Huffaker and the other faculty in the Clean Energy for Green Industry (CGI) IGERT program.

I am particularly grateful to Dr. Guy Ramon, who started as a post-doc in our lab as I began my PhD journey four years ago. His mentorship and guidance have made me a much wiser and more confident researcher.

Special thanks to my current and former colleagues: Dr. Jinwen Wang, Dr. Mavis Wong, Dr. MaryTheresa Pendergast, Dr. Catalina Marambio Jones, Brian McVerry and Dukwoo Jun. I will always have fond memories of the laughs, academic exchanges, and fun times we shared during my time at UCLA. Thanks also to Drs. Gregory Guillen and Gil Hurwitz, both of whom provided good humor and good advice to a new doctoral student.

I would like to thank my partner, JD Barton, for his love and understanding as I worked late nights and long weekends. Most of all, I would to thank my parents and brothers for their constant encouragement, support, and wisdom. From a young age, they fostered a strong sense of intellectually curiosity in me, and for that I will be forever grateful.

Financial support was provided by a scholarship from the National Science Foundation through the Clean Energy for Green Industry (CGI) IGERT and by the UCLA Henry Samueli

School of Engineering and Applied Science and Department of Civil and Environmental Engineering.

This document contains content from currently published and in preparation research articles. I am first author on all articles with the exception of **Chapter 1**, where Dr. Guy Z. Ramon is listed as first author. The article information is as follow: G.Z. Ramon, B.J. Feinberg, and E.M.V. Hoek, "Membrane-based production of salinity gradient power," *Energy and Environmental Science*, 4 (2011) 4423-4434. I would like to acknowledge his work here, and to note that I have received his consent to use content from this article for this dissertation. My contribution to the relevant article focused primarily on the modeling of the RED process. Please note that, in parts, I have modified the text from the original publication. Since the chapter is a modified version of the journal article, text, figures, and charts are used directly without further citation here.

Chapters 2, **3** and **4,** are based on published, submitted, or in preparation journal articles as follows: B.J. Feinberg, G.Z. Ramon and E.M.V. Hoek, "Thermodynamic analysis of osmotic energy recovery at a reverse osmosis desalination plant," *Environmental Science and Technology*, 47 (2013) 2982–2989. (Chapter 2); B.J. Feinberg, G.Z. Ramon, and E.M.V. Hoek, "Scale-up characteristics of membrane-based salinity-gradient power production," *Journal of Membrane Science*, submitted. (Chapter 3); B.J. Feinberg, G.Z. Ramon, and E.M.V. Hoek, "Toward improving pressure retarded osmosis efficiency," *Environmental Science and Technology Letters*, in preparation. (Chapter 4);

Chapter 5 contains cost data gathered by a current Master's student at Imperial College London, David Debash. David and I worked together on the development of the cost analysis for PRO, and I would like to acknowledge his contribution to the work. I would also like to thank

Holly Johnson and Lisa Henthorne, of Water Standard, for their guidance and advice on reverse osmosis costing.

VITA

2007	B.S. Environmental Engineering Science Massachusetts Institute of Technology (MIT) Cambridge, MA
2008	MSc Environmental Engineering Imperial College London London, UK
2008 – 2010	Environmental Services Engineer Arup London, UK
2010-2013	Graduate Fellow Clean Energy for Green Industry (CGI) IGERT National Science Foundation
2010-2013	Graduate Student Researcher Department of Civil and Environmental Engineering University of California, Los Angeles Los Angeles, California
2012	Teaching Assistant Department of Civil and Environmental Engineering University of California, Los Angeles Los Angeles, California

PUBLICATIONS AND PRESENTATIONS

B.J. Feinberg, G.Z. Ramon, and E.M.V. Hoek, "Toward improving pressure retarded osmosis efficiency," *Environmental Science and Technology Letters*, **in preparation.**

B.J. Feinberg, G.Z. Ramon, and E.M.V. Hoek, "Scale-up characteristics of membrane-based salinity-gradient power production," *Journal of Membrane Science*, **submitted.**

G.R. Guillen, B.T. McVerry, **B.J. Feinberg**, T.P. Farrell, Q.Wei, B.R. Mattes, R.B. Kaner, and E.M.V. Hoek, "Tuning the properties of polyaniline-based ultrafiltration membranes with chemical post-treatments," *Journal of Membrane Science*, **in preparation.**

B.J. Feinberg, G.Z. Ramon and E.M.V. Hoek, "Thermodynamic analysis of osmotic energy recovery at a reverse osmosis desalination plant," *Environmental Science and Technology*, 47 (2013) 2982–2989.

B.J. Feinberg, E.M.V Hoek, "Interfacial polymerization," Encyclopedia of Membrane Science & Technology, E.M.V. Hoek and V.V. Tarabara (Eds.), John Wiley & Sons, 2013

B.J. Feinberg, G.Z. Ramon, and E.M.V. Hoek, "Reducing energy costs at a seawater RO plant using coupled salinity gradient power," International Desalination Association (IDA) World Congress 2013, Tianjin, China, October 20 – 25, 2013, *oral presentation*.

B.J. Feinberg, G.Z. Ramon, and E.M.V. Hoek, "Modeling the relationship between power density and energy recovery in large – scale application of salinity gradient energy technologies," North American Membrane Society (NAMS) Meeting 2013, Boise, ID, June 9 – 12, 2013, *oral presentation*.

B.J. Feinberg and E.M.V. Hoek, "Structure-performance relationships for osmotic membranes: comparing theory to reality," Advanced Membrane Technology V, Singapore, October 14 – 19, 2012, *oral presentation*.

B.J. Feinberg, G.Z.Ramon, and E.M.V. Hoek, "Production of energy using salinity gradients," Renewable and Sustainable Energy Technology (ReSET) Conference 2013, Los Angeles, CA, April 12 – 13, 2012, *poster presentation*.

B.J. Feinberg, G.Z. Ramon, and E.M.V. Hoek, "Membrane-based production of salinity gradient power," Gordon Research Conference on Membranes: Materials & Processes, New London, NH, July 29 – August 2, 2012, *poster presentation*.

G.Z. Ramon, **B.J. Feinberg**, and E.M.V. Hoek, "Membrane-based production of salinity gradient power," *Energy and Environmental Science*, 4 (2011) 4423-4434.

H. Lateef, S. Grimes, P. Kewcharoenwong and **B.J. Feinberg**, "Separation and recovery of cellulose and lignin using ionic liquids: a process for recovery from paper-based waste," *Journal of Chemical Technology and Biotechnology*, 84 (2009) 1818-1827, I.F. 2.504.

1 INTRODUCTION

1.1 General introduction

The need for renewable, environmentally benign energy is widely recognized, and hence, massive efforts are being exerted globally to develop new 'green energy' sources including: wind, solar, geothermal, biomass, ocean thermal, wave, and tidal. Interest in renewable energy stems from both the perceived supply-side risk of the fossil fuels energy supply and the potential environmental impact of fossil fuel extraction, processing, and use [1]. Furthermore, increasing awareness of climate change has prompted extensive research into technologies that do not emit greenhouse gases through combustion. Still, potential drawbacks to many forms of renewable energy include intermittency (i.e. many technologies provide a variable output and must include some form of energy storage) and high cost.

Salinity gradient power (SGP) is the power available from mixing two aqueous solutions of different salinities, such as river water and seawater. The global estimated production potential for SGP is significant, and has been estimated at 1.4–2.6 TW [2, 3], a value derived from the mixing of major rivers with seawater. Of course, while it is impossible to practically recover all of this energy, there has been a significant and focused research effort to develop the technology to exploit the energy from mixing. In 2009, a Norwegian utility called Statkraft revealed the first demonstration of a 10kW salinity-gradient power plant [4]. While Statkraft has since abandoned the SGP program, their work highlights the scale of the development effort.

Importantly, salinity gradient power is not intermittent in nature and has the ability to function continuously, supplying constant output power. Different techniques exist for the recovery of energy from the mixing of varied salinity flows. These technologies include reverse electrodialysis (RED) [4-6], pressure retarded osmosis (PRO) [7, 8], capacitive mixing [9, 10], and mixing in ion selective nano-channels[11]. Recently, a microbially-assisted RED process has

been developed that simultaneously treats wastewater, produces desalinated water, and generates electricity[12, 13].

1.2 Background and related research

Much of **Sections 1.2** and **1.3** is taken directly or modified from a published journal article for which I am listed as a co-author. Further details are included in the Acknowledgments section at the beginning of this dissertation.

1.2.1 Salinity gradient power fundamentals

1.2.1.1 Free energy of mixing

If two solutions with different molecular compositions are brought into contact, they will spontaneously mix, and the difference in free energy upon mixing of two solutions is the sum of the chemical potentials of the original, unmixed solutions minus the chemical potential of the final mixture. Assuming constant pressure and temperature, the free energy of mixing is

$$\Delta G_{mix} = 2RT\left(c_c \ln\frac{c_c(1+\phi)}{c_c + c_d\phi} + \phi c_d \ln\frac{c_d(1+\phi)}{c_c + c_d\phi} \right) \tag{1.1}$$

where R is the universal gas constant, T is temperature, V is volume, c is concentration, subscripts c and d refer to the concentrated and dilute solutions, respectively, and $\phi = V_d/V_c$ is the dilution ratio. This equation implies that more energy is released from the mixing of solutions that exhibit a larger concentration difference, and that linear changes in concentration do not result in a linear change in the free energy of mixing.

1.2.1.2 Pressure-retarded osmosis

The two most prominent forms of SGP include pressure-retarded osmosis (PRO) and reverse electrodialysis (RED). These technologies are theoretically the reverse of two very common water treatment tecnhnolgoies, reverse osmosis (RO) and electrodialysis (ED) desalination. Originally developed in the 1970s [14, 15], in PRO water molecules diffuse across a membrane from a high chemical potential (dilute) solution into a pressurized, low chemical potential (concentrated) solution. The concentrated solution, which now comprises the original concentrated solution flow as well as the permeate flow, is passed through a hydroturbine in order to generate electricity. **Figure 1.1** depicts the PRO process as typically envisioned.

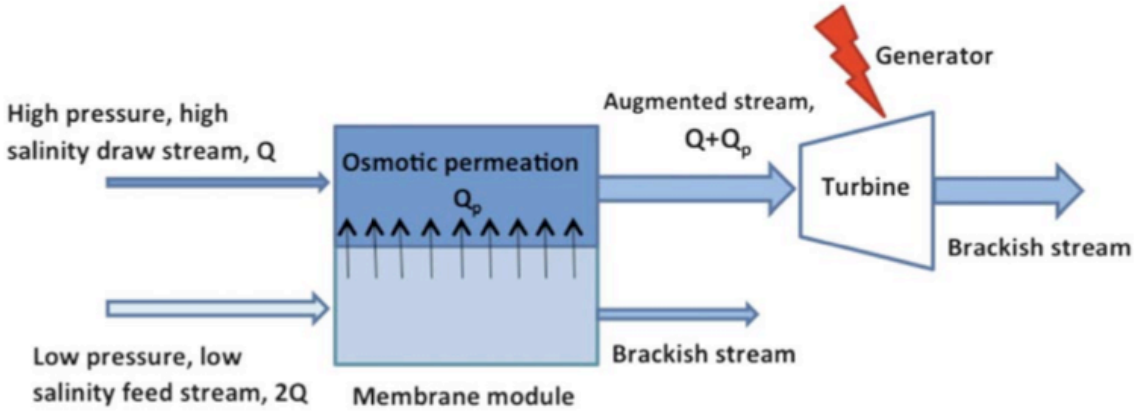

Figure 1.1 Schematic representation of the PRO process.

1.2.1.3 Reverse electrodialysis

In RED, alternating concentrated and dilute streams are separated by ion exchange membranes. Diffusion of counter-ions across theses ion exchange membranes occurs due to the concentration difference across each membrane. This ionic flux across membranes is converted into an electron flux at electrodes, and power is dissipated through an external load. An RED stack consists of many pairs of low concentration and high concentration flow channel pairs separated by anion

and cation exchange membranes. **Figure 1.2** depicts the RED process as it is typically envisioned.

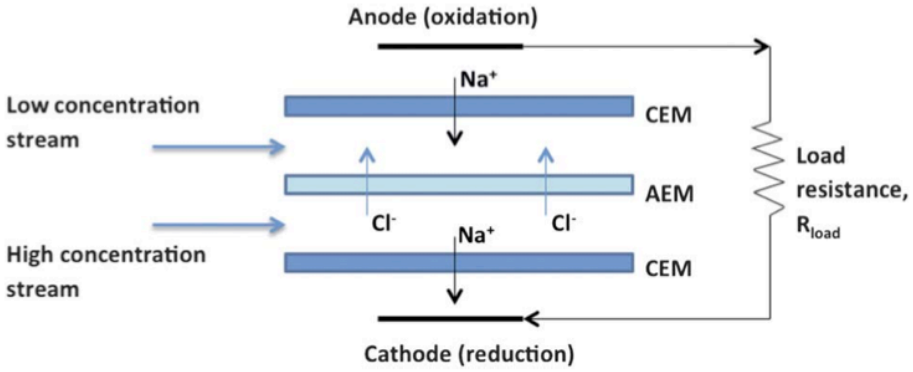

Figure 1.2 Schematic representation of the RED process.

1.2.2 Governing equations

1.2.2.1 PRO

The driving force for water flux (osmosis) in PRO is the chemical potential difference across a semipermeable membrane. Assuming an isothermal system, the water flux is correlated to the driving force (osmotic pressure difference across the membrane, $\Delta\pi = 2RT(c_c - c_d)$) minus the applied hydraulic pressure difference (ΔP), multiplied by the water permeability value for the membrane itself (A) [14, 15], i.e.

$$J_w = A(\Delta\pi - \Delta P)\,. \tag{1.2}$$

In **Eq.** 1.2, the applied pressure diminishes the driving force for water flux across the membrane, hence the terminology pressure *retarded* osmosis.

In an ideal sense, the power generated from the hydroturbine is the permeate flow multiplied by the applied pressure. The power density, that is the power generated per unit of membrane area, is therefore

$$W = J_w \Delta P = A(\Delta\pi - \Delta P)\Delta P \,. \tag{1.3}$$

Note that this power density does not take into account inefficiencies in equipment or viscous dissipation. Through a simple differentiation of **Eq.** 1.3 with respect to ΔP, the maximum power density achievable can be calculated as

$$W_{max} = \frac{A}{4}\Delta\pi^2 \,. \tag{1.4}$$

It is clear from **Eq.** 1.4 that the maximum power density is a function of only the osmotic pressure difference between the two solutions and the membrane hydraulic permeability. While the maximum power density of the process can be most dramatically improved by increasing the concentration difference between the dilute and concentrated solutions, the membrane permeability remains a critically important design parameter with significant impact on process performance.

1.2.2.2 RED

While the goal of both PRO and RED is to recover energy from the mixing of two solutions of different molecular composition, the operating principle of each is decidedly different. While PRO is a hydraulic process involving the diffusion of water molecules (J_w) across a semipermeable membrane, RED is an electrochemical process which depends on ion diffusion (J_s) [16]. Still, the governing equations are direct analogues, albeit here the driving force can be defined as the potential difference across the membranes (ΔE), instead of the osmotic pressure difference, as follows

$$\Delta E = \frac{2\alpha R_g T}{F} \ln \frac{c_c}{c_d} \tag{1.5}$$

where α is the ion exchange membrane permselectivity (i.e. the relative preference for counter-ions), and F is the Faraday constant relating electron flux to ion flux. Note that **Eq.** 1.5 refers to the total driving force across two membranes and therefore includes a factor of 2 to represent one "cell pair" accounting for both dilute and concentrated flow channels. Many cell pairs can be placed in parallel to form a larger *stack*, and the total potential difference is then multiplied by the number of cell pairs. The load voltage (ΔV), analogous to the hydraulic pressure in PRO, is the product of the ion flux (J_s) times the load resistance (R_{load}), i.e. $\Delta V = R_{load} J_s F$. The salt flux can be determined through

$$J_s = K(\Delta E - \Delta V) \tag{1.6}$$

where K is the membrane conductivity for salt ions and can be defined as $K = 1/R_{stack}F$, where R_{stack} is the stack resistance. The stack resistance,

$$R_{stack} = R_{aem} + R_{cem} + \frac{h_c}{\kappa_c} + \frac{h_d}{\kappa_d} + R_{electrode} \tag{1.7}$$

is the sum of the anion exchange membrane resistance (R_{aem}), the cation exchange membrane resistance (R_{cem}), the two channel resistances where h_d is the dilute feed channel height, h_c is the concentrated feed channel height, κ_c the concentrated feed conductivity, and κ_d the dilute feed conductivity. As with the potential difference, stack resistance scales with the size of the stack (i.e. the number of cell pairs). Electrode resistance, $R_{electrode}$, is typically assumed to be negligible for a stack containing a large number of cell pairs. As with PRO, the power density is a simply the flux multiplied by the load (here voltage instead of pressure),

$$W = \frac{1}{2R_{stack}}(\Delta E - \Delta V)\Delta V \tag{1.8}$$

and the maximum power density can be calculated as

$$W_{max} = \frac{1}{2R_{stack}}\frac{\Delta V^2}{4} \tag{1.9}$$

through a simple differentiation of the power density equation. Note that in **Eq.** 1.9 we divide by a factor of 2 to account for the two membranes in one cell pair.

1.2.3 Mass transfer limitations

1.2.3.1 PRO

While increasing the osmotic pressure difference is an easy route to improving power density, mass transfer limitations such as concentration polarization (CP) lead to decreased mixing efficiency. While external CP is certainly present in RO and other membrane-based processes, PRO uniquely exhibits both external and *internal* CP phenomena. The external CP manifests itself as 'dilutive external CP,' whereby water flux across the membrane dilutes the interface concentration in the concentrated solution, reducing the overall driving force for permeation. This effect is the opposite to what is observed in RO, where the interface concentration in the concentrated solution is heightened relative to the bulk concentration.

On the other hand, internal CP occurs due to the diffusion of salt into the dilute solution from the concentrated solution ('salt leakage'), as well as accumulation of rejected salt at the dilute-side membrane interface [17, 18]. The structure of PRO membranes heightens the impact

of internal CP, which were developed using similar methods employed in RO membrane fabrication. To form these thin film composite (TFC) membranes, a very dense, highly rejecting polyamide active layer (~100 nm) is grown on a porous, ultrafiltration membrane support (~50 microns). The dense surface layer of the ultrafiltration support membrane precludes rapid diffusion of accumulated salt at the dilute-side active layer interface into the bulk. **Figure 1.3** depicts internal and external CP as they apply to a PRO membrane with the active layer facing the concentrated solution (draw).

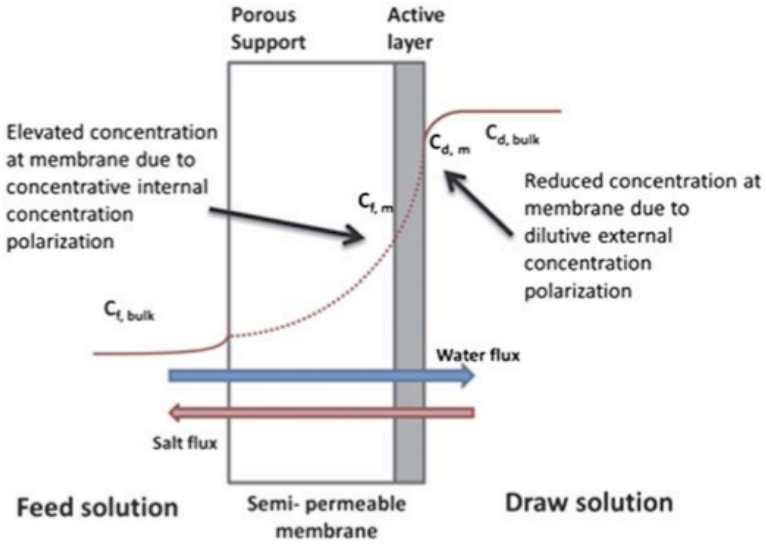

Figure 1.3 Schematic drawing illustrating internal and external concentration polarization when an asymmetric membrane is used for pressure retarded osmosis.

Applying film theory, the *actual* osmotic pressure difference across the membranes can be defined as [7, 17]

$$\Delta\pi = 2RT(c_{m,c} - c_{m,d}) = 2RT\left(\frac{c_{b,c}exp\left(\frac{-J_w}{k}\right) - c_{b,d}exp\left(\frac{J_w S}{D}\right)}{1+\frac{B}{J_w}\left(exp\left(\frac{J_w S}{D}\right)-1\right)}\right) \tag{1.10}$$

where k is the mass transfer coefficient, B is the salt permeability coefficient, an intrinsic membrane property, k is the mass transfer coefficient, D is the diffusion coefficient for salt, S is the structure factor, and subscript b and m refer to the bulk and membrane interface conditions, respectively. The structure factor is a property of the porous ultrafiltration support of the membrane, and can be defined as

$$S = \frac{\tau\delta}{\epsilon} \tag{1.11}$$

where ϵ , τ and δ are the porosity, tortuosity, and thickness of the support membrane, respectively. Since the structure factor increases the effective diffusion path length for salt and water, a significant amount of research work has been conducted in order to reduce this membrane parameter [18] In film theory as applied in **Eq.** 1.10, the external mass transfer coefficient is used to relate bulk concentration to membrane interface concentration. The value of this coefficient varies depending on channel dimensions and flow conditions, but here we assume an RO like configuration (spacer filled channel), and use the following correlation [19] which was developed using a computation fluid dynamics approach

$$k = 0.46(\mathrm{ReSc})^{0.36}\frac{D}{d_h}. \tag{1.12}$$

Here Sc is the Schmidt number (the ratio of viscous diffusion to molecular diffusion forces), Re is the Reynolds number (the ratio of inertial forces to viscous forces), and d_h is the flow channel hydraulic diameter. Reynolds number itself is a function of the fluid velocity, and therefore increased crossflow velocity will increase the mass transfer coefficient, and decrease the degree of external concentration polarization. Similarly, reducing the channel hydraulic diameter

through decreasing the channel height will also improve mixing within the flow channel. Of course, in a real process, there is a tradeoff between optimization of the mass transfer coefficient and reduction of viscous dissipation in the flow channel.

1.2.3.2 RED

As with PRO, concentration polarization is a major source of process inefficiency in RED. The membrane interface concentration can be related to the bulk concentration through $c_m = c_b \pm J_s/k$, where subscripts b and m refer to the bulk and membrane interface conditions, respectively. Therefore, the real potential difference, accounting for concentration polarization, can be written as

$$\Delta E = 2\frac{\alpha R_g T}{F}\ln\frac{c_c - J_s/k}{c_d + J_s/k}. \tag{1.13}$$

While losses such as co-ion transport and electro-osmosis have been found to have limited impact on process efficiency, especially at higher current densities [20], other losses significantly reduce the power densities achievable in RED. These other effects include spacer effects, electrode losses, and multivalent ion effects. Spacers are used to maintain constant flow channel height as well as to limit the impact of concentration polarization by promoting mixing. However, the presence of spacers in the flow channel also promotes increased viscous dissipation. Furthermore, spacers can interfere with the transport of ions through the membranes, reducing the effective surface area for ion diffusion. Previous work has shown that this ‘‘shadow effect’’ can reduce process efficiency by up to 40% [6]. In order to reduce the impact of spacers, Dlugolecki et al. developed *conductive spacers* designed to increase the effective area for ion

transport [21]. These spacers, created using both an anion-conducting part and a cation-conducting part, increased power density by nearly 400%.

Electrode losses have been shown to have limited impact on process performance [22]. However, improvement in electrode configuration through the use of segmented electrodes can significantly improve overall process efficiency. Veerman et al. showed that segmented electrodes, which allow for different load resistances over the length of the stack, significantly improve power output in RED [4]. The impact of segmentation on power output increased with longer resistance time (i.e. greater extent of mixing).

RED laboratory studies typically use single solute solutions in testing stack performance. Recently, however, a study showed that the multivalent ions in the feed solution can decrease power output through increased stack resistance [23]. In order to prevent the diffusion of these multivalent ions against the electrochemical potential gradient, monovalent selective membranes can be chosen.

1.2.4 Current state-of-the-art

1.2.4.1 PRO

Most of the recent work on PRO has focused on improving membrane technology. This work has included the development of bespoke laboratory-developed membranes [24-28] as well as the testing of commercially available RO and forward osmosis (FO) membranes [7, 17, 18, 29, 30]. Experimental efforts have been primarily limited to small, laboratory scale systems, although a commercial FO spiral-wound module was recently tested in PRO mode [31]. The maximum power densities reported in the literature as inferred from experimental measurements, using seawater-equivalent as the concentrated stream, are ~0.5 W/m^2 in a commercially available

spiral-wound module (Hydrowell, Hydration Technology Innovations Inc., Albany, Oregon, USA) [31] 2.7 W/m^2 with the same commercial membrane lab-tested [7], and 3.5 W/m^2 with a prototype, lab-cast TFC membrane [24].

There has been significant progress made recently in the fabrication of FO membranes. While these were not specifically tested for PRO operation (e.g., permeation rates under pressurized conditions), their estimated potential performance may be calculated based on the experimentally determined characteristics, namely, the water and salt permeabilities and the structure factor of the support. **Table 1.1** provides a compilation of FO membranes, their reported characteristics and projected power densities, calculated using **Eq** 1.9 and 1.10. Power calculations were made assuming the concentrated solution is either seawater or seawater RO brine after 50% recovery (0.55 M and 1.1 M as NaCl, respectively) and that the dilute stream has a concentration of 0.005 M, representative of river water, or 0.02 M, representative of wastewater, and the Reynolds number was taken to be 100, which may be considered as a representative value for operation of spiral-wound membrane modules.

The membrane with the best structure factor reported thus far is a cellulose-acetate phase-inversion membrane with a thickness of ~35 mm and a structure factor of ~50 mm [28], followed by ~310 mm reported for a thin-film composite polyamide/polysulfone membrane [25], which along with its relatively high permeability (~5.3×10^{-12} m s^{-1} Pa^{-1}) has the highest projected performance at 6.1 W/m^2 and 15.3 W/m^2 for seawater and RO brine, respectively, serving as the concentrated solution. The highest reported permeability is ~7×10^{-12} m s^{-1} Pa^{-1} [24], also for a composite membrane, which is about double that of the average commercial seawater RO membrane. The current generation of prototype membranes, particularly those recently reported by Tiraferi et al. [25], already achieve the ~5 W/m^2 power density which has been flagged as the

target for making PRO economically viable [32]. That being said, this power density is idealized and is expected to be significantly lower in practice, primarily due to dilution effects and hydraulic losses, as previously discussed. It is particularly curious to note the lack of a definitive correlation between the structure factor and estimated power output; this will be discussed further in the following section.

An important characteristic of any PRO membrane is its ability to withstand the applied hydraulic pressure in the feed stream. Since a maximum power output is achieved when this applied pressure is about half the osmotic pressure, it follows that the higher the concentration difference (larger energy source), the higher the necessary applied pressure for power maximization. For example, when RO brine (1.1M, twice the concentration of seawater) is contacted with 0.02M wastewater, the optimum applied pressure would be ~24 bar. It is not clear whether the currently available membranes, as compiled in **Table 1.1**, would be able to mechanically withstand such an applied pressure

1.2.4.2 RED

The reported characteristics of a number of commercially available ion-exchange membranes are shown in **Table 1.2**. Most of the commercially available membranes are homogenous, that is, fabricated solely from the ion-exchange polymer. Lower performance, heterogeneous membranes are also available, to a much lesser extent; these are fabricated using mixed ratios of ion-exchange polymer with another, inert, polymeric carrier. While achieving permselectivity comparable with that of homogeneous membranes, heterogeneous membranes are 3–4 times less ion-conductive.

Veerman et al. [20] benchmarked six cation-anion membrane pairs and found that the Fumasep (FAD and FKD) and Selemion (AMV and CMV) membrane combinations obtained the highest power density of approximately 1.2 W/m^2. This power density was achieved for artificial river water and seawater with concentrations of 1 g/L and 30 g/L NaCl, respectively. As the membrane electrical conductivities/resistances were not published, it is difficult to compare the individual performance of these membranes to those in other studies. Commercial IEX membranes Neosepta CM-1 (cation exchange) and Selemion AFS (anion exchange) have been shown to have the lowest electrical area conductivities (reciprocal of the area resistance), measured to be ~6,000 and ~15,000 S/m^2, respectively [33]. An important part of the RED stack, electrode performance has been shown have a minor impact on stack resistance [22]; therefore, further investigation into electrode materials is unlikely to result in significant power density improvements. Electrode segmentation is a novel concept which should certainly be incorporated into future large-scale optimization of RED stacks [34]. For the most part, RED stacks studied in the literature have been small-scale systems with limited membrane surface area and cell pairs. However, Veerman et al. recently developed a 50-cell RED stack in order to demonstrate the performance of a comparatively large system [4]. This system was able to achieve a power density of 0.93 W/m^2, the highest power density achieved in practice from a sea-river water salinity-gradient source.

Table 1.1 Characteristics of commercial and prototype osmotic membranes and their potential power density.

Membrane	A[1]	B[2]	S[3]	W, SW[b,c]	W, Brine[c]	Ref
Lab Cellulose-Acetate-FO	0.41	0.22	52	0.7	2.7	[28]
Lab TFC-FO	5.27	0.91	312	6.1	15.3	[25]
Lab TFC-FO	3.22	1.3	492	3.8	10.1	[27]
Lab TFC-FO (hollow fiber)	6.2	0.56	595	5.5	8.7	[26]
Commercial FO Cellulose	2.2	1.2	625	2.8	7.8	[7, 27]
Lab TFC-FO	7.1	1.1	670	4.7	6.5	[24]
Commercial RO Cellulose-	2	0.6	1000	2.4	5.9	[27]
Commercial TFC-RO[a]	1.6	0.8	2200	1.2	2.1	[27]

[1] = ($\times 10^{-12}$ m Pa^{-1} s^{-1}), [2] = ($\times 10^{-7}$ m s^{-1}), [3] = ($\times 10^{-6}$ m), *[a] = without fabric support, [b] = SW means seawater, [c] = dilute stream concentration of 0.02M , i.e. that of treated wastewater – with units of* W/m^2

Table 1.2 Characteristics of commercial ion-exchange membranes and their potential power density.

Anion Exchange Membranes	**Type**	**α**	**$1/R_{aem}$[1]**	**W**	**Ref**
Neosepta AFN	Homogenous	88.9	1.43	1.23 - 1.30	[21]
Selemion APS	Homogenous	88.4	1.47	1.23 - 1.30	[21]
Fumasep FAD	Homogenous	86	1.12	1.16 - 1.24	[35]
Neosepta AMX	Homogenous	90.7	0.43	1.02 - 1.22	[35]
Ralex AMH-PES	Heterogeneous	89.3	0.13	0.73 - 1.12	[21]
Cation Exchange Membranes	**Type**	**α**	**$1/R_{cem}$[1]**	**W**	**Ref**
Neosepta CM-1	Homogenous	97.2	0.6	1.12 - 1.30	[35]
Fumasep FKD	Homogenous	89.5	0.47	0.99 - 1.19	[21]
Neosepta CMX	Homogenous	99	0.34	1.02 - 1.30	[35]
Ralex CMH-PES	Heterogeneous	94.7	0.09	0.73 - 1.23	[21]

[1] = (10^4 S/m^2)

1.3 Preliminary results

A sensitivity analysis was conducted in order to identify the role of mass transfer and membrane permeability on maximum power density. Furthermore, PRO and RED were compared through maximum power density using current state-of-the-art membranes and membranes with projected properties.

1.3.1 Modeling mass transfer limitations in PRO and RED

We begin by examining the limitations imposed by mass transfer, i.e. external and, for PRO, internal concentration polarization. Recent efforts on improving membrane characteristics for PRO have focused their attention on the minimization of the support membrane structure factor. Assuming that there are no external mass transfer limitations, that is, complete mixing of the streams, **Figure 1.4** shows the variation of the power output with membrane water permeability for different structure factors. Note how, for the representative permeability of current FO membranes (marked with a vertical dotted line) changing the structure factor has a minor impact on the power density.

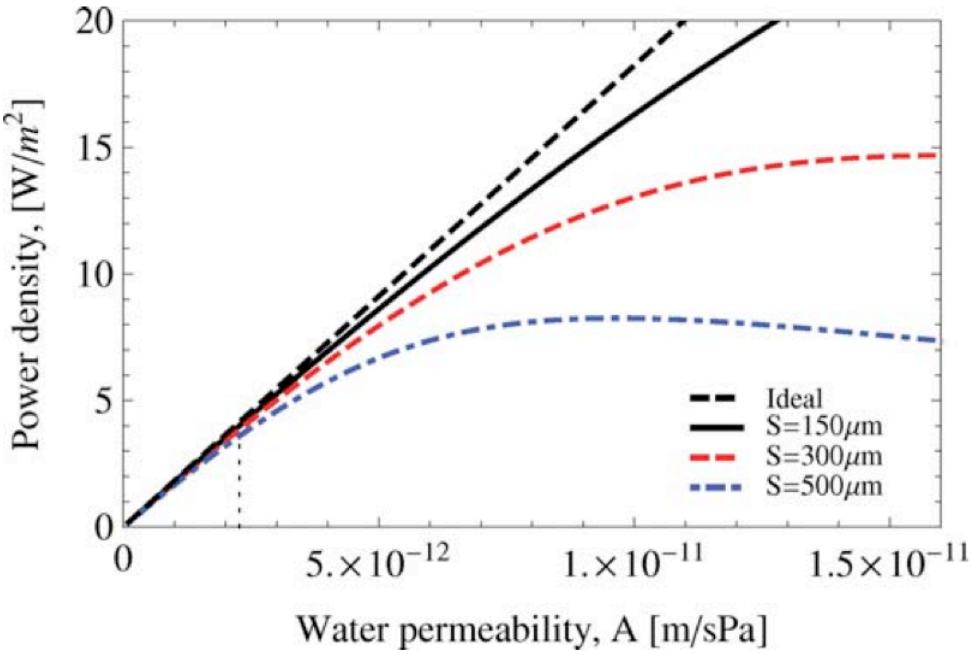

Figure 1.4 Variation of PRO power density with increasing water permeability, for different values of the structure factor, S, under complete mixing conditions (no ECP). Also shown is an ideal power curve, calculated without any mass transfer limitations. The vertical dotted line marks the water permeability of a commercially available FO membrane. In these calculations, the salt permeability is set at B = 10^{-7} m/s, the concentrated solution is seawater (0.55 M) and the dilute solution has a concentration of 5mM.

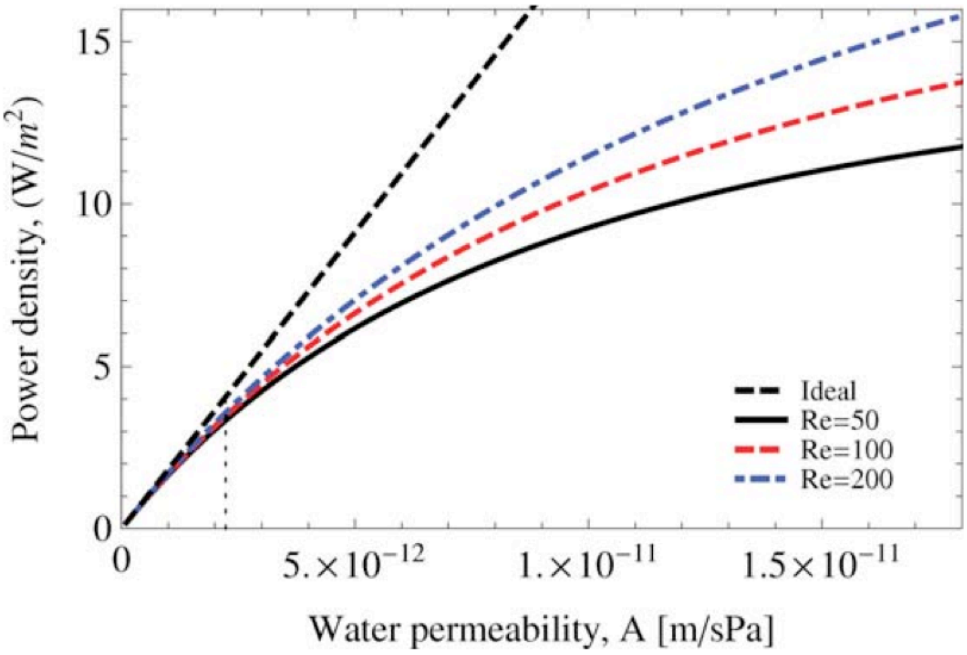

Figure 1.5 Variation of PRO power density with increasing water permeability, for a membrane with S = 50 microns, showing the effect of external mixing. Also shown is an ideal power curve, calculated without any mass transfer limitations. The vertical dotted line marks the water permeability of a commercially available FO membrane. In these calculations, the salt permeability is set at $B = 10^{-7}$ m/s, the concentrated solution is seawater (0.55 M) and the dilute solution has a concentration of 5 mM.

Only upon a significant increase of the water permeability does the advantage of a smaller structure factor come into play, reach a maximum and then decline once again as internal polarization becomes a limiting factor. For the best prototype membrane permeability, a structure factor greater than 500 mm will limit performance. A similar trend is observed when the effect of external polarization is considered (**Figure 1.5**), calculated with a structure factor of 50 mm, the lowest achieved so far; external mass transfer variations are manifested through the Reynolds number which embodies any changes made to the flow velocity or channel hydraulic diameter.

The power production is only weakly limited by external mass transfer; in fact, model calculations predict that for a low structure factor, the membrane permeability can be increased by nearly one order of magnitude before external mass transfer would limit the power density. It must be noted that, as already mentioned, any increase in the operating Reynolds number would also result in parasitic hydraulic losses which are not accounted for in the model used herein; such losses must be considered at the module-scale, as they may overwhelm any power gained by increased mass transfer.

The RED process is much less sensitive to mass transfer and membrane conductivity, since other resistances in the system, particularly the dilute channel resistance, play a dominant role in imposing the process limitation. Typical operating conditions reported in the literature are at a Reynolds number on the order of unity, two orders of magnitude lower than in PRO. Given currently available membrane parameters and stack design, increased mass transfer offers little to gain – operating at a higher Reynolds number of 100 would increase the power density by ~35%. Moreover, if the membrane conductivity were increased by one order of magnitude, the gain in power density would be a meager 11%. This trend is illustrated in **Figure 1.6**, where the power density is plotted against the membrane area conductivity, for different crossflow velocities as well as a 'complete mixing' case. A similar trend is observed when the feed channel height is varied, as shown in **Figure 1.7**. An 'ideal' RED stack would have a highly ion-conductive membrane and well-mixed streams but would still require a finite channel height for pumping the dilute solution. The results illustrate that changing the channel height has the greatest impact on the power density; with currently available membranes, decreasing the channel height three-fold, from 0.6 mm to 0.2 mm, results in a 2.6-fold increase in the power density.

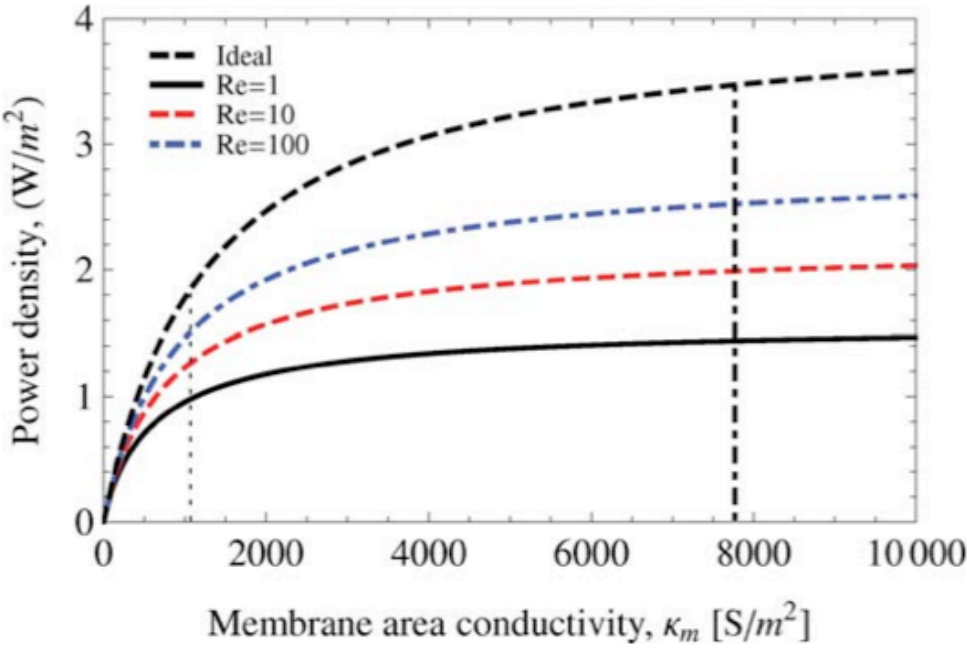

Figure 1.6 Variation of RED power density with average membrane area conductivity illustrating the effect of external mixing. Also shown is an ideal power curve, calculated without any mass transfer limitations. The vertical dotted and dash-dotted lines mark the conductivity of commercial heterogeneous and homogeneous membranes, respectively. In these calculations, the average permselectivity is set at $\alpha = 0.95$, the channel height is $h = 200$ microns, the concentrated solution is seawater (0.55 M) and the dilute solution has a concentration of 5 mM.

1.3.2 Membrane selectivity in PRO and RED

Salt leakage has been viewed as a significant loss mechanism in PRO, primarily due to the fact that with low salinity feeds the main reason for ICP is salt transport across the membrane from the draw to the feed. This is intimately tied with the structure factor, which is the main parameter controlling the severity of ICP. However, when non-ideal feeds are used the main cause for ICP is salt accumulation and not salt-leakage. Acknowledging this point warrants the consideration of a different paradigm for future development of PRO membranes - the goal is to increase water transport, even if such an increase incurs a concurrent decrease in salt rejection; in other words, as long as the net outcome is an increased power output, who cares about salt leakage?

Efficiency set aside, the purpose of PRO is power generation, not separation. This point is illustrated in **Figure 1.8**, where the power density is plotted against the membrane permeability, for varying salt permeabilities and structure factors. As may be seen, there is little to be gained when the membrane selectivity is higher than that currently available; in fact, if the structure factor is low (e.g. 150 mm) power output will increase as the membrane permeability is improved, even at the expense of losing selectivity five-fold. This is a major point to consider in

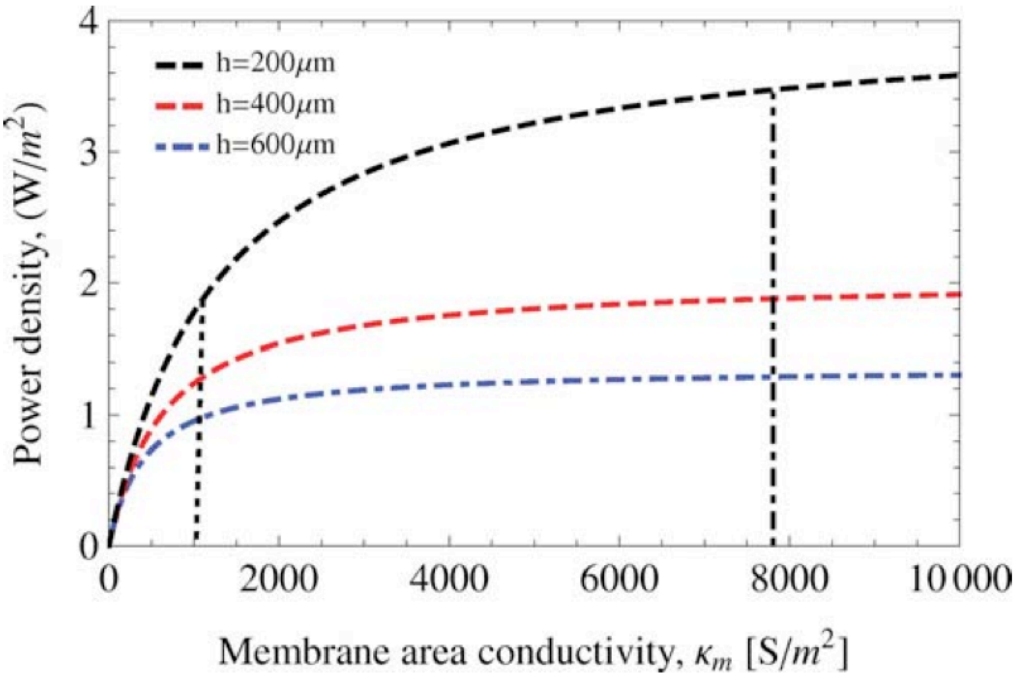

Figure 1.7 Variation of RED power density with average membrane area conductivity, illustrating the effect of the feed channel height, h, under complete mixing. The vertical dotted and dash-dotted lines mark the conductivity of commercial heterogeneous and homogeneous membranes, respectively. In these calculations, the average permselectivity is set at $\alpha = 0.95$, the concentrated solution is seawater (0.55 M) and the dilute solution has a concentration of 5 mM.

future development of PRO membranes, since experience shows that membrane permeability usually comes at some penalty in selectivity [36]. Process efficiency will, of course, be reduced

since salt leakage represents a loss mechanism; however, it would appear that such losses may be an inevitable consequence of increasing the water permeability. Nevertheless, the power gain would certainly offset the lowered efficiency.

For RED, the permselectivity plays a comparatively more important role since it does not induce losses but in effect controls the transport of charge – the power source itself. Nevertheless, results suggest that this effect is not very significant – increasing the average permselectivity from the currently available value of 0.95 to unity will increase the power density by 9%. If improved membrane conductivity would result in reduced permselectivity (the trade-off between transport resistance and selectivity), these two effects would all but cancel out any improvement to the achieved power output; for example, upon reducing the permselectivity to 0.9, an order of magnitude conductivity increase would result in a 3–15% power gain for a corresponding Reynolds number ranging between ~1–100.

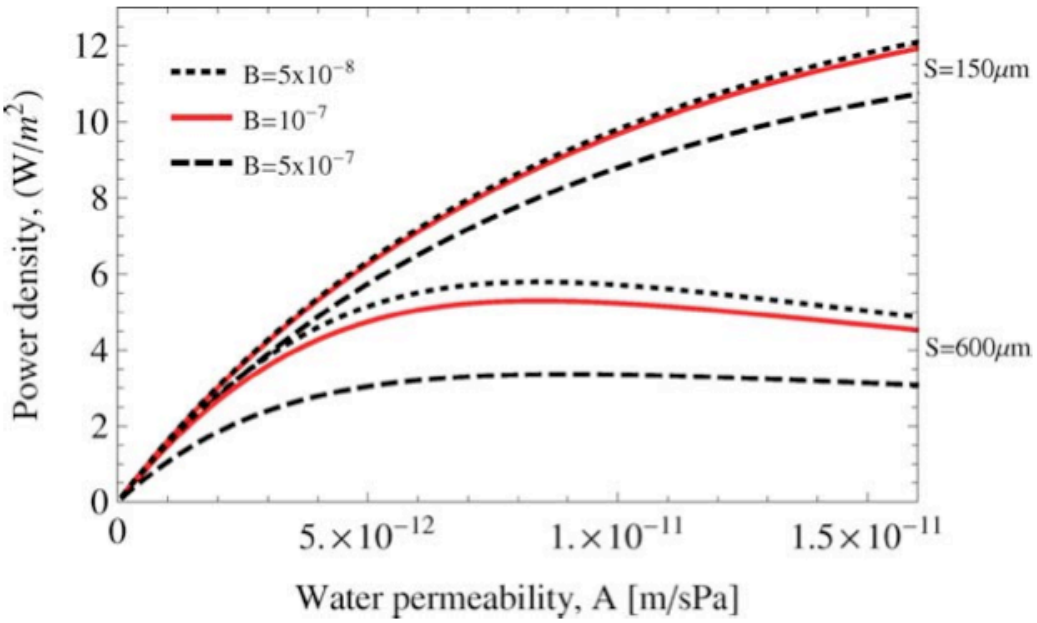

Figure 1.8 Variation of PRO power density with increasing water perme- ability, for different salt permeabilities and structure factors. In these calculations, the Reynolds number is set at Re 1⁄4 100, the concentrated solution is seawater (0.55 M) and the dilute solution has a concentration of 5 mM.

1.3.3 Comparing PRO and RED

Finally, we turn to compare the performance of the two membrane-based processes considered. This is done based on the simplified models presented and is made for two scenarios; the first considers process and membrane parameters which are based on the current state-of-the-art as reported in the recent literature (**Figure 1.9**); the other considers potential improvements (**Figure 1.10**). The parameters used for both scenarios are listed in **Table 1.3**. The main improvements to PRO are in the increased water permeability, with an assumed penalty to the salt rejection, and the decreased structure factor. For RED, an increased conductivity is assumed without a reduction in permselectivity (e.g. a thinner membrane), and the channel height is further reduced.

Note that the RED power density contours exhibit an inflection point at low dilute stream salinity. This is due to the increased resistance of the solution as it approaches the conductivity of pure water, at which point the concentration gradient required to maintain a constant power density increases sharply. The point of inflection itself represents the conditions which conspire to produce the minimum resistance in the dilute channel, through the combined effects of the channel height and solution conductivity, as given in **Eq.** 1.7**.** This is an important point to consider, as it may be beneficial for the RED process to operate with slightly brackish water as the dilute stream, resulting in a lowered resistance at reasonable channel heights.

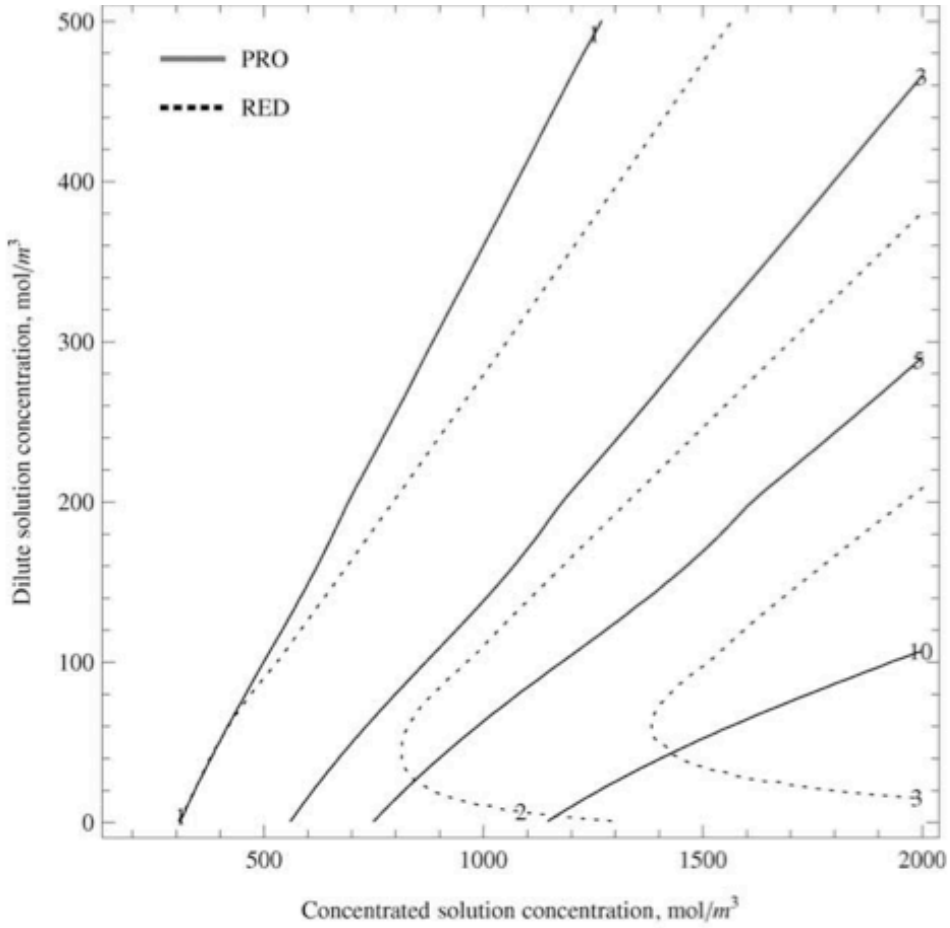

Figure 1.9 Contours of constant power density characteristic of PRO and RED, as a function of the salinity gradient, calculated for state-of-the-art process parameters.

The presented calculations suggest that, based on power density, PRO has a better potential for use as a means for harvesting salinity-gradient energy. This is already true for commercially available membranes, and with potential possible improvements to the membranes the gap becomes even greater, in favor of PRO. This is true no matter what salinity gradient is used as the energy source, in contrast with the conclusions drawn by Post et al [23]. In their paper from 2007, they provided an insightful comparison of PRO and RED with the conclusion that RED produces a higher power density for low salinity gradients, such as the sea-river water pair. The membrane parameters used in the present study are generally better than those used by

Post et al. [23] for both RED and PRO. Specifically, the commercialization of FO membranes has already made PRO the more promising option, with a much higher potential for future improvement. For example, the current state-of-the-art, optimum power density achievable for PRO for the sea-river water pair is 2.3 W/m^2 compared with 1.3 W/m^2 for RED. With projected improvements, the gap increases to 7.7 W/m^2 vs. 3.4 W/ m^2 for the sea-river water pair, while if RO brine is used the corresponding values become 21.2 W/m^2 and 5.2 W/m^2.

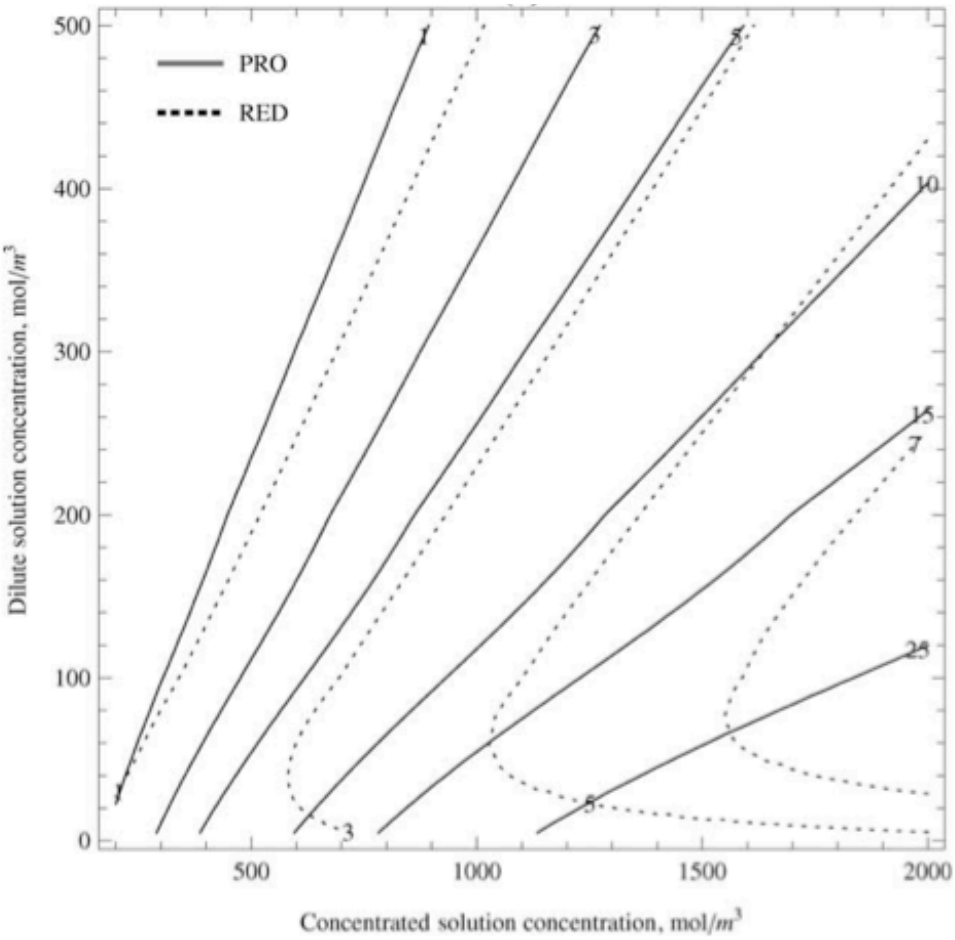

Figure 1.10 Contours of constant power density characteristic of PRO and RED, as a function of the salinity gradient, calculated for projected process parameters.

Table 1.3. Process characteristics used for calculation of power density

PRO	A[1]	B[2]	S[3]
State of the art	2.2	1.2	625
Projected	10	5	150
RED	$1/R_{mem}$[4]	**α**	**Channel height**
State of the art	0.8	0.95	200
Projected	3.5	0.95	100

[1] = ($\times 10^{-12}$ m Pa^{-1} s^{-1}), [2] = ($\times 10^{-7}$ m s^{-1}), [3] = ($\times 10^{-6}$ m), [4] = (10^4 S/m^2)

1.4 Hypothesis and scope of work

1.4.1 Hypothesis

The preliminary research discussed in **Section 1.3** suggests that computational models can inform the design and engineering of SGP processes. In particular, the maximum power density models demonstrate that RED is fundamentally limited by the dilute channel resistance, and that improvements in membrane conductivity are likely to have little impact on power density. For PRO, however, there is significant opportunity for increasing power performance through membrane enhancements. Water permeability appears to be far more limiting that structure factor for many prototype PRO membranes discussed in the literature. Furthermore, in improving PRO water permeability, some degree of salt rejection can be tolerated if structure is simultaneously decreased.

As noted earlier, previous modeling work on SGP technologies has focused on the maximum power density produced through PRO or RED. However, maximum power density

alone is an insufficient metric for designing a large-scale, realistic SGP system. In an idealized system, maximum power density would occur at the inlet to the flow channel where there exists the largest difference in concentration between the dilute and concentrated solutions. On the other hand, energy efficiency theoretically maximizes at infinite module length (where the driving force approaches zero). In a real system, where viscous dissipation and other inefficiencies are inevitable, power density and efficiency will likely deviate from these idealized behaviors. Therefore, in order to evaluate the scale-up of SGP technologies, it is critical to understand the variation in power density and energy efficiency (and thus, total power output) with system length. A full-scale process model, which accounts for changes in velocity, pressure, and concentration along the length of the flow channels can provide a direct, quantitative indication of these important process metrics.

It is hypothesized that a full-scale process model, incorporating hydraulic losses and machine inefficiencies, will demonstrate that power densities from PRO and RED are far lower than existing, maximum power density models predict. In addition, the full-scale process model will capture total power output and thermodynamic efficiency with changing system size, allowing for the first time a rigorous comparison with other alternative energy technologies. Finally, the model will also identify ideal operating conditions that may deviate from those specified by existing, maximum power density models.

1.4.2 Scope of work

1. Develop a thermodynamic model for each process in order to determine the fundamental limiting efficiency.

2. Develop new full-scale, crossflow process model for each process, with the ability to calculate power density, thermodynamic efficiency, and total power output with changing system length (or area). Sensitivity analysis will be conducted on model parameters, and optimization will highlight those operating conditions that maximize performance.
3. Using the full-scale process model, identify novel process configurations that maximize efficiency and/or power density.
4. Incorporate cost data into the full-scale process model in order to determine capital and operating expenditure of a SGP plant.

1.4.3 Overview of dissertation

The present dissertation includes 6 Chapters and 2 Appendices. **Chapter 1** serves as an introduction to the work, and includes general background and preliminary work. Research hypotheses and objectives are also discussed in this chapter.

Chapter 2 presents simple thermodynamic models for PRO and RED. Using these models, SGP processes are integrated with an existing reverse osmosis model in order to evaluate the reduction in energy demand of desalination.

Chapter 3 presents full-scale process models for both PRO and RED in order to probe scale-up characteristics with changing system size and operating conditions. Ideal process parameters are highlighted.

In Chapter 4, the developed PRO process model is applied to a novel, "staged" PRO configuration. This configuration is shown to dramatically improve the water flux, and therefore process efficiency, in PRO.

Chapter 5 incorporates cost correlations into the PRO process model in order to evaluate the cost of energy production. Membrane parameters and operating conditions are shown to have a significant impact on energy cost.

Finally, major conclusions and suggestions for future research are included in **Chapter 6**.

1.5 References

[1] J.A. Turner, A Realizable Renewable Energy Future, Science, 285 (1999) 687-689.

[2] J.D. Isaacs, R.J. Seymour, The ocean as a power resource, international journal of environmental studies, 4 (1973) 201-205.

[3] G. Wick, W. Schmitt, Prospects for renewable energy from sea, Mar. Technol. Soc. J, 11 (1977) 16-21.

[4] J. Veerman, M. Saakes, S.J. Metz, G.J. Harmsen, Electrical Power from Sea and River Water by Reverse Electrodialysis: A First Step from the Laboratory to a Real Power Plant, Environmental Science & Technology, 44 (2010) 9207-9212.

[5] J.W. Post, H.V.M. Hamelers, C.J.N. Buisman, Energy recovery from controlled mixing salt and fresh water with a reverse electrodialysis system, Environmental Science & Technology, 42 (2008) 5785-5790.

[6] P. Długołęcki, A. Gambier, K. Nijmeijer, M. Wessling, Practical potential of reverse electrodialysis as process for sustainable energy generation, Environmental science & technology, 43 (2009) 6888-6894.

[7] A. Achilli, T.Y. Cath, A.E. Childress, Power generation with pressure retarded osmosis: An experimental and theoretical investigation, Journal of Membrane Science, 343 (2009) 42-52.

[8] N.Y. Yip, M. Elimelech, Performance Limiting Effects in Power Generation from Salinity Gradients by Pressure Retarded Osmosis, Environmental Science & Technology, 45 (2011) 10273-10282.

[9] D. Brogioli, R. Zhao, P.M. Biesheuvel, A prototype cell for extracting energy from a water salinity difference by means of double layer expansion in nanoporous carbon electrodes, Energy & Environmental Science, 4 (2011) 772-777.

[10] D. Brogioli, Extracting Renewable Energy from a Salinity Difference Using a Capacitor, Physical Review Letters, 103 (2009) 058501.

[11] D.K. Kim, C.H. Duan, Y.F. Chen, A. Majumdar, Power generation from concentration gradient by reverse electrodialysis in ion-selective nanochannels, Microfluidics and Nanofluidics, 9 (2010) 1215-1224.

[12] X. Cao, X. Huang, P. Liang, K. Xiao, Y. Zhou, X. Zhang, B.E. Logan, A New Method for Water Desalination Using Microbial Desalination Cells, Environmental Science & Technology, 43 (2009) 7148-7152.

[13] M. Mehanna, T. Saito, J. Yan, M. Hickner, X. Cao, X. Huang, B.E. Logan, Using microbial desalination cells to reduce water salinity prior to reverse osmosis, Energy & Environmental Science, 3 (2010) 1114-1120.

[14] S. Loeb, F. Van Hessen, J. Levi, M. Ventura, The Osmotic power plant, in: 11th Intersociety Energy Conversion Engineering Conference, 1976, pp. 51-57.

[15] R.S. Norman, Water salination: a source of energy, Science, 186 (1974) 350-352.

[16] J.N. Weinstein, F.B. Leitz, Electric power from differences in salinity: the dialytic battery, Science, 191 (1976) 557-559.

[17] K. Lee, R. Baker, H. Lonsdale, Membranes for power generation by pressure-retarded osmosis, Journal of Membrane Science, 8 (1981) 141-171.

[18] G.D. Mehta, S. Loeb, Internal polarization in the porous substructure of a semipermeable membrane under pressure-retarded osmosis, Journal of Membrane Science, 4 (1979) 261-265.

[19] G. Guillen, E.M.V. Hoek, Modeling the impacts of feed spacer geometry on reverse osmosis and nanofiltration processes, Chemical Engineering Journal, 149 (2009) 221-231.

[20] J. Veerman, R. De Jong, M. Saakes, S. Metz, G. Harmsen, Reverse electrodialysis: Comparison of six commercial membrane pairs on the thermodynamic efficiency and power density, Journal of Membrane Science, 343 (2009) 7-15.

[21] P. Długołęcki, J. Dąbrowska, K. Nijmeijer, M. Wessling, Ion conductive spacers for increased power generation in reverse electrodialysis, Journal of Membrane Science, 347 (2010) 101-107.

[22] J. Veerman, M. Saakes, S. Metz, G. Harmsen, Reverse electrodialysis: evaluation of suitable electrode systems, Journal of Applied Electrochemistry, 40 (2010) 1461-1474.

[23] J.W. Post, J. Veerman, H.V. Hamelers, G.J. Euverink, S.J. Metz, K. Nymeijer, C.J. Buisman, Salinity-gradient power: Evaluation of pressure-retarded osmosis and reverse electrodialysis, Journal of Membrane Science, 288 (2007) 218-230.

[24] K. Gerstandt, K.-V. Peinemann, S.E. Skilhagen, T. Thorsen, T. Holt, Membrane processes in energy supply for an osmotic power plant, Desalination, 224 (2008) 64-70.

[25] A. Tiraferri, N.Y. Yip, W.A. Phillip, J.D. Schiffman, M. Elimelech, Relating performance of thin-film composite forward osmosis membranes to support layer formation and structure, Journal of Membrane Science, 367 (2011) 340-352.

[26] R. Wang, L. Shi, C.Y. Tang, S. Chou, C. Qiu, A.G. Fane, Characterization of novel forward osmosis hollow fiber membranes, Journal of Membrane Science, 355 (2010) 158-167.

[27] N.Y. Yip, A. Tiraferri, W.A. Phillip, J.D. Schiffman, M. Elimelech, High performance thin-film composite forward osmosis membrane, Environmental Science & Technology, 44 (2010) 3812-3818.

[28] S. Zhang, K.Y. Wang, T.-S. Chung, H. Chen, Y. Jean, G. Amy, Well-constructed cellulose acetate membranes for forward osmosis: minimized internal concentration polarization with an ultra-thin selective layer, Journal of Membrane Science, 360 (2010) 522-535.

[29] G.T. Gray, J.R. McCutcheon, M. Elimelech, Internal concentration polarization in forward osmosis: role of membrane orientation, Desalination, 197 (2006) 1-8.

[30] J.R. McCutcheon, M. Elimelech, Influence of concentrative and dilutive internal concentration polarization on flux behavior in forward osmosis, Journal of Membrane Science, 284 (2006) 237-247.

[31] Y. Xu, X. Peng, C.Y. Tang, Q.S. Fu, S. Nie, Effect of draw solution concentration and operating conditions on forward osmosis and pressure retarded osmosis performance in a spiral wound module, Journal of Membrane Science, 348 (2010) 298-309.

[32] S.E. Skilhagen, J.E. Dugstad, R.J. Aaberg, Osmotic power—power production based on the osmotic pressure difference between waters with varying salt gradients, Desalination, 220 (2008) 476-482.

[33] T. Xu, Ion exchange membranes: state of their development and perspective, Journal of Membrane Science, 263 (2005) 1-29.

[34] J. Veerman, M. Saakes, S. Metz, G. Harmsen, Reverse electrodialysis: A validated process model for design and optimization, Chemical Engineering Journal, 166 (2011) 256-268.

[35] P. Długołęcki, K. Nymeijer, S. Metz, M. Wessling, Current status of ion exchange membranes for power generation from salinity gradients, Journal of Membrane Science, 319 (2008) 214-222.

[36] G.M. Geise, H.B. Park, A.C. Sagle, B.D. Freeman, J.E. McGrath, Water permeability and water/salt selectivity tradeoff in polymers for desalination, Journal of Membrane Science, 369 (2011) 130-138.

2 THERMODYNAMIC ANALYSIS OF SALINITY GRADIENT POWER AND OSMOTIC ENERGY RECOVERY

2.1 Introduction

Reverse osmosis (RO) technology now dominates the global market for seawater desalination, primarily due to its significantly lower energy consumption compared with thermal technologies. The advance of RO technology is primarily due to improvements in membrane materials, modules, process components and process designs, which have resulted in significant reductions of the specific energy consumption (SEC) and cost of water produced. Notably, SEC has been nearly halved due to high-efficiency hydraulic energy recovery (HER) devices, which transfer hydraulic energy from the (still) high-pressure brine stream, prior to its discharge, to the low-pressure incoming feed stream. Including pre-treatment, state of the art installations now operate with a SEC on the order of 2.5 kWh/m^3 [1]. From elementary thermodynamics it may be calculated that the minimum energy required to extract 1m^3 of freshwater at 50% recovery (i.e., from 2 m^3 of seawater) is ~1.1 kWh, which implies that a substantial gap still exists between theory and practice. Certainly, some gap must always exist due to intrinsic irreversibilities and losses; however, the energy demand of RO still accounts for 40-50% of the cost of water in seawater desalination [2], clearly suggesting that a break-through reduction in the energy demand must be sought in order to transform desalination into a more cost-effective, sustainable source of fresh water.

One such possibility is the partial recovery of the chemical potential of the concentrated brine – the very same energy spent separating water out of the feed solution – employing an osmotic energy recovery process. Osmotic energy recovery (OER) involves harvesting the energy released during the controlled mixing of two solutions with different salt concentrations (*i.e.*, a salinity gradient). Different techniques exist for the recovery of energy from the mixing of varied salinity flows. These technologies include reverse electrodialysis (RED) [3-5], pressure

retarded osmosis (PRO) [6, 7], capacitive mixing [8, 9], and mixing in ion selective nano-channels [10]. Recently, a microbially-assisted RED process has been developed that simultaneously treats wastewater, produces desalinated water, and generates electricity [11, 12].

A comparison of the power potential for the two most prominent, membrane-based salinity gradient technologies, PRO and RED, was recently published, in which the various technological challenges were outlined, and the most promising avenues for improvement were identified [13]. Briefly, PRO and RED are theoretically reversed versions of the RO and ED desalination techniques, respectively. In PRO, water molecules diffuse across a semi-permeable membrane from a high chemical potential (dilute) feed into a pressurized, low chemical potential (concentrated) feed. The volume-augmented, concentrated feed is then passed through a hydroturbine, generating electricity. In RED, ion selective membranes separate alternating concentrated and dilute feed compartments. The concentration difference between the feeds encourages the diffusion of anions against the electric field, creating an ionic flux that is converted into an electron flux at the electrodes. Despite the fact that power densities from these SGP processes still remain relatively low, improvements in power densities have been forecast in the literature [13, 14].

The use of seawater RO brine in an RED process has been previously suggested in the patent literature[15]; however, energy recovery from the RO feed was not considered. Recently, the use of forward osmosis, a membrane based process proposed for desalination application, has been suggested in the literature in a coupled RO process arrangement [16, 17]. This “osmotic dilution” reduces the energy demand of RO and, although the use of a SGP technology is briefly discussed, the authors do not present a quantitative analysis of the energy saving potential of osmotic energy recovery. During the revision process for this publication, it has come to our

attention that an insightful study of an RO-RED coupled process has been recently published [18]. Although the authors do not comprehensively study the thermodynamics of mixing (or the use of PRO as a mixing technology), their conclusions for the RO-RED coupled process show that a coupled RO-RED process could reduce the net SEC of seawater RO to below zero kilowatt-hours per cubic meter of RO permeate.

In this study, we assess the possibility of osmotic energy recovery from both the RO feed stream *and* the RO brine. A straightforward thermodynamic analysis is used to evaluate the potential of PRO and RED processes coupled to a typical seawater RO plant. Here we provide insight into the way various process parameters affect the optimal SEC for a hybrid RO-HER-OER plant configuration. It is our intent to theoretically probe the process potential through the thermodynamically available work produced by each OER technology. Hence, system-specific losses, e.g., hydraulic losses (pumps, piping, modules etc.), membrane losses and other sources of inefficiency are ignored. This is based on our contention that, prior to resolving such details, it is desirable to first establish the motivation for process implementation.

2.2 Theory

2.2.1 Process description

Several potential configurations may be envisioned for integrating osmotic energy recovery with RO desalination, perhaps the most obvious one being re-mixing the concentrated brine with seawater. However, the complete mixing of equal volumes of seawater and RO-brine (at 50% recovery) would theoretically yield ~0.12 kWh/m^3. A significantly greater impact is envisioned when a low-salinity water source is present such as fresh surface water, tertiary

wastewater or RO concentrate from a wastewater reuse plant or other mildly brackish natural or industrial waters. The potential for mixing with treated wastewaters of different origins will vary on a site-by-site basis; however, coordinated site planning could allow for co-location of wastewater treatment or reuse plants with seawater RO facilities. In such a case, it would generally be possible to employ OER technology on the RO feed side and the brine outflow, mixing the low-salinity wastewater either with incoming seawater or the brine, prior to discharge. The greatest potential energy is obviously contained in the brine-wastewater pair; however, mixing the seawater-wastewater pair prior to RO has merit beyond the energy of mixing, as it also significantly reduces the salinity of the RO feed, translating into further reduction of energy consumption. Hence, the RO-OER process considered in the forgoing analysis employs two stages of osmotic energy recovery coupled with a HER-equipped seawater RO process (**Figure 2.1** and **Table 2.1**). The coupled process includes both pre-RO, OER mixing (OER_1) and post-RO, OER mixing (OER_2).

Table 2.1 Flow volumes and concentrations at each point in the coupled process (see **Figure 2.1** for accompanying graphical representation).

Designation	Flow Type	Volume	Concentration
1	Seawater	$V_{c,i,OER1}$	$c_{c,i,OER1}$
2	Treated wastewater	$V_{d,i,OER1} = V_{c,i,OER1}/\phi$	$c_{d,i,OER1}$
3	Diluted seawater	$V_{c,f,OER1}$	$c_{c,f,OER1}$
4*	Diluted seawater	$V_{c,f,OER1} - V_{c,i,OER1}$	$c_{c,f,OER1}$
5	Diluted seawater	$V_f = V_{c,i,OER1}$	$c_f = c_{c,f,OER1}$
6	Concentrated treated wastewater	$V_{d,f,OER1}$	$c_{d,f,OER1}$
7	RO permeate	$V_p = V_{c,i,OER1}Y$	c_p
8	RO brine	$V_{c,i,OER2} = V_b = V_{c,i,OER1}(1-Y)$	$c_b = c_{c,i,OER2}$
9	Treated wastewater	$V_{d,i,OER2} = V_{c,i,OER2}/\phi$	$c_{d,i,OER2} = c_{d,i,OER1}$
10	Diluted RO brine	$V_{c,f,OER2}$	$c_{c,f,OER2}$
11	Concentrated treated wastewater	$V_{d,f,OER2}$	$c_{d,f,OER2}$

* = PRO Only

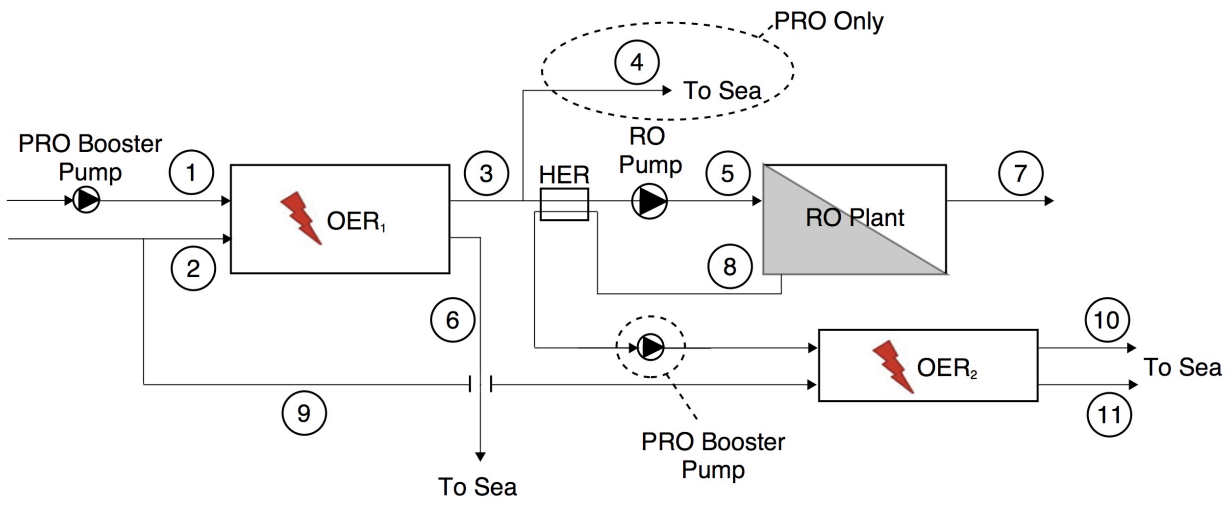

Figure 2.1 Schematic representation of the coupled process. Numerical designations correlate to volumes and concentrations in **Table 2.1**.

For the sake of comparison, the straightforward dilution of the seawater inflow through direct mixing with low-salinity sources was also considered as a means by which the energy demand of RO may be lowered [16]. The direct dilution method, while probably cheaper than OER, will provide fewer barriers to the transport of emerging contaminants into the RO permeate, an important consideration for drinking water production from seawater; however, not all seawater RO plants are designed to produce potable water. Regardless, any OER device should have a good capacity to keep such cross-contamination to a minimum to ensure the seawater RO product remains of appropriate quality. In the case of membrane-based OER, rejection of both pesticides and pharmaceutical compounds was found to exceed 95% in polyamide-based, thin film composite RO membranes, materials which seem likely to find use in PRO[19]. Similarly, ion exchange membranes, used in RED, can be finely tuned for the separation or concentration of a variety of pharmaceuticals and organic compounds [20]. It is

unclear as to what degree of cross-contamination would be expected when employing other, emerging, salinity-gradient energy devices.

As already mentioned above, we are interested in the maximum energy recoverable through each of these mixing methods. Therefore, we do no consider membrane or module related inefficiencies, hydraulic losses in pumps/turbine/pipeworks or the possible energy demands of pre-treatment. For consistency, the volume passed to the RO process is kept constant regardless of the OER technology chosen (PRO inherently involves significant volumetric exchanges while in RED this is negligible). This results in the discharging of excess flow from the PRO process before transfer to the RO system. In a practically applied coupled process it is likely that the PRO plant would be sized so that the PRO outflow would directly meet the RO feed supply requirement. This would reduce the capital investiture for the PRO plant but would result in less overall energy savings due to reduced flow rate (and thus recovered energy) through the PRO plant.

2.2.2 The free energy of mixing

The energy released during the mixing of two solutions with different molecular compositions was calculated through a method similar to that described by Yip et al. [21], although having been modified using basic mathematics, the equation appears here in slightly different form. Operational and engineering constraints would prevent any OER process from achieving full mixing, and it is therefore useful to evaluate the energy recovery when the outlet feeds are not at thermodynamic equilibrium. The model described herein accounts for scenarios where mixing is less than 100%, whereby the summation of the Gibbs free energy of the two

solutions before and after ideal mixing (i.e., isothermal conditions and activity coefficients set at unity) results in[21]

$$\Delta G = -2RT\left[V_{c,f}c_{c,f}\ln c_{c,f} + V_{d,f}c_{d,f}\ln c_{d,f} - V_{c,i}c_{c,i}\ln c_{c,i} - V_{d,i}c_{d,i}\ln c_{d,i}\right] \tag{2.1}$$

where R is the universal gas constant, T is temperature, V is volume, c is concentration, the subscripts i and f denote before (initial) and after (final) mixing, respectively, and the subscripts c and d refer to the concentrated and dilute solution feeds, respectively.

2.2.3 Mixing by PRO

The reversible work that can be recovered by PRO may be calculated using either the free energy of mixing, **Eq.** 2.1, or through the thermodynamic relationship, $W = \int P\,dV$, where P is pressure and V is volume. The osmotic pressure (i.e. the pressure required to inhibit osmotic diffusion) of the concentrated and dilute feeds, π_c and π_d, respectively, can be calculated through $\pi_i = \left(RT/\overline{V}\right)\ln x_w$, where $\overline{V}$ is the molar volume of water and x_w is the mole fraction of water. The maximum reversible work is calculated by setting the external pressure to the internal pressure within the system, i.e., so that the osmotic pressure difference, $\Delta\pi$, is set equal to P for for each infinitesimally small change in volume according to

$$W_{rev}^{PRO} = \int_0^{\Delta V} \Delta\pi\, dV \tag{2.2}$$

where ΔV is the total volume of water transferred between the two solutions. The expression resulting from the integration of **Eq.** 2.2, used in subsequent calculations, equates to

$$W_{rev}^{PRO} = 2RT\left[c_{c,i}V_{c,i}\ln\left(V_{c,i}+\Delta V\right) + c_{d,i}V_{d,i}\ln\left(V_{d,i}+\Delta V\right)\right]. \tag{2.3}$$

In PRO, extraction of the energy is facilitated by a hydroturbine, which converts the kinetic energy of the flowing water to electricity. During the mixing process, the transport of water across the membrane terminates when thermodynamic equilibrium is reached, i.e., at the point of equal chemical potentials on either side of the membrane. One such equilibrium naturally exists when the osmotic pressure difference is equal to zero, i.e. $\Delta\pi = 0$. However, in the currently accepted configuration used for the operation of PRO the incoming high-concentration feed is pressurized prior to the membrane-mediated mixing process. The reasoning behind this configuration is based on efficiency considerations (pump and turbine). However, the pressurization alters the equilibrium point, which now occurs when $\Delta\pi = \Delta P$, the applied pressure, and therefore limits the extractable energy. It is therefore impossible that a real PRO process would be able to extract all of the reversible work. Therefore, the *available* work extractable from this configuration of a PRO process is the volume `expansion` work performed against the constant applied pressure ,

$$W_{av}^{PRO} = \Delta P \Delta V \tag{2.4}$$

This available work will necessarily be considerably lower in magnitude than the reversible work. Realistically, the actual recoverable work is likely to be even lower than this available work due to the hydraulic resistance of the semipermeable membrane, frictional losses through pipework, and hydroturbine and pump inefficiencies. In the present study, however, we ignore the internal system losses and use W_{av}^{PRO} and W_{rev}^{PRO} as measures of the intrinsic potential for energy savings from a coupled process. Feed volumes and concentrations before and after mixing, for PRO, are listed in **Table 2.2**.

2.2.4 Mixing by RED

The maximum work in a RED process can similarly be calculated either through the free energy of mixing equation (**Eq.** 2.1) or the cell potential $\Delta G = -nF\Delta E$, where n is the number of ions transferred, F the Faraday constant, and ΔE the zero current cell potential (or electromotive force). The electromotive force can be calculated from the difference of the individual half-cell reaction potentials, E_c and E_d, of the concentrated and dilute solutions, respectively. The half-cell reaction potentials can be calculated through $E_i = (RT/z)\ln c_i$, where c_i is the concentration of ions in the given feed and z is the valence of the ions. The maximum reversible work for a given extent of mixing may be calculated as

$$\begin{aligned} W_{rev}^{RED} &= -nF\Delta E = -\frac{2RT}{z}\int_0^{\Delta n}\ln\frac{c_c}{c_d}dn = -\frac{2RT}{z}\int_0^{\Delta n}\ln\frac{\left(\frac{n_{c,i}-n}{V_{c,i}}\right)}{\left(\frac{n_{d,i}+n}{V_{d,i}}\right)}dn \\ &= -\frac{2RT}{z}\left[\Delta n\ln\frac{V_{d,i}\left(n_{c,i}-\Delta n\right)}{V_{c,i}\left(n_{d,i}+\Delta n\right)} - n_{c,i}\ln\left(1-\frac{\Delta n}{n_{c,i}}\right) - n_{d,i}\ln\left(1+\frac{\Delta n}{n_{d,i}}\right)\right] \end{aligned} \tag{2.5}$$

where Δn is the total number of salt ions transferred between the two solutions, and the factor of 2 denotes the transport of both sodium and chloride ions.

It is important to note that in RED energy is extracted through an external circuit, which, while completely analogous to a hydraulic network in the dynamic sense, does not have the same thermodynamic effect – an ideal resistor passing a diffusion-induced current does not alter the equilibrium properties of the system. One may draw a constant current out of an RED cell, to the point where concentrations equilibrate. The applied load resistance will reduce the rate of charge transport, but this current will only cease when the concentrations have equilibrated [18, 22]. Thus, unlike PRO, there is no configurational constraint analogous to a constant applied pressure

that inherently limits the extent of mixing. Inevitable losses such as the electrical resistance of the membranes and the feed compartments will ultimately limit the amount of recoverable work. However, since there is potential to improve these process inefficiencies through future design improvements, for the purposes of the present study (as with PRO) we ignore these internal system losses, and here we apply only W_{rev}^{PRO} in order to calculate the potential energy savings from RED. Feed volumes and concentrations before and after mixing, for RED, are listed in **Table 2.2**.

2.2.5 RO process equations

The RO process recovery can be determined from the RO feed and brine concentrations in addition to the concentrated feed concentrations from OER_1 and OER_2 as

$$Y = \frac{V_p}{V_f} = 1 - \frac{c_f}{c_b} = 1 - \frac{c_{c,f,OER1}}{c_{c,i,OER2}} \tag{2.6}$$

where V_p is RO permeate volume, V_f is RO feed volume, c_f is RO feed concentration and c_b is RO brine concentration. In the coupled scenario, the RO feed concentration is the OER_1 concentrated feed effluent ($c_{c,f,OER1}$, now diluted from the OER process) and the RO brine concentration is the OER_2 concentrated feed influent ($c_{c,i,OER2}$). The specific energy consumption of the RO process can be represented as[23]

$$SEC_{RO} = \Delta P_{RO} = \frac{\pi_{RO}}{1 - Y} \tag{2.7}$$

where ΔP_{RO} is the RO pump pressure and $\Delta \pi_{RO}$ is the inlet osmotic pressure difference between the RO feed and permeate. The above, which applies when a HER device conversion efficiency of unity has been assumed, equates to the RO process thermodynamic restriction. The

thermodynamic restriction corresponds to the necessary RO pump applied pressure to ensure permeate flux across the entire length of the RO module. That is, increase in the feed concentration as water diffuses across the membrane results in greater osmotic pressure difference between the feed and permeate, requiring that the initial applied pressure be sufficient in order to ensure diffusion at the RO module outlet.

The net SEC of the coupled process is obtained by subtracting the energy generated in the pre- and post-RO OER stages from the SEC of the HER-assisted RO process, viz.

$$SEC_{net} = SEC_{RO} - \frac{W_{OER1}}{V_p} - \frac{W_{OER2}}{V_p} \tag{2.8}$$

where the subscripts 1,2, refer to the first and second stage OER, respectively. Calculations for the coupled process have been carried out considering two possible RO configurations: 1) constant pressure applied at 770 psi (53 bar, corresponding with the thermodynamic restriction [23] for a 550 mol/m^3 feed at 50% recovery) and RO brine target concentration of 1100 mol/m^3, which effectively varies the RO process recovery depending on the degree of mixing in OER_1, and 2) constant recovery (Y = 0.5) with variable RO pump applied pressure. Most modern RO facilities operate at Y = 0.5 and we have therefore sought to align our modeling results with actual practice. Note that other non-ideal process losses (hydraulic, mass transfer, dilute channel resistance, etc.) are not included in this analysis. The dilution ratio, ϕ (i.e. the ratio of the OER concentrated feed volume to the dilute feed volume), is taken as unity in the current study, and complete mixing (to thermodynamic equilibrium) is always assumed for the OER_2 process.

Table 2.2 Feed volumes and concentrations before and after mixing for an OER process, where the subscript *c* indicates the concentrated (seawater) feed, the subscript *d* indicates the low salinity (treated wastewater) feed, and the subscript *i* indicates pre-mixing and subscript *f* indicates post-mixing. The number of moles and the volume of water transferred between the feeds are indicated by Δn and ΔV, respectively.

Process	$V_{c,f}$	$V_{d,f}$	$c_{c,f}$	$c_{d,f}$
PRO	$V_{c,i} + \Delta V$	$V_{d,i} - \Delta V$	$n_{c,i} / V_{c,f}$	$n_{d,i} / V_{d,f}$
RED	$V_{c,i}$	$V_{d,i}$	$(n_{c,i} - \Delta n) / V_{c,f}$	$(n_{d,i} + \Delta n) / V_{d,f}$

2.3 Results and Discussion

2.3.1 Available work

We begin by examining the work that can be extracted by the PRO and RED processes alone. **Figure 2.2** shows the maximum reversible work (W_{rev}) from each process plotted against the changing dilute feed (e.g., fresh water or tertiary wastewater) and concentrated feed (e.g., seawater RO feed or brine) concentrations. All mixing begins from the same starting feed concentrations and approaches equilibrium, except where practical constraints may limit the extent of mixing achieved. Although both processes approach the same equilibrium, the concentration profiles follow different paths, a consequence of the different relative amounts of water and salt molecules transferred in the RED and PRO processes, as they approach reversible equilibrium. In practice this means that if the dilute or concentrated feed is to be used in another process after mixing, there may be a preferred recovery technology based on the concentration of the feed at a given extent of mixing.

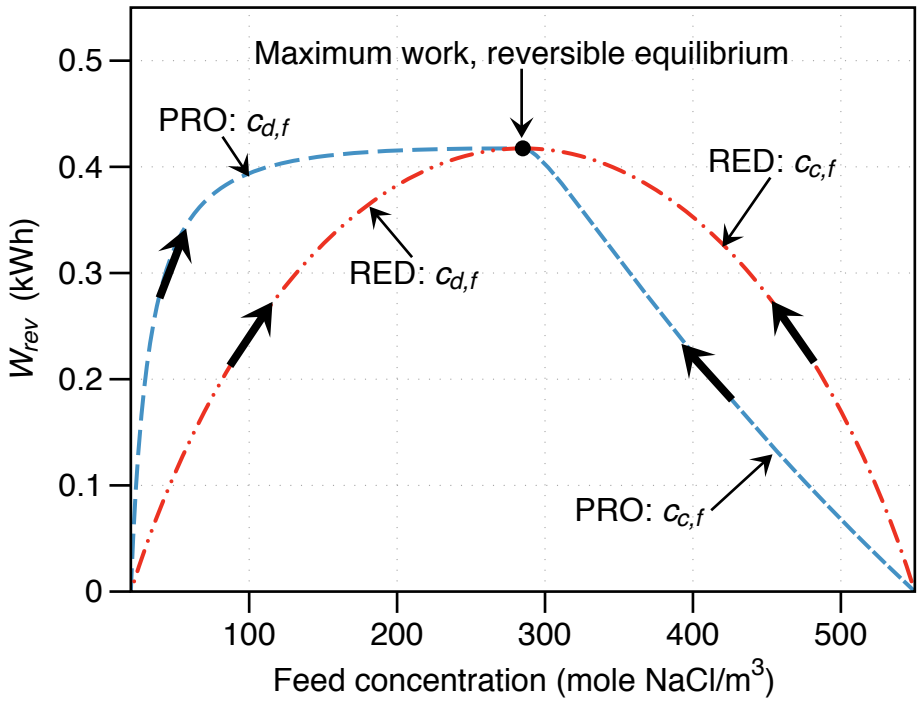

Figure 2.2 The change in reversible work produced by the system (W_{rev}) *versus* the concentration of the feed using **Eq** 2.3 for PRO and **Eq** 2.4 for RED. For a given amount of reversible work, the concentrations of the concentrated and dilute feeds are shown for both PRO and RED. All feeds have the same concentration at the point of maximum reversible work (thermodynamic equilibrium). Arrows on plot lines indicate direction of increased extent of mixing. Here V_c = 1 m^3, V_d = 1 m^3, concentrated feed initial concentration = 550 mol NaCl/m^3, dilute feed initial concentration = 20 mol NaCl/m^3, T = 293.15 K.

Figure 2.3 illustrates the available work produced by PRO and RED relative to the RO feed concentration (diluted effluent from OER_1 concentrated feed). Here the OER concentrated feed extent of mixing corresponds to $r_{mix,c} = 1 - [(c_{c,f} - c_{eq})/(c_{c,i} - c_{eq})]$, where c_{eq} is the concentration associated with reversible equilibrium. As expected, when a constant applied pressure is applied for PRO, the recoverable work decreases. While the maximum power density under a constant applied pressure for PRO is indeed achieved at $\Delta P = \Delta\pi_t/2$, it is clear from the data that more energy can be recovered at lower extents of mixing, e.g., when $\Delta P = \Delta\pi_t/1.5$. The implications of this are important, as less membrane area may be required to operate at lower extents of mixing, which correlates with reduced capital and operation costs. As already noted,

the different values of constant applied pressure shift the equilibrium concentrations of the system. The equilibrium concentration, in turn, corresponds with the maximum extractable energy for a given applied pressure. This configurational loss is not shared by RED, where the cell potential is independent of the applied load [4, 14, 22].

Comparing the results for maximum reversible work, the RED process is capable of achieving greater gross power output at a higher concentrated feed concentration than PRO. Although this behavior does not reveal the technical feasibility of achieving a degree of mixing

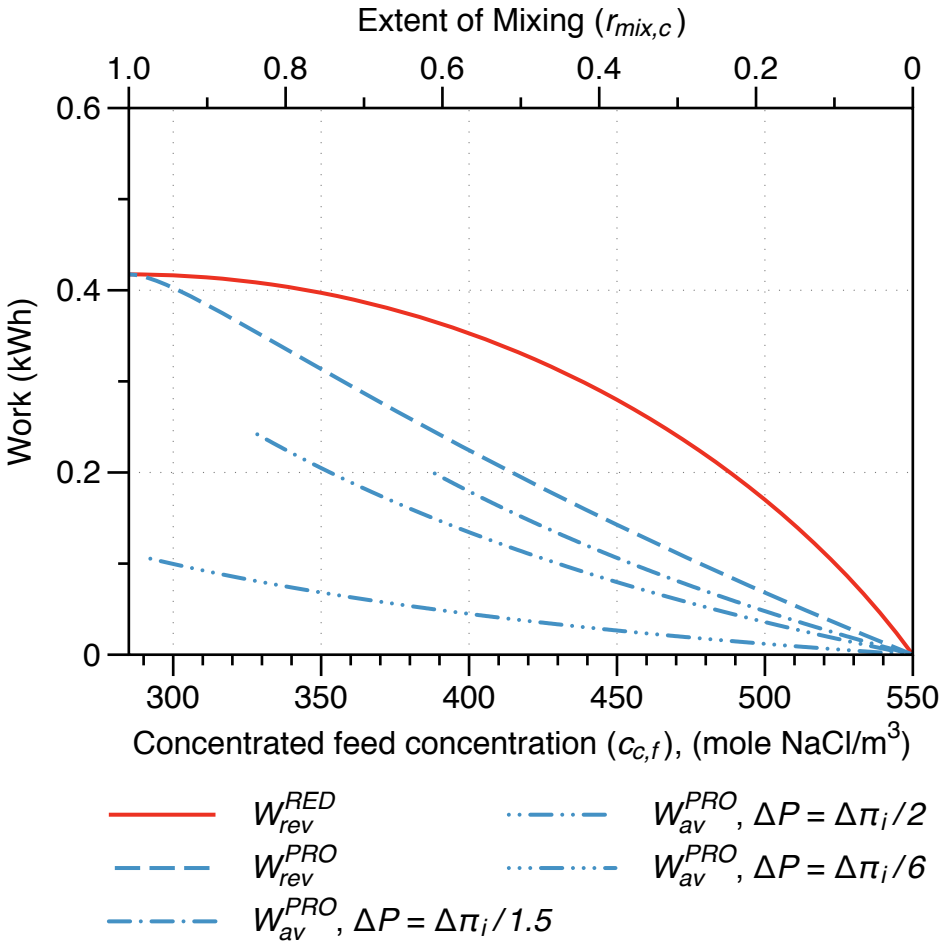

Figure 2.3 The change in work produced by the system *versus* the concentration of the OER concentrated feed for different extents of mixing, for both PRO and RED. **Eq.** 2.3 and 2.4 were utilized for PRO while **Eq.** 2.5 was applied for RED. Here V_c = 1 m^3, V_d = 1 m^3, concentrated feed initial concentration = 550 mol NaCl/m^3, dilute feed initial concentration = 20 mol NaCl/m^3, T = 293.15 K.

with either process, it does provide insight into the maximum potential of each process at a given concentration. The RED data also shows that the recoverable work begins to level off as it approaches its maximum value and this occurs at lower extent of mixing than for PRO. Therefore, if a practical RED process operates at low efficiency, achieving a higher degree of mixing may not be economically justified.

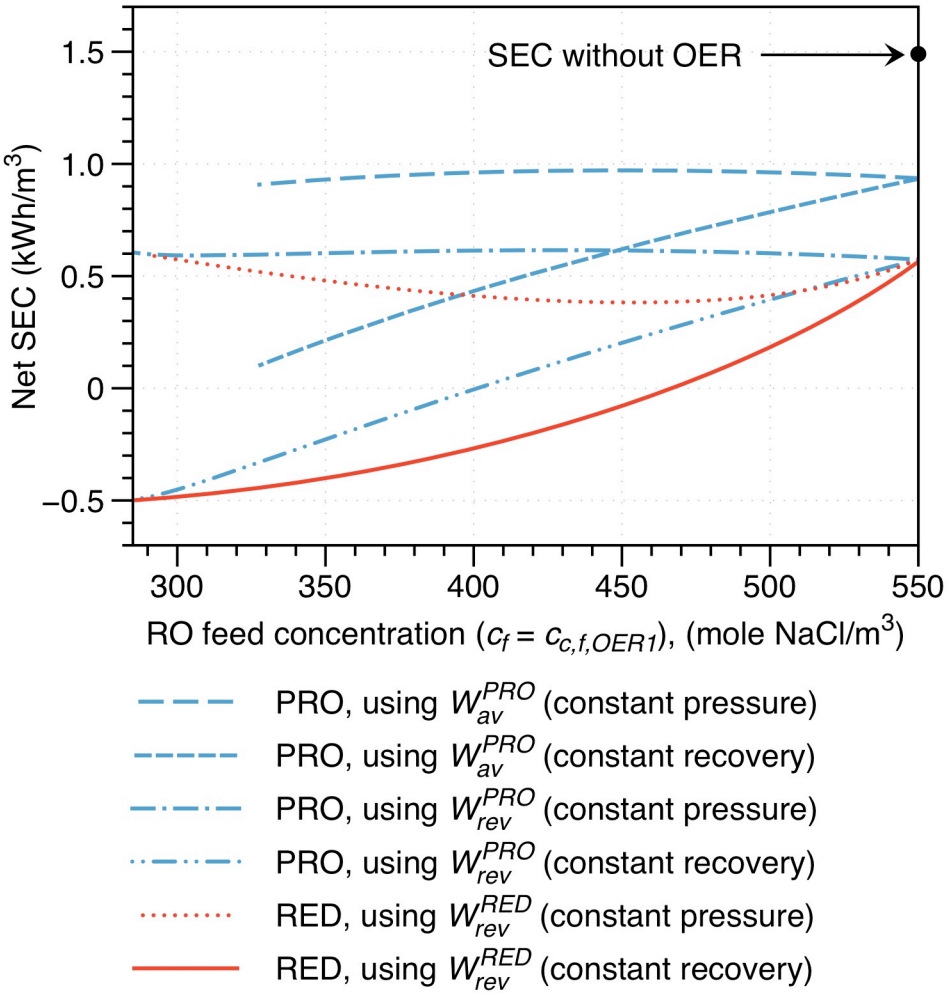

Figure 2.4 Net SEC *versus* RO feed concentration for PRO and RED facilitated OER, with either constant pressure (770 psi) or constant recovery (Y = 0.5) RO operation. $\Delta P = \Delta\pi_i/2$ was used for the available work from PRO-based OER, $\phi = 1$, concentrated feed initial concentration = 550 mol NaCl/m^3, dilute feed initial concentration = 20 mol NaCl/m^3, T = 293.15 K. **Eq.** 2.4 and 2.5 were used to calculate the recoverable energy from PRO and RED, respectively, while **Eq.** 2.6, 2.7, and 2.8 were used for the RO process thermodynamics.

2.3.2 Net SEC for two-stage OER

It has been shown, by Yip and Elimelech[21], that for $\phi = 1$ the recoverable work is maximized at a constant applied pressure of $\Delta P = \Delta\pi_t/2$, Therefore, this pressure was chosen for all the calculations of PRO-facilitated OER using W_{av}^{PRO}. For the *constant pressure* scenario (**Figure 2.4**) using either PRO- or RED-based *OER*, increased extent of mixing in OER_1 (i.e., reducing RO feed salinity) has limited impact on SEC, but proportionally increases RO product water recovery. While there is some osmotic energy recovered, the recoverable energy from the HER decreases in proportion to the decreased RO brine volume (due to higher RO recovery). Furthermore, the recoverable energy from OER_2 is also reduced (due to lower brine volume). In contrast, for the *constant recovery* scenario (also **Figure 2.4**), the net SEC decreases (net energy recovered increases) with increased OER_1 extent of mixing for both PRO and RED based *OER*. At constant recovery, lower salinity RO feeds consume less energy due to reduced feed pressure requirements, while the higher RO brine flow rate enables greater energy recovery by the OER_2 process. In all scenarios, without considering non-ideal process losses (hydraulic, mass transfer, dilute channel resistance, etc.), RED appears to recover more osmotic energy than PRO over most RO feed concentrations, although the reversible work cases for RED and PRO achieve the same energy savings at complete mixing. However, it is important to consider that energy recovery potential is but one metric by which to compare these processes. Ultimately, the ability to extract more of the available potential may be offset by efficiency considerations. For example, capital expenditure is expected to also scale with required membrane area, most commonly associated with power density. Based upon this metric, PRO has been shown to outperform RED by an order of magnitude[13]. Therefore, it is not possible to gauge the actual

preferred technology based on the current results, and they are primarily useful in defining the potential impact on the overall energy consumption for water production.

Figure 2.5 depicts the change in SEC_{net} for constant recovery scenarios ($Y = 0.5$) for both PRO and RED-based OER considering the following options: OER_1 only, OER_1 and OER_2, OER_2 with RO feedwater dilution, and dilution only. Note that OER_1 process reduces the salinity of RO feedwater, but at the capital and operating cost of the OER equipment rather than at the much lower cost of simply blending a lower salinity stream into the RO feedwater (i.e., "dilution"). Of course the benefit of OER technology is the added water quality barrier to pollutant crossover from the dilute stream. An important point most be emphasized here, for as the RO process recovery decreases, the contribution of the OER_1 stage increases. Therefore, to generate the lowest net SEC, flow through the OER devices should be maximized relative to permeate volume, up to a point where the OER_1 infrastructure is oversized and dominates the capital cost of the entire desalination plant.

The combined OER_1 and OER_2 configuration recovered the most energy. It is clear from the results that the energy recovered by OER_1 increases with extent of mixing (i.e., declining RO

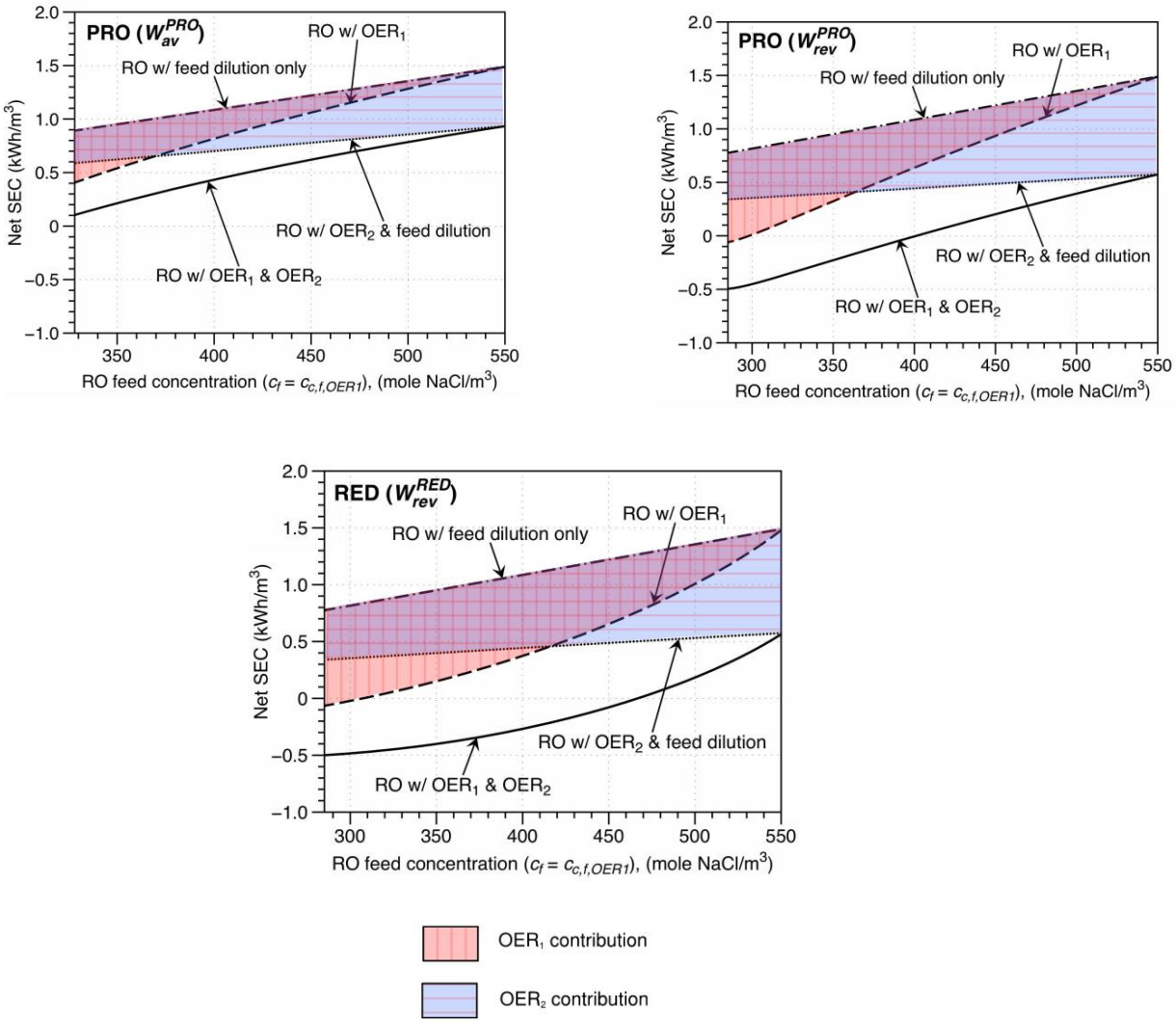

Figure 2.5 Net SEC *versus* RO feed concentration for a coupled process with 1) PRO, using the available work (top, left), 2) PRO, using the full reversible work (top, right), and 3) RED, using the full reversible work (bottom). The figure illustrates the contribution of dilution and individual OER stages, with the hatching indicating the contribution of Stage 1 or Stage 2 OER processes in lowering the net SEC. Note that it is intrinsic for the OER_1 process that dilution occurs and a lower salinity feed is passed to the RO process. Y = 0.5, $\phi = 1$, $\Delta P = \Delta \pi_i/2$ for PRO-based OER, concentrated feed initial concentration = 550 mol NaCl/m^3, dilute feed initial concentration = 20 mol NaCl/m^3, T = 293 K. **Eq.** 2.4 and 2.5 were used to calculate the recoverable energy from PRO and RED, respectively, while **Eq.** 2.6, 2.7, and 2.8 were used for the RO process thermodynamics.

feed concentration) while the energy produced from OER_2 decreases due to a corresponding drop in RO brine concentration. Our results correspond well with the results of the coupled RO-RED study which was recently published [18]. The negative SEC_{net} values output by the model correspond to net energy production from the coupled process. Positive work can be produced from the coupled process due to the mixing of greater volume in the OER_1 process than the volume from which permeate is being extracted in the RO process. That is, we are mixing more volume with PRO or RED than the volume we are 'de-mixing' through RO, resulting in net energy production. The results here show slightly greater potential energy savings than the published article due to the idealized analysis conducted here (i.e. no stack or load resistance).

2.3.3 Economic implications

The energy recoverable by OER could dramatically lower the energy demand and operating cost of seawater RO plants; such energy savings could reduce one of the most significant environmental impacts of seawater desalination. Practical barriers to overcome in developing OER technology include capital, operation, and maintenance costs. Cumulatively, these costs should be less than the reduced costs of RO electricity consumption for OER technology to proliferate like HER technology; in other words, the total cost of water is reduced. Until an actual OER system is built and tested it is difficult to predict the operating costs, so here we will consider projections of potential OER capital costs. Using published data for the amortized cost of electricity over the 20-year life of a 100,000 gallon per day (~380 m^3/day) RO facility[24], it is possible to estimate the capital cost available to accommodate OER infrastructure. As set out in the Desalination Markets 2010 report[24], the cost of electricity was taken as $0.06 per kWh and the interest rate was set at 6% annually. Our results suggest that

energy savings provided by RED-facilitated OER could offset 42% of the total RO plant capital cost, when discounting the capital cost of the OER plant itself (ϕ = 1, c_c = 550 mol/m^3, c_d = 20 mol/m^3, Y = 0.5). Although the energy savings are significant, it must be acknowledged that hydraulic and other process losses are likely to decrease the work produced by the OER plant relative to the reversible work. As the degree of mixing is increased net SEC decreases, but the additional capital cost increases due to the increase in required OER membrane area.

A review of PRO research suggests the capital cost per unit area of membrane eclipses the economic value of the theoretical maximum power produced per square meter over a membrane lifetime of 5 years [25]. It is reasonable to assume that the construction of a membrane-based OER facility (i.e. PRO/RED) designed for, say, a 100,000 m^3 per day RO facility, would have similar requirements of membrane area. High performance RO membranes are priced at approximately 20 $USD/m^2 and modern ion exchange membranes can cost upwards of 200 $USD/m^2 [26]. These costs are not trivial, with membrane capital costs accounting for approximately 6% of the total capital cost of an RO facility and membrane replacement contributing to 7% of operational expenditures[24]. Pumps, pressure vessels, and hydraulic energy recovery capital costs account for only 11% of total RO facility capital costs, and are likely to cost less for the individual OER processes due to operation at lower pressure.

Through the calculation of the recoverable energy from mixing concentrated and dilute waters, it has been possible to provide a rough indication of the available capital for the OER components of a coupled process. Fouling, hydraulic losses, process inefficiencies and other mitigating factors are likely to result in much lower energy savings than the ideal case. At current pricing, OER coupled with RO and HER will be a practical option if OER capital and maintenance costs do not exceed the economic value of energy savings.

Acknowledgements

The authors are grateful for financial support for this research provided by tbe Clean Energy for Green Industry (CGI) NSF IGERT at UCLA. G.Z.R is supported by a Marie-Curie IOF grant under the FP7 program of the European Research Council.

Nomenclature

c	concentration (mol/m^3)
c_{eq}	equilibrium concentration (mol/m^3)
c_b	RO brine concentration (mol/m^3)
c_f	RO feed concentration (mol/m^3)
CF	concentration factor
E	half-cell potential (V)
ΔE	electromotive force (V)
F	Faraday constant (C/mol)
ΔG	free energy of mixing (kWh)
n	moles of salt ions (mol)
Δn	moles of salt ions transferred (mol)
ΔP	PRO applied booster pump pressure (Pa)
ΔP_{RO}	RO applied pump pressure (Pa)
R	Universal gas constant (J/(mol K))
$r_{mix,\,c}$	concentrated feed extent of mixing
SEC_{net}	net specific energy consumption (kWh/m^3)
SEC_{RO}	RO process specific energy consumption (kWh/m^3)
T	temperature (K)
V	volume (m^3)
$\overline{V}$	molar volume of water
V_f	RO feed Volume (m^3)
V_p	RO permeate Volume (m^3)
ΔV	transferred volume (m^3)
W_{rev}^{PRO}	PRO reversible work (kWh/mixed volume)

W_{rev}^{RED}	RED reversible work (kWh/mixed volume)
W_{av}^{PRO}	PRO available work (kWh/mixed volume)
$W_{OER\ 1}$	OER Stage 1 work (kWh)
$W_{\mathrm{OER\ 2}}$	OER Stage 2 work (kWh)
x_w	mole fraction of water
Y	RO process recovery
z	valence of salt ions

Greek Symbols

π	osmotic pressure (Pa)
$\Delta\pi$	osmotic pressure difference (Pa)
ϕ	dilution ratio

Subscripts

f	final
i	initial
c	concentrated
d	dilute

2.4 References

[1] B. Peñate, L. García-Rodríguez, Energy optimisation of existing SWRO (seawater reverse osmosis) plants with ERT (energy recovery turbines): Technical and thermoeconomic assessment, Energy, 36 (2011) 613-626.

[2] M.H. Li, Minimization of Energy in Reverse Osmosis Water Desalination Using Constrained Nonlinear Optimization, Industrial & Engineering Chemistry Research, 49 (2010) 1822-1831.

[3] P. Dlugolecki, A. Gambier, K. Nijmeijer, M. Wessling, Practical Potential of Reverse Electrodialysis As Process for Sustainable Energy Generation, Environmental Science & Technology, 43 (2009) 6888-6894.

[4] J.W. Post, H.V.M. Hamelers, C.J.N. Buisman, Energy recovery from controlled mixing salt and fresh water with a reverse electrodialysis system, Environmental Science & Technology, 42 (2008) 5785-5790.

[5] J. Veerman, M. Saakes, S.J. Metz, G.J. Harmsen, Electrical Power from Sea and River Water by Reverse Electrodialysis: A First Step from the Laboratory to a Real Power Plant, Environmental Science & Technology, 44 (2010) 9207-9212.

[6] A. Achilli, T.Y. Cath, A.E. Childress, Power generation with pressure retarded osmosis: An experimental and theoretical investigation, Journal of Membrane Science, 343 (2009) 42-52.

[7] N.Y. Yip, M. Elimelech, Performance Limiting Effects in Power Generation from Salinity Gradients by Pressure Retarded Osmosis, Environmental Science & Technology, 45 (2011) 10273-10282.

[8] D. Brogioli, R. Zhao, P.M. Biesheuvel, A prototype cell for extracting energy from a water salinity difference by means of double layer expansion in nanoporous carbon electrodes, Energy & Environmental Science, 4 (2011) 772-777.

[9] D. Brogioli, Extracting Renewable Energy from a Salinity Difference Using a Capacitor, Physical Review Letters, 103 (2009) 058501.

[10] D.K. Kim, C.H. Duan, Y.F. Chen, A. Majumdar, Power generation from concentration gradient by reverse electrodialysis in ion-selective nanochannels, Microfluidics and Nanofluidics, 9 (2010) 1215-1224.

[11] X. Cao, X. Huang, P. Liang, K. Xiao, Y. Zhou, X. Zhang, B.E. Logan, A New Method for Water Desalination Using Microbial Desalination Cells, Environmental Science & Technology, 43 (2009) 7148-7152.

[12] M. Mehanna, T. Saito, J. Yan, M. Hickner, X. Cao, X. Huang, B.E. Logan, Using microbial desalination cells to reduce water salinity prior to reverse osmosis, Energy & Environmental Science, 3 (2010) 1114-1120.

[13] G.Z. Ramon, B.J. Feinberg, E.M.V. Hoek, Membrane-based production of salinity-gradient power, Energy & Environmental Science, 4 (2011) 4423-4434.

[14] J.W. Post, J. Veerman, H.V.M. Hamelers, G.J.W. Euverink, S.J. Metz, K. Nymeijer, C.J.N. Buisman, Salinity-gradient power: Evaluation of pressure-retarded osmosis and reverse electrodialysis, Journal of Membrane Science, 288 (2007) 218-230.

[15] E. Brauns, Combination of a desalination plant and a salinity gradient power reverse electrodialysis plant and use thereof, in, 2004.

[16] N.T. Hancock, N.D. Black, T.Y. Cath, A comparative life cycle assessment of hybrid osmotic dilution desalination and established seawater desalination and wastewater reclamation processes, Water Research, 46 (2012) 1145-1154.

[17] L.A. Hoover, W.A. Phillip, A. Tiraferri, N.Y. Yip, M. Elimelech, Forward with Osmosis: Emerging Applications for Greater Sustainability, Environmental Science & Technology, 45 (2011) 9824-9830.

[18] W. Li, W.B. Krantz, E.R. Cornelissen, J.W. Post, A.R.D. Verliefde, C.Y. Tang, A novel hybrid process of reverse electrodialysis and reverse osmosis for low energy seawater desalination and brine management, Applied Energy, 104 (2013) 592-602.

[19] P. Xu, J.E. Drewes, C. Bellona, G. Amy, T.-U. Kim, M. Adam, T. Heberer, Rejection of Emerging Organic Micropollutants in Nanofiltration-Reverse Osmosis Membrane Applications, Water Environment Research, 77 (2005) 40-48.

[20] X. Tongwen, Ion exchange membranes: State of their development and perspective, Journal of Membrane Science, 263 (2005) 1-29.

[21] N.Y. Yip, M. Elimelech, Thermodynamic and Energy Efficiency Analysis of Power Generation from Natural Salinity Gradients by Pressure Retarded Osmosis, Environmental Science & Technology, 46 (2012) 5230-5239.

[22] J. Veerman, M. Saakes, S. Metz, G. Harmsen, Reverse electrodialysis: A validated process model for design and optimization, Chemical Engineering Journal, 166 (2011) 256-268.

[23] A. Zhu, P.D. Christofides, Y. Cohen, Effect of Thermodynamic Restriction on Energy Cost Optimization of RO Membrane Water Desalination, Industrial & Engineering Chemistry Research, 48 (2009) 6010-6021.

[24] G.W.I. (GWI), Desalination Markets 2010, (2010).

[25] A. Achilli, A.E. Childress, Pressure retarded osmosis: From the vision of Sidney Loeb to the first prototype installation - Review, Desalination, 261 (2010) 205-211.
[26] FilmTec Price List, http://www.formembranes.com/FTP.pdf, 2011

3 DEVELOPMENT OF FULL-SCALE PROCESS MODELS FOR PRESSURE RETARDED OSMOSIS AND REVERSE ELECTRODIALYSIS

3.1 Introduction

Clean, renewable energy may be produced by controllably mixing streams of different salinity [1, 2]. This is achieved by employing membranes that facilitate selective transport of either solute or solvent, resulting in different process characteristics with various advantages and disadvantages. Pressure-retarded osmosis (PRO) and reverse electro-dialysis (RED), the two most popular salinity gradient power (SGP) technologies, are discussed in detail in the literature (see, for example, refs [1, 3-8]). While both PRO and RED involve mixing dilute and concentrated solutions, the energy conversion mechanism achieved via mixing is fundamentally different. PRO involves the diffusion of water molecules across a semipermeable membrane from a dilute feed stream into a pressurized concentrated stream, augmenting its volume upon dilution. The volume-augmented concentrated feed is then passed through a hydro-turbine where the mechanical energy is converted into electricity. RED involves the diffusion of salt ions across ion exchange membranes, creating an ionic flux that is converted into an electron flux at electrodes, and power is harnessed through an applied load in an external circuit.

Previous modeling work on SGP technologies has focused on the maximum power density produced through PRO or RED. However, maximum power density alone is an insufficient metric for designing a large-scale, realistic SGP system. Even in an ideal system, maximum power density will only be achieved at the system inlet where the concentration gradient is largest, but downstream mixing of the streams inevitably lowering the power density. Conversely, energy efficiency, defined as the ratio of produced to available energy, is maximized at the point of complete mixing, which would theoretically occur at the system outlet. However, complete mixing would require infinite system size (or residence time). Therefore, in order to evaluate the scale-up of SGP technologies, it is essential to first understand how system-level

power density and energy efficiency (and therefore total power output) change with module length (a proxy for system size).

A full-scale process model accounting for changes in velocity, pressure, and concentration along the length of the flow channels can provide a direct, quantitative indication of these important process metrics. To the best of our knowledge, a detailed process model has yet to be published for PRO. For RED, a full-scale process model was already proposed [9]; however, it was employed for the purpose of comparison with experimental measurements on a small scale system and was not used to evaluate full-scale performance. Moreover, the model did not consider external mass transfer, which is significantly impacts performance at low crossflow velocity [2]. A recent study by Vermaas et al. applied a process model to evaluate changes in energy recovery and power density over relatively short lengths, but did not account for membrane resistance, viscous dissipation, or concentration polarization [10]. Furthermore, detailed comparisons of PRO and RED previously published have considered the maximum power density achievable, but did not consider how both energy efficiency and average power density would comparatively scale with system size.

The purpose of this paper is to identify how full-scale performance varies with the main process parameters. In particular, this is the first time that PRO performance has been evaluated a full-scale process model. Note that the two processes modeled are envisioned with different system dimensions and operating principles; hence, comparing PRO and RED is naturally a difficult task. Therefore, the results presented herein are designed to illustrate the potential of a full-scale process model and the extension of that model to practical scale-up considerations. The results are not intended to be a prescriptive statement on which process is technologically superior. Furthermore, although PRO and RED can be envisioned as multi-stage processes, we

only consider a single stage (single hydro-turbine and single electrode for PRO and RED, respectively). Finally, only co-current cases are considered here; cross-current or counter-current configurations could produce different results.

3.2 Model formulation

In this section, one-dimensional process models are developed for both PRO and RED, in the spirit of previous efforts to model full-scale reverse osmosis systems [11-14]. In this framework, cross-sectional variations of velocity and concentration in the flow channels are not explicitly solved for. Instead, mass transfer correlations are used to account for external concentration polarization (in the case of PRO, internal concentration polarization is accounted for as well), and a friction factor is used to account for viscous dissipation. This results in a significant computational simplification, producing a coupled system of non-linear ordinary, rather than partial, differential equations. Through employing this flexible approach, operational parameters can be more rapidly adjusted and evaluated over a wider range as compared with more computationally intensive approaches such as computational fluid dynamics (CFD). A one-dimensional model is the first step toward approximating scale-up of salinity gradient energy and requires much less computational power than more complex modeling techniques. While, over short lengths CFD can be of great use, over longer system lengths (many meters) it is not computationally rational to apply two- and three- dimensional approaches. We note that good correlation between one-dimensional models and experimental data has been reported in the past for the fouling of reverse osmosis systems [15]. In the present formulation, other inefficiencies are included, such as co-ion transport and salt leakage, hydraulic losses within the module, and machine inefficiencies (pumps, hydro-turbine, hydraulic energy recovery device).

Mass and momentum balances applied to each channel yield the system of governing ordinary differential equations for transport in each process. Equations 3.1 - 3.3 describe changes in crossflow velocity *u(x)*, solute concentration *c(x)*, and pressure *p(x)*, with position *x* (module length) in the dilute and concentrated channels, *viz*.

$$\frac{du}{dx} = \pm\frac{2J_w}{h} \tag{3.1}$$

$$\frac{d(uc)}{dx} = \pm\frac{2J_s}{h} \tag{3.2}$$

$$\frac{dp}{dx} = -\frac{\lambda\rho u^2}{2d_h} \tag{3.3}$$

where h is the PRO or RED module channel height, ρ is the density of water, d_h is the hydraulic diameter of the channel, J_w is the water flux across the membrane, J_s is the salt flux, and λ is the friction factor coefficient. An exhaustive study was conducted in order to identify useful friction factor correlations in the literature. Many correlations have been developed for different flow geometries and Reynolds numbers. Here were apply a friction factor correlation which is relevant to the range of conditions modeled in this study [16]. The friction factor coefficients used in determining the hydraulic losses within each channel were calculated through

$$\lambda = \omega_1 - \frac{\omega_2}{\mathrm{Re}^{\omega_3}} \tag{3.4}$$

where ω_1 , ω_2 , and ω_3 are fitting parameters obtained from computational fluid dynamics [16]. For the case of circular spacers with a diameter half the channel height, and 4.5 mm filament spacing, the values of these parameters are $\omega_1 = 0.42$, $\omega_2 = 189.29$, and $\omega_3 = 1$. Please see the Supporting Information for more details on our approach to the friction factor correlation.

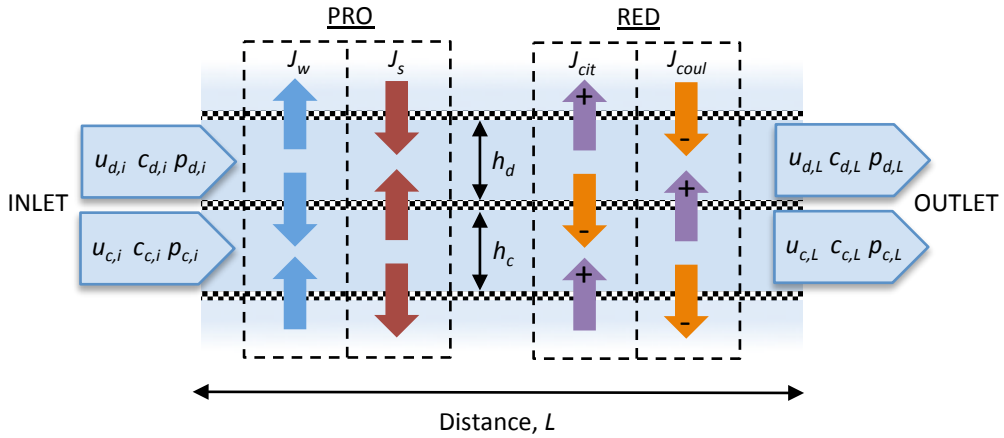

Figure 3.1 Graphical representation of a unit "cell" for PRO and RED. Note that initial flow conditions are denoted by the subscript i, while conditions at a given module length L are represented by subscript L. PRO involves water flux (J_w) and salt flux (J_s), while RED consists of a co-ion transport flux (J_{cit}) and Coulombic flux (J_{coul}) for positive and negative ions.

A graphical representation of a single PRO or RED membrane "cell" is shown in **Figure 3.1**. Note that in **Eq.** 3.1 and 3.2, negative and positive signs signify mass loss/gain, respectively, occurring in the dilute and concentrated channel. Furthermore, we define the dilution ratio, i.e., the ratio of dilute to concentrated channel flow rates, as

$$d_r = \frac{q_d}{q_c}. \tag{3.5}$$

The dilution ratio has a fundamental impact on the energy efficiency achieved during mixing, as well as the total power extracted. It is distinctly a feature of large-scale implementation and therefore such effects have not received attention in the laboratory-scale literature.

3.2.1 Water and salt fluxes

3.2.1.1 PRO

Water flux in PRO is a function of the bulk solute concentrations (and hence, the osmotic pressure), salt diffusivity D, external mass transfer coefficient k_c, universal gas constant R, temperature T, and membrane permeability to water A, and salt B [5]. In order to account for the impact of non-ideality in the osmotic pressure, a correction factor must be applied. The actual osmotic pressure (π_{actual}) and the ideal osmotic pressure (π_{ideal}) can be related through the concentration-dependent osmotic coefficient (ϕ),

$$\phi = \frac{\pi_{actual}}{\pi_{ideal}} = \frac{(RT/\bar{V})\ln a_w}{2RTc}. \tag{3.6}$$

where the numerator is the actual osmotic pressure and considers the activity of water (a_w), and thus non-ideality, and the denominator is the idealized van't Hoff approximation for osmotic pressure. Here, $\bar{V}$ is the molar volume of water and c is the molar concentration of the solution. Using published reference data [17, 18], it is possible to construct a numerical correlation to determine the osmotic coefficient of water at a given concentration (i.e. $\phi = f(c)$). Please see the Supporting Information for further details on the numerical correlation applied in this study. The membrane interface concentrations (subscript m) for the dilute and concentrated feeds subscripts (subscripts d and c, respectively) are defined as [19]

$$c_{c,m} = c_{c,b}\exp\left(\frac{-J_w}{k_c}\right) - \frac{B}{J_w}(c_{c,m} - c_{d,m})\left[1 - \exp\left(\frac{-J_w}{k_c}\right)\right]. \tag{3.7}$$

and

$$c_{d,m} = c_{d,b}\exp\left(\frac{J_w S}{D}\right) + \frac{B}{J_w}(c_{c,m} - c_{d,m})\left[\exp\left(\frac{J_w S}{D}\right) - 1\right] \tag{3.8}$$

where
$$c_{c,m} - c_{d,m} = \frac{c_{c,b}\exp\left(\frac{-J_w}{k_d}\right) - c_{d,b}\exp\left(\frac{J_w S}{D}\right)}{1 + \frac{B}{J_w}\left[\exp\left(\frac{J_w S}{D}\right) - \exp\left(\frac{-J_w}{k_c}\right)\right]}. \quad (3.9)$$

Here, S is the structure factor, dependent on the porosity, tortuosity and thickness of the membrane support layer, which dictates the severity of salt accumulation within it (internal concentration polarization). We apply $\pi_{actual} = \phi 2RTc$ (from **Eq.** 3.6) to calculate the actual osmotic pressure difference between the two feeds, with $c = c_{d,m}$ and $c = c_{c,m}$ for $\pi_{actual,d}$ and $\pi_{actual,c}$, respectively. Here, the value of the osmotic coefficient is determined from the constructed correlation and is calculated for both the concentrated and dilute solution membrane interface concentrations ($\phi_{c,m}$, and $\phi_{d,m}$, respectively). The flux can then be determined through

$$J_w = A(\Delta\pi_{actual} - \Delta p) \quad (3.10)$$

where $\Delta\pi_{actual} = \pi_{actual,c} - \pi_{actual,d}$, $\Delta p = p_c - p_d$ and is the applied pressure difference between the two feeds, and A is the membrane hydraulic permeability.

The salt flux (or "salt leakage") is assumed to be purely diffusive and, accounting for concentration polarization effects, is given by [5]

$$J_s = B\left[\frac{c_c e^{-J_w/k_c} - c_d e^{J_w S/D}}{1 + \frac{B}{J_w}(e^{J_w S/D} - e^{-J_w/k_c})}\right]. \quad (3.11)$$

3.2.1.2 RED

The RED salt flux is composed of both a Coulombic (J_{coul}) and co-ion transport (J_{cit}) components, i.e. $J_s = J_{coul} + J_{cit}$ [9]. The Coulombic flux component can be described by

$$J_{coul} = \frac{\Delta V_{mem} - \Delta V_{load}}{F r_{stack}} \ , \tag{3.12}$$

where F is the Faraday constant, ΔV_{load} is the voltage drop across the external load, r_{stack} is the internal stack resistance incorporating average ion exchange membrane resistance (r_{mem}), as well as dilute (r_d), and concentrated (r_c) channel resistances. The potential difference across the membrane, ΔV_{mem}, is defined as

$$\Delta V_{mem} = \frac{\alpha 2RT}{F} ln \frac{\gamma_{c,m} c_{c,m}}{\gamma_{d,m} c_{d,m}}, \tag{3.13}$$

where α is the average permselectivity, and $\gamma_{c,m}$ and $\gamma_{d,m}$ are the sodium chloride activity coefficients for the concentrated and dilute solutions, respectively, as a function of membrane concentration [9]. As with the osmotic coefficient for PRO, here we construct a numerical correlation relating sodium chloride activity to concentration using data from the literature [17, 18]. Details for the numerical correlation are included in the Supporting Information. The subscript m refers to the membrane interface concentration and is related to the bulk concentration (c_b) generally via

$$c_m = c_b \pm \frac{J_{coul}}{k_c}, \tag{3.14}$$

which accounts for ion accumulation (depletion) at the membrane surface in the dilute (concentrated) channel. Since $J_{coul} >> J_{cit}$, we only consider the effect of the Coulombic flux in concentration polarization. The co-ion flux component is defined as

$$J_{cit} = \frac{D_{mem}}{\delta_{mem}} \left(c_{c,m} - c_{d,m} \right) \ , \tag{3.15}$$

where the salt diffusion coefficient within the membrane is denoted by D_{mem} and the thickness of the membrane by δ_{mem} [9]. We assume negligible net osmotic flux through the ion exchange membranes due to the competing contributions of osmosis and electro-osmosis [20].

3.2.1.3 External mass transfer

The feed side external mass transfer coefficients were determined using correlations for a rectangular, spacer filled channel. As with the friction factor coefficient detailed in the earlier section, an exhaustive review of the available literature was conducted in order to identify the most useful correlations. Please see the Supporting Information for more details on our approach to the mass transfer coefficient. The chosen correlations were specifically derived for RO but here we apply them for both PRO and RED. The mass transfer coefficient, k, can be calculated via [16],

$$k_c = 0.46(\mathrm{ReSc})^{0.36}\frac{D}{d_h} \tag{3.16}$$

where $\mathrm{Re} = ud_h\rho/\mu$ is the Reynolds number (i.e. the ratio of inertial to viscous forces in a flow), where μ is the dynamic viscosity of the solution, and $\mathrm{Sc} = \mu/\rho D$ is the Schmidt number (i.e. the ratio of typical time scales for diffusive momentum and mass transport).

3.2.1.4 Applied pressure and load voltage

In order to produce power in real systems, a hydraulic pressure (for PRO) or load voltage/resistance (for RED) must be applied. In PRO, the applied pressure corresponds to some multiple, represented here as (*1/f*) of the total available pressure difference ($\Delta\pi$) between the dilute and concentrated feeds. Here, f is termed the load factor, where the value of f must be

greater than unity for the process to operate in PRO mode. The initial osmotic pressure difference is given by $\Delta\pi_i = \phi_{c,b} 2RTc_{c,b} - \phi_{d,b} 2RTc_{d,b}$, here using the bulk (and not the membrane interface) concentration difference between the dilute and concentration feeds. Bulk concentrations are used since the membrane interface concentrations are a function of the water flux, and therefore, the membrane properties and geometric proportions of the channel. By using the bulk concentration, the applied pressure is a property of the solution properties alone. Likewise, in RED, the load voltage is represented as (*1/f*), taken here relative to the initial potential difference (ΔE), where the open circuit voltage is given by $\Delta E_i = \left(2RT/F\right)\ln\left(\gamma_{c,b}c_{c,b}/\gamma_{d,b}c_{d,b}\right)$. As with PRO, here bulk concentrations are used instead of membrane interface concentrations. For both processes, ignoring viscous dissipation, maximum power density is achieved when the applied pressure difference or load voltage is exactly half of the available osmotic pressure or open circuit voltage, i.e. $\Delta p = \Delta\pi/2$ and $\Delta V = \Delta E/2$, where Δp is the difference in hydraulic pressure between the feeds and ΔV is the applied load voltage [1]. In a large-scale system where pressure and concentration vary with length, the applied pressure must be adjusted to account for these changing conditions. Hence, for PRO we define the initial dilute feed pressure as the minimum pressure necessary to overcome hydraulic losses in the dilute channel and define the initial concentrated feed pressure (which is far in excess of the dilute feed pressure) to equal

$$p_{c,i} = \frac{\Delta\pi_i}{f} + p_{d,i} - p_{d,L}, \tag{3.17}$$

where $\Delta\pi_i$ is the initial osmotic pressure difference between the concentrated and dilute solutions, $p_{d,i}$ and $p_{d,l}$ are the initial dilute feed applied pressure and the applied pressure of the dilute feed at some distance *L*. As noted earlier, for maximum power density in an idealized, constant pressure

system, $f = 2$; however, as will be shown, this condition does not necessarily correspond to maximum power density or energy efficiency in a real system.

For RED, the applied load is not linked with dissipation due to module length as in PRO, and therefore the applied load is defined as

$$\Delta V_{load} = \frac{\Delta E_i}{f}, \tag{3.18}$$

where ΔE_i is the initial potential difference between the concentrated and dilute channel.

3.2.1.5 Net power and power density

In general, the maximum, reversible power P_{rev} that can be extracted from mixing a dilute feed and a concentrated feed can be written as

$$P_{rev} = 2RT\left(q_{d,i}c_{d,i}ln\frac{c_{d,i}}{c_{eq}} + q_{c,i}c_{c,i}ln\frac{c_{c,i}}{c_{eq}} \right), \tag{3.19}$$

where c_{eq} is the equilibrium concentration at complete mixing,

$$c_{eq} = \frac{c_{c,i} + d_r c_{d,i}}{1 + d_r}. \tag{3.20}$$

In the PRO configuration envisioned here, only the permeate flow is passed through the hydroturbine while the initial flow is passed through a hydraulic energy recovery (HER) device where energy is exchanged with the concentrated feed prior to flow through a high pressure pump. Because the HER device efficiency is greater than the efficiency of the hydroturbine, for PRO we assume that only the water transported across the membrane is passed through the hydroturbine, while the remaining flow is passed through a hydraulic energy recovery (HER) device. The net power generated for a module of a given length, L, can be determined by

subtracting the contribution of the pumping energy demand for the dilute and concentrated feeds from the power generated by the hydroturbine, i.e. $P_{net} = P_{ht} - P_{p,}$ where

$$P_{ht} = \eta_{ht} b h_c p_{c,L} \int_0^L J_w dx \tag{3.21}$$

and

$$P_p = \frac{q_{c,i}}{\eta_p}(p_{c,i} - \eta_{her} p_{c,L}) + \frac{q_{d,i}}{\eta_p}(p_{d,i} - p_{d,L}), \tag{3.22}$$

where η_{ht} , η_p and η_{her} denote the efficiencies of the hydroturbine, pump and, hydraulic energy recovery device, respectively, and b is the width (hereafter taken as unity). The first term on the right hand side of **Eq.** 3.22 is the power necessary to pump the concentrated feed, where the energy consumption is reduced due to the contribution of the HER) device.

In RED the net power is calculated by determining the power dissipated by the external load, and subtracting the pumping power demand for the concentrated and dilute feeds, i.e. $P_{net} = P_{load} - P_p$, where

$$P_{load} = bF\Delta V_{load} \int_0^L J_{coul} dx \tag{3.23}$$

and

$$P_p = \frac{q_{c,i}(p_{c,i} - p_{c,L}) - q_{d,i}(p_{d,i} - p_{d,L})}{\eta_p} \ . \tag{3.24}$$

The system-level power density, for both PRO and RED, can be calculated by dividing the net power by the total membrane area,

$$P_d = \frac{P_{net}}{2bL} \ , \tag{3.25}$$

where division by 2 accounts for the fact that there are two membranes in a single unit cell. Power density is the quantity most frequently used in the literature for comparing RED vs. PRO process performance. Here we define the total process efficiency as the total generated power (or work) divided by the theoretical power (or work) available with completely reversible mixing

$$\eta = \frac{P_{net}}{P_{rev}}. \tag{3.26}$$

Note that this value corresponds to the fraction of the reversible work, and not the available work, that is recovered through mixing [8]. Since the reversible (but not the available) work is the same for PRO and RED, this approach maintains continuity in the analysis.

3.2.1.6 Solution methodology

The non-linear system of ordinary differential equations [**Eq.** 3.1, 3.2, and 3.3] and algebraic constraints [**Eq.** 3.10**,** 3.11**,** 3.12**,** and 3.15] outlined above for each process, were solved using the freely-available APMonitor modeling environment [21]. For the present study, state-of-the-art commercially available membranes were applied in the process modeling, namely, the Oasys thin film composite (TFC) forward osmosis (FO) membrane was used for PRO, while the Neosepta AMX-CMX and Fumasep FKD-FAD anion exchange-cation exchange membrane pair was applied for RED. The dilute feed (treated wastewater or river water) concentration is taken as 17 mol/m^3 NaCl while the concentration feed (seawater) concentration is taken as 513 mol/m^3. **Table 3.1** lists the values of different process parameters used in the simulations. Unless otherwise stated, crossflow velocities for both RED and PRO are taken as 0.02 m/s for all

process simulations. A brief comparison of our modeling results with published experimental data from a 1 meter long PRO module [22] is included in the Supporting Information. Unfortunately, we have only been able to conduct this analysis for PRO, since we could not find any comparable experimental data for RED. Calculations illustrate that the water flux from our model is in very reasonable agreement with water flux reported from the module size study, especially at lower applied pressures. We note that discrepancies may inherently present themselves due to uncertainty in the choice of parameters in the experimental study, as well as the specific module geometry used.

Table 3.1 Overview of process parameters.

Parameter	**Value**	**Reference**
PRO:		
Membrane hydraulic permeability, A	9.56×10^{-12} m/(s Pa)	[23]
Membrane salt permeability, B	1.31×10^{-7} m/s	[23]
Membrane structure factor, S	434 microns	[23]
Channel height, h	700 microns	
RED:		
Average membrane resistance, r_{cem}	2.63×10^{-4} Ω/m^2	[1]
Average permselectivity, α	0.949	[1]
Channel height, h	200 microns	
General:		
Pump efficiency, η_p	0.89	[24]
Hydroturbine efficiency, η_{ht}	0.90	[24]
HER device efficiency, η_{her}	0.95	[8]
Solution molar conductivity	0.01287 (S m^2)/mol	[10]
Temperature, T	293 K	

Note that, as the model predicts that mixing will proceed until the driving force is infinitesimally small, some threshold must be set in order to determine the relative location of equilibrium. Therefore, $J_w \approx 0$ and $J_{coul} \approx 0$ actually correspond to prescribed values where $J_w =$

10^{-9} m s^{-1} and J_{coul} =10^{-10} mol m^{-2} s^{-1}. These values correspond to approximately 0.1% of the initial flux for PRO and RED when operating under the conditions listed in **Table 3.1** and at crossflow velocity u = 0.02 m/s and load factor f = 2.

3.3 Results and Discussion

3.3.1 Properly calculating power density

The commonly accepted method to assess the power density in PRO is to multiply the experimentally determined flux (i.e. average flux, $\overline{J}_w$) by the (constant) concentrated feed applied pressure, i.e. $P_d = \overline{J}_w p_{c,i}$. However, this method grossly overestimates the actual power density achievable in a PRO module since it ignores the contribution of hydraulic losses and machine (hydroturbine, pump, and HER device) inefficiencies. In **Figure 3.2**, the power density has been calculated using both the commonly published method and through the method discussed in **Eq.** 3.25 which incorporates losses. It is clear from the results that there is a significant impact on the power density from incorporating these losses. Although it is not surprising that hydraulic losses reduce the achievable power density, there is also an unforeseen impact due to machine inefficiency. In fact, when operating at a relatively low crossflow velocity (and correspondingly low hydraulic losses), the efficiency of the hydraulic energy recovery device becomes the primary contributor to reduced power density. This effect shifts the power density to negative values at short module length. The reduced power density can be explained due to the high pressures needed on the concentrated solution side in order to operate near the optimum power density. For example, although current HER devices can operate at $\eta_{her} > 0.95$, the energy lost when transferring pressure (energy) to the PRO concentrated feed from the PRO

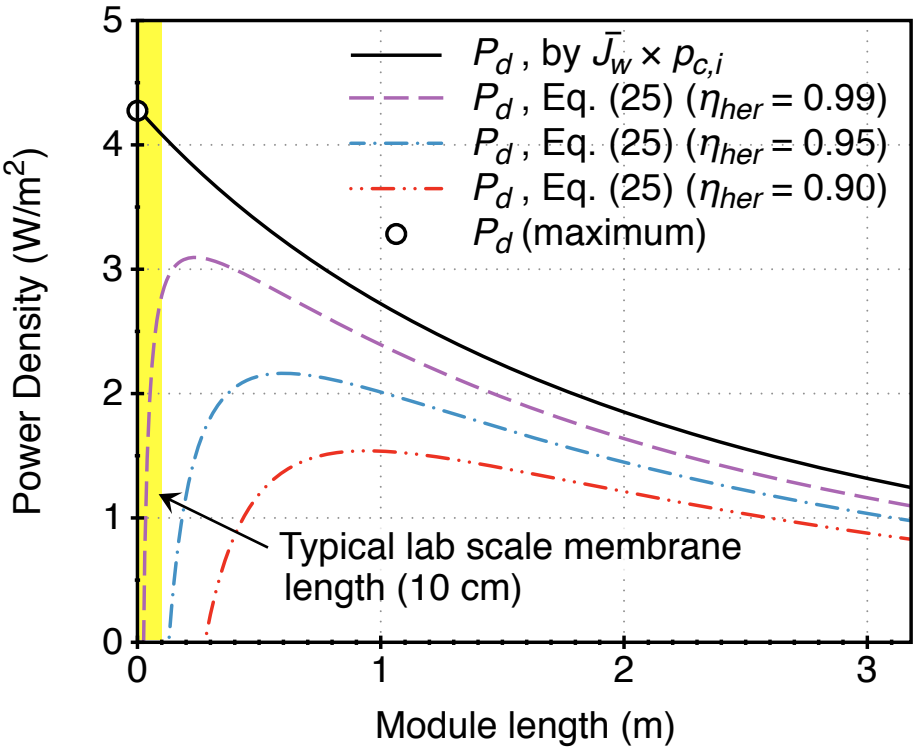

Figure 3.2 Change in PRO power density with module length, using different calculation methods. Note that the commonly accepted method for extrapolating the power density from experimental data (black line) results in much higher power density than when losses and inefficiencies are considered. The yellow shaded area represents the region where most power density measurements are observed in the laboratory due to small-scale experimental design. All calculations for PRO were made with f = 2, and u = 0.02 for both channels.

brine, i.e. $(1-\eta_{her})p_{c,L}\, q_{c,i}$, is still very significant when $p_{c,L}$ is large. Further increasing the already high value of η_{her} may not be feasible. Note that the size of most laboratory scale PRO membranes is on the order of centimeters rather than meters, and therefore only power density near the maximum value is reported. Due to the efficiency considerations shown, a membrane module of this length will in fact have low or negative power density depending on the efficiency of the HER device.

Since RED does not require a significant applied pressure in order to extract energy, RED lacks the HER device commonly included in the PRO configuration. Therefore, the change in the

power density profile at short module length due to HER device inefficiency is not observed for RED. This distinction is a particularly important difference between PRO and RED. For RED, power density is maximized at infinitely short module length (see later sections) while for PRO there exists a maximum power density when module length is appreciably greater than zero. Of course, since both the actual value of maximum power density and the associated membrane/module cost are different for each process, this does not imply that either process is inherently superior. A full scale cost analysis is necessary to determine with which process the dollar invested per unit energy produced can be maximized.

3.3.2 Change in applied pressure and load

In order to provide a useful indication of the relative process performance at different operating conditions, the developed model has been used to calculate both power density and efficiency. **Figure 3.3** shows how these metrics change with system length when operating at different load factors. Power density (which is obtained from the total, system-integrated power divided by the membrane area), indicates the system-level average productivity of the total available membrane area. Note that here, it may indeed be treated as an average property, rather than a local one based on the flux at a given position in the system. In a system that does not account for losses, power density is maximized for an infinitesimally short system length (where no dilution occurs), while efficiency is maximized at equilibrium – complete mixing. However, here we can see that, especially for the case of PRO (**Figure 3.3**a), power density is not maximized until approximately 0.5 m of system length. Again, this shift in maximum power density is due to the inclusion of pump, hydroturbine, and pressure exchanger inefficiencies. These require that a finite amount of power actually be consumed by the system to overcome inherent losses.

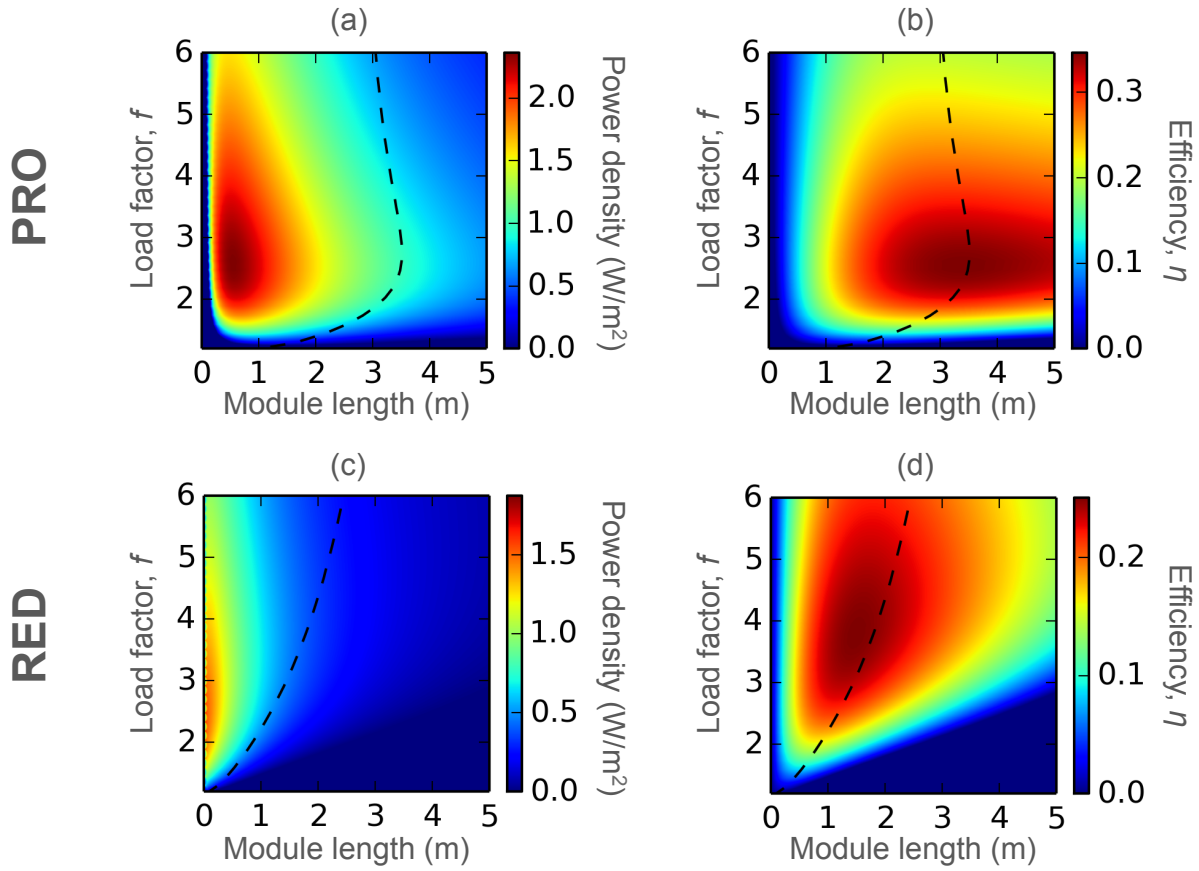

Figure 3.3 Change in power density and efficiency for PRO (a,b) and RED (c,d), with variation in load factor and module length. The dashed black line on all plots corresponds to the module length at which mixing approaches equilibrium (i.e. $J_w \approx 0$ for PRO and $J_{coul} \approx 0$ for RED) for the given set of operational conditions. All simulations conduced at a crossflow velocity of u = 0.02 m/s for both the concentrated and dilute feed channels.

System-averaged power densities here approach 2.0 W/m^2 for RED and surpass 2.5 W/m^2 for PRO.

While power density and efficiency appear to be maximized at approximately the same load factor for PRO, this does not occur at $f = 2$, as predicted theoretically[1, 3, 5]. Rather, maximization occurs at $f \approx 2.5$, meaning that a significantly lower applied pressure is necessary compared to the ideal case, due to process inefficiencies and dilution. In RED, efficiency is highest at $f \approx 3.8$ while power density is maximized at $f \approx 2.1$, again suggesting there is a significant gap between the real and idealized cases. The dashed black lines shown on the plots

in **Figure 3.3** represent the module length corresponding to equilibrium for each applied load factor. For PRO, the maximum value for module length lies at the load factor maximizing efficiency and power density.

3.3.3 Change in crossflow velocity

The crossflow velocity is an operational parameter that appears to fundamentally impact process performance. Velocity variation has been modeled in two ways, 1) the dilution ratio has been set to unity and the concentrated and dilute feed velocities varied together over a selected range, and 2) the sum of the concentrated and dilute feed velocities has been set constant at 0.04 m/s with the dilution ratio varied. This does not mean that the same flow rates apply for PRO and RED at a given dilution ratio. Rather, crossflow velocities are the same for PRO and RED, but due to the different channel heights for each process the flow rates are necessarily different. This approach was taken in order to capture comparable power densities for both processes. For example, applying a relatively high flow rate for PRO will produce a relatively higher power density, but applying the same flow rate for RED may result in unacceptably high viscous dissipation in the flow channels due to higher crossflow velocity. This is a consequence of the two processes possessing fundamentally different engineering constraints. **Figure 3.4** depicts the change in power density and efficiency, for PRO and RED with change in velocity at constant dilution ratio. For PRO (**Figure 3.4**a-b), it is clear that the power density and efficiency diminish significantly above 0.1 m/s. This result is particularly interesting since the proposed "standard method" for testing FO and PRO membranes is at a crossflow velocity of 0.25 m/s [25], and it appears that such a high crossflow velocity may be impractical in a large-scale implementation of PRO for energy generation. A similar change in crossflow velocity for RED results in an even

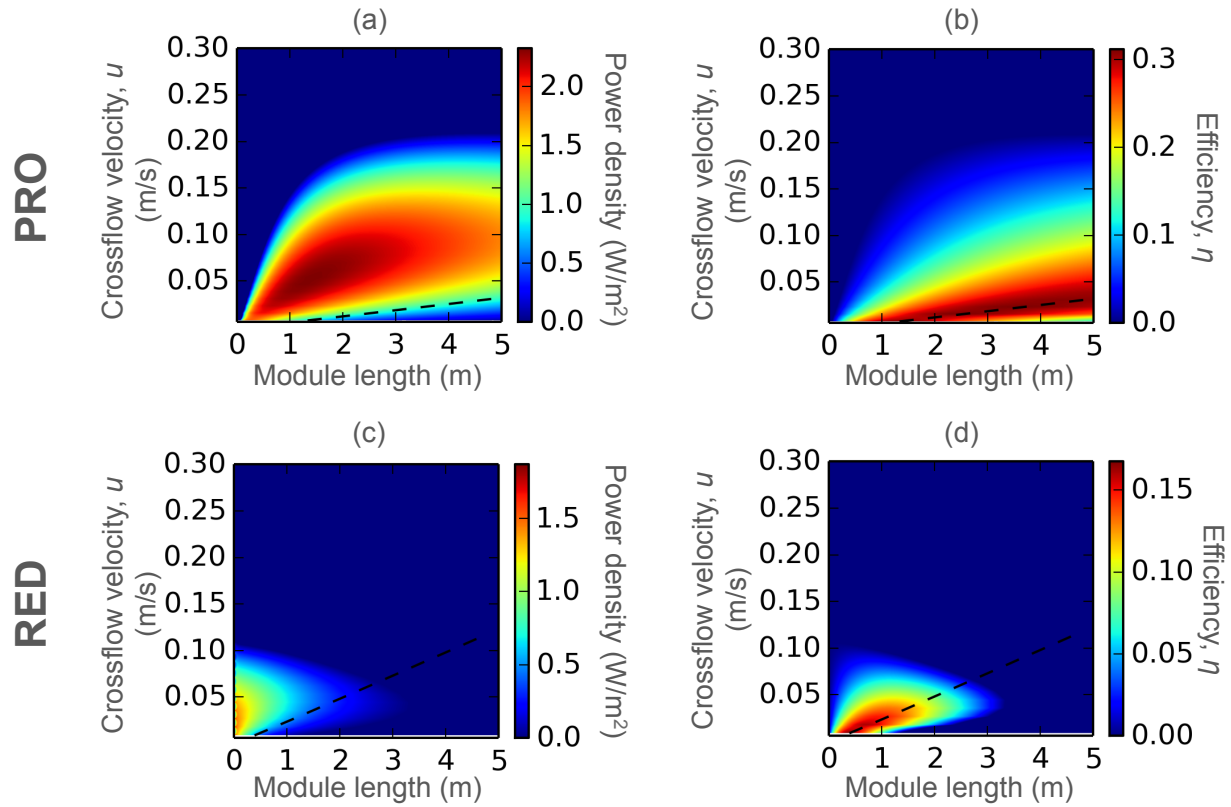

Figure 3.4 Change in power density and efficiency for PRO (a,b) and RED (c,d), with variation in crossflow velocity and module length. The dashed black line on all plots corresponds to the module length at which mixing approaches equilibrium (i.e. $J_w \approx 0$ for PRO and $J_{coul} \approx 0$ for RED) for the given set of operational conditions. All calculations for PRO and RED were made with $f = 2$.

narrower region of preferred operation (**Figure 3.4**c-d). The smaller channel height in RED increases the impacts of hydraulic pressure losses on the average power density and efficiency.

3.3.4 Change in dilution ratio

Varying the dilution ratio at a constant total crossflow velocity (u = 0.04 m/s) indicates that increasing the dilution ratio results in higher efficiency for RED but lower efficiency for PRO (**Figure 3.5**). It is also clear from the data that, for PRO, operating near a dilution ratio of unity leads to maximum system length (i.e. more membrane is necessary to achieve thermodynamic

equilibrium). For RED, membrane area is maximized at $2 < d_r < 3$. The results incorporate the thermodynamic effect of changing mixing volumes as well as external mass transfer and hydraulic pressure loss effects.

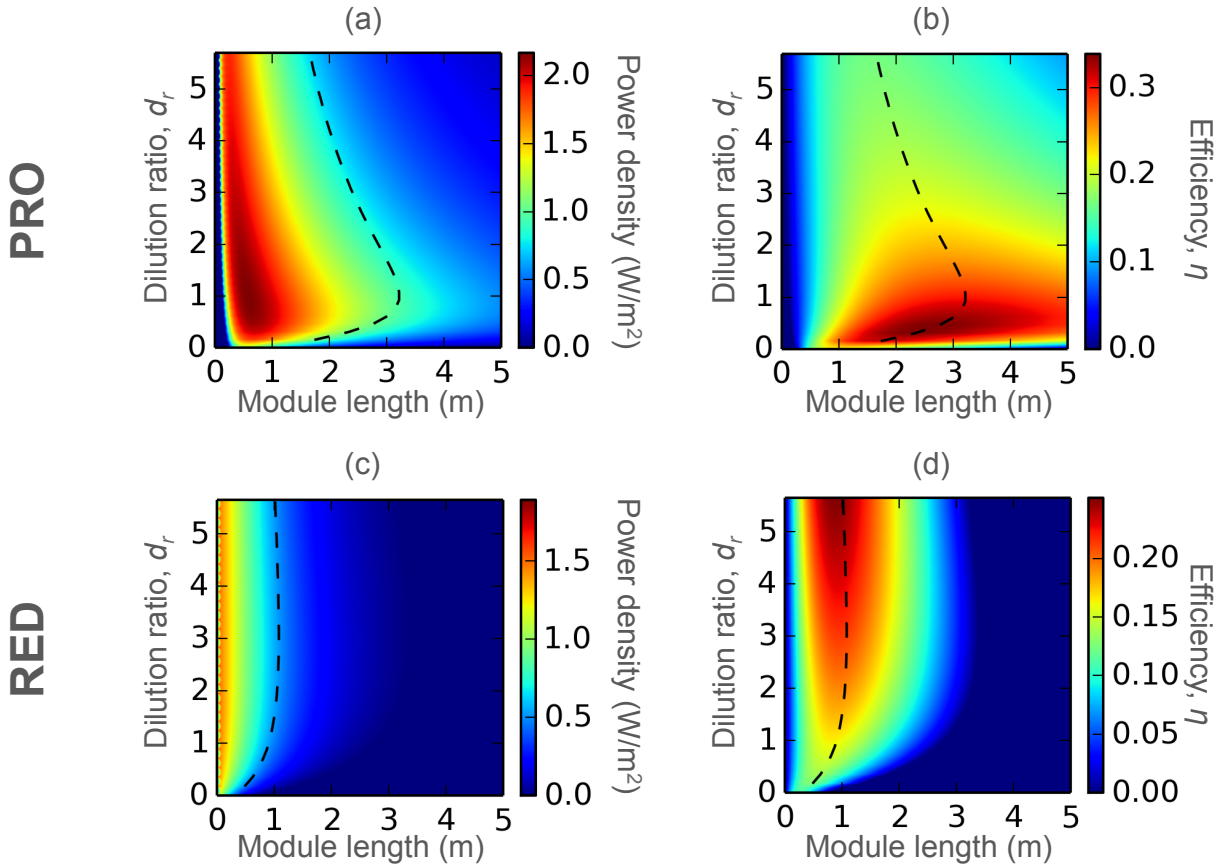

Figure 3.5 Change in power density and efficiency for PRO (a,b) and RED (c,d), with variation in dilution ratio and module length. The dashed black line on all plots corresponds to the module length at which mixing approaches equilibrium (i.e. $J_w \approx 0$ for PRO and $J_{coul} \approx 0$ for RED) for the given set of operational conditions. Calculations made with a total crossflow velocity u = 0.04 m/s, with dilution ratio variation achieved by taking different fractions of the total velocity. All calculations for PRO and RED were made with $f = 2$.

3.3.5 Maximum values

As has been demonstrated above, the process model can be used to determine how important performance metrics change under different operating conditions. From **Figure 3.3** – **Figure 3.5**, it is clear that the values for power density and efficiency change with dilution ratio, load factor, and crossflow velocity. However, in the preceding set of calculations, each of these operating parameters was varied individually with respect to module length. It is useful to identify how the maximum values for three performance metrics – power (P_{net}), power density (P_d), and efficiency (η) – change as operating conditions are changed simultaneously rather than one at a time. Here, dilution ratio and load factor have been chosen as the variable operating conditions. In order to conduct the analysis, the maximum value for each performance metric was evaluated for different system lengths, and the largest value was plotted against the relevant load factor. Note that, as the load factor necessarily impacts the driving force and equilibrium in each case, module length is not constant across all scenarios, and is rather a model output, giving a value of the system size at which a maximum is achieved for either the total power, power density or efficiency. **Figure 3.6** shows how changes in load factor impact the maximum energy efficiency, power, and power density for several dilution ratios (d_r = 0.25,1,4) when all process losses are incorporated. Dilution ratio variation has been achieved using the method described earlier.

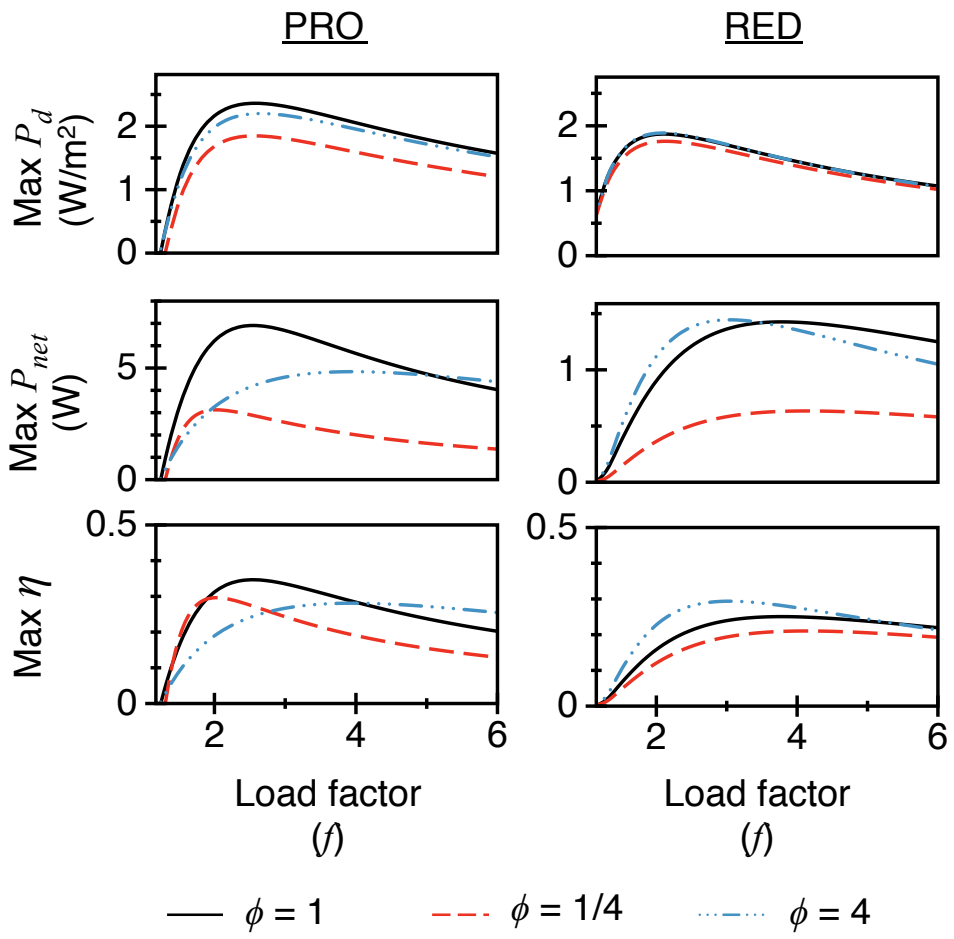

Figure 3.6 Change in maximum power density (P_d), maximum power (P_{net}), and maximum efficiency (η) for PRO (left column) and RED (right column) as the load factor (f) is varied at different dilution ratios.

While all dilution ratios show roughly similar maximum power density values, the power output and efficiency vary significantly with dilution ratio. Thus, reporting a maximum power density value alone is an incomplete measure for judging the performance of an SGP process since these maximum power densities may correlate with different system size. Furthermore, the data shows that higher energy efficiency does not necessarily correspond to higher overall power output. For example, in RED, operating at d_r = 4 is more efficient than operating at d_r = 1, yet both scenarios produce roughly the same overall power output. Similar behaviour can be observed for PRO. In an ideal case, the efficiency will vary only by changing the ratio of the feed

flow rates and not the magnitude of the flow rates. Accounting for losses, however, introduces some impact of the actual flow rate magnitude on energy efficiency due to viscous losses and mass transfer limitations (external concentration polarization). In either case, the power produced is of course proportional to the mixed volumes. For example, if 10 m^3 of river water were mixed with 40 m^3 of seawater, one would still expect greater overall power output than from mixing 0.10 m^3 of river water with 0.10 m^3 of seawater, despite the higher overall efficiency in the latter case.

Over the range of flow rates modeled, RED displays higher maximum efficiency with increasing dilution ratio. A larger relative dilute feed flow rate maintains low concentrations and thus ensures a more sustained potential difference across the membrane. PRO, on the other hand, does not exhibit a clear trend over the dilution ratios modeled. In theory, a relatively larger concentrated solution flow rate results in greater sustained osmotic pressure difference between the two solutions, since each molecule of water crossing the membrane has relatively lessened dilutive effect. However, in a non-ideal system, increasing the concentrated feed flow rate results in greater viscous dissipation in the feed channel, decreasing the overall energy efficiency.

Recall that, in an ideal case, power density is maximized at $f = 2$. As already established earlier (see **Figure 3.3**), power density and efficiency are not maximized at this value. However, while maximum power density peaks at the same load factor for all modeled dilution ratios, this is not the case for maximum efficiency or maximum power (**Figure 3.6**). Varying the dilution ratio necessarily changes the preferred load factor. These effects are shown to be of great importance and so must be considered when determining an optimum operating regime.

As noted earlier, maximum membrane area per "cell" (i.e. the system length necessary to achieve $J_w \approx 0$ or $J_{coul} \approx 0$, multiplied by unit width and a factor of two to account for two membranes), necessarily changes with varying inlet conditions. To determine the maximum membrane area, one cannot simply divide the total maximum power by the maximum power density shown in **Figure 3.6**, since each of these metrics is maximized at a different system size. Still, it is worthwhile to identify how maximum area changes with dilution ratio and we can

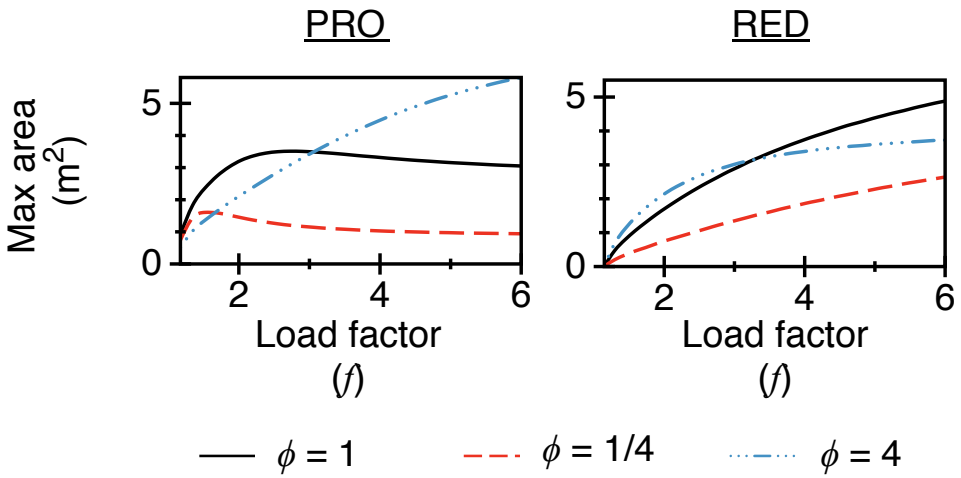

Figure 3.7 Change in maximum membrane area for one "cell" (i.e. the system length necessary to achieve $J_w \approx 0$ or $J_{coul} \approx 0$, multiplied by unit width and a factor of two to account for two membranes), for PRO (left column) and RED (right column) as the load factor (f) is varied at different dilution ratios.

extract this value from the process model. From **Figure 3.7**, it is clear that maximum membrane area scales differently with varying dilution ratio for PRO and RED. As noted earlier, these results are per "cell," at the same cross flow velocities for PRO and RED, and not at equal flow rate. For RED, membrane area appears to increase with increasing load factor, irrespective of the actual dilution ratio. On the other hand, for PRO, maximum membrane area appears to peak at lower load factors for some dilution ratios. This behavior is a consequence of the way the driving

force ($\Delta\pi$ or ΔV_{mem}) and retarding force (Δp or ΔV_{load}) impact the flux equations differently for each process.

3.3.6 Cost considerations

Ultimately, the cost to produce a kilowatt-hour of energy and the installed cost (per kW) are the most important metrics in evaluating energy production, and for designing full-scale membrane area requirements (here represented by module length). It is also the most useful basis of comparison between SGP processes and, ultimately, other forms of electricity generation. As stated earlier, it would not be economically viable to seek complete mixing (i.e., equilibrium) due to the relatively low productivity of downstream membranes. The most cost-effective system lengths will lie somewhere between the maximum power density and efficiency.

For a SGP process, total membrane module cost will scale with membrane area. However, assuming constant crossflow velocity, there is a tradeoff between the cost associated with pump flow rate requirement (higher for cells in parallel) and pump pressure requirement (higher for cells in series due to higher pressure drop). With the input of cost correlations for each of the system components (pumps, membrane modules, HER device, etc.), it is possible to use the process model to optimize the cost relative to the system power output. That is, one can determine the location of maximum cost-effectiveness (i.e. the effective length or number of cells in series) depending on the relative capital costs of different plant components. Operating costs, which may scale differently than capital costs, can also be considered in the overall cost optimization. For example, pump capital cost could outweigh membrane capital cost (i.e. in very short modules), but the operating cost associated with membrane cleaning could be more

significant than pump maintenance. Of course, the accuracy of such an analysis will depend on the quality of the cost correlations used for the various plant components.

While it is possible to use seawater RO empirical relationships to estimate costs for PRO and RED, the classical models do not appear to realistically predict optimized full-scale performance. Loeb used a different method for his analyses of PRO feasibility [24, 26]. It must be acknowledged, however, that Loeb did not apply a full-scale process model to determine how power density changes with system length, and he extrapolated the cost for PRO based on the cost per cubic meter of permeate volume produced by RO, whereas our work herein suggests that method may be unsubstantiated. Future work to determine PRO or RED cost should rely on appropriate full-scale process model results (such as those presented here) as well as updated empirical correlations for plant component capital cost, operating cost, construction cost, and other contributing costs.

3.4 Conclusions

A new process model has been formulated for PRO enabling simulation of power density and process efficiency for full-scale system designs. Here, the modeled scenario corresponds to ocean water-river water mixing, whereas applications with significantly different salinity gradients may require different operating conditions to optimize performance. The results provided herein demonstrates the following.

1) HER device efficiency can significantly impact the power density and energy efficiency profiles for PRO. An important future research area is the refinement and improvement of HER devices for the operating pressures likely to be encountered in PRO.

2) The impact of cross-flow velocity is clear. In particular, PRO studies commonly employ velocities that (according the results of this study) are likely to consume significant power output at scale.
3) Load pressures and voltages typically identified as the preferred operating regimes for PRO and RED are shown here to be non-ideal. Therefore, full-scale implementation of either process should not rely on predictions from simpler models.
4) Highest energy efficiency does not necessarily occur at thermodynamic equilibrium for both processes due to viscous dissipation. Furthermore, energy efficiency appears to be maximum at lower dilution ratios for PRO and higher dilution ratios for RED. Depending on the relative availability of the dilute or concentrated feed, this could imply a preference for a particular process.
5) Since membrane area varies significantly with dilution ratio, maximum power density is an incomplete metric for comparing a process with different operating conditions.

The data presented here demonstrates that the power densities achievable from PRO and RED are still relatively low, particularly when compared to reported lab-scale measurements. Ultimately, the most direct method to increase power production (but not necessarily efficiency) is to increase the concentrated feed salinity. The increased salinity will lead to larger water and Coulombic fluxes for PRO and RED, respectively, allowing for higher total power output. Still, operation at higher salinity presents a new set of challenges, such as corrosion, membrane compaction at higher pressures, and availability of hyper-saline feed waters. Ultimately, a reduction in the cost of energy production for both PRO and RED will largely depend on a mix of component cost decrease (specifically membrane cost reduction), optimal engineering design, and adequate governmental policy support.

Acknowledgements

We are grateful for financial support for this research provided by the Clean Energy for Green Industry (CGI) NSF IGERT at UCLA. G.Z.R was supported by a Marie-Curie IOF grant under the FP7 program of the European Research Council.

Nomenclature

A	Water permeability coefficient, m Pa^{-1} s^{-1}
B	Salt permeability coefficient, m s^{-1}
b	Module width, m
c	Concentration, mol m^{-3}
c_{eq}	Equilibrium concentration, mol m^{-3}
D	Solute diffusion coefficient in water, m^2 s^{-1}
d_h	Hydraulic diameter, m
d_r	Dilution ratio
D_m	Solute diffusion coefficient in membrane, m^2 s^{-1}
ΔE	Open circuit voltage, V
F	Faraday constant, C mol^{-1}
f	Load factor
h	Channel height, m
J_{cit}	Co-ion flux, mol m^{-2} s^{-1}
J_{coul}	Coulombic flux, mol m^{-2} s^{-1}
J_s	Salt flux, mol m^{-2} s^{-1}
J_w	Water flux, m s^{-1}
k	External mass transfer coefficient, m s^{-1}
L	Module length, m
p	Pressure, Pa

P_d	Power density, W m^{-2}
P_{ht}	Power generated through hydroturbine, W
P_{load}	Power generated through external load, W
P_{net}	Net power, W
P_p	Pump demand, W
P_{rev}	Power from reversible mixing, W
q	Volumetric flow rate, m^3 s
R	Universal gas constant, J mol^{-1} K^{-1}
Re	Reynolds number
r	Resistance, Ohm m^2
r_{mem}	Membrane resistance, Ohm m^2
r_{stack}	Stack resistance, Ohm m^2
S	Structure parameter, m
Sc	Schmidt number
Sh	Sherwood number
T	Absolute temperature, K
u	Crossflow velocity, m s^{-1}
ΔV_{mem}	Voltage drop across membrane, V
ΔV_{load}	Voltage drop across external load, V
x	Distance, m

Greek letters

α	Permselectivity
δ_{mem}	Membrane thickness, m
η	Efficiency
η_{her}	HER-device efficiency
η_{ht}	Hydroturbine efficiency
η_p	Pump efficiency
λ	Friction factor

$\Delta\pi$	Osmotic pressure difference, Pa
ρ	Solution density, kg m^{-3}
ϕ	Osmotic coefficient
ω_n	Friction factor fitting parameter

Subscripts

b	Bulk
c	Concentrated
d	Dilute
i	Inlet
L	Outlet
m	Membrane interface

3.5 References

[1] G.Z. Ramon, B.J. Feinberg, E.M.V. Hoek, Membrane-based production of salinity-gradient power, Energy & Environmental Science, 4 (2011) 4423-4434.

[2] B.E. Logan, M. Elimelech, Membrane-based processes for sustainable power generation using water, Nature, 488 (2012) 313-319.

[3] J.W. Post, J. Veerman, H.V.M. Hamelers, G.J.W. Euverink, S.J. Metz, K. Nymeijer, C.J.N. Buisman, Salinity-gradient power: Evaluation of pressure-retarded osmosis and reverse electrodialysis, Journal of Membrane Science, 288 (2007) 218-230.

[4] J.W. Post, H.V.M. Hamelers, C.J.N. Buisman, Energy recovery from controlled mixing salt and fresh water with a reverse electrodialysis system, Environmental Science & Technology, 42 (2008) 5785-5790.

[5] A. Achilli, T.Y. Cath, A.E. Childress, Power generation with pressure retarded osmosis: An experimental and theoretical investigation, Journal of Membrane Science, 343 (2009) 42-52.

[6] P. Dlugolecki, A. Gambier, K. Nijmeijer, M. Wessling, Practical Potential of Reverse Electrodialysis As Process for Sustainable Energy Generation, Environmental Science & Technology, 43 (2009) 6888-6894.

[7] N.Y. Yip, M. Elimelech, Thermodynamic and Energy Efficiency Analysis of Power Generation from Natural Salinity Gradients by Pressure Retarded Osmosis, Environmental Science & Technology, 46 (2012) 5230-5239.

[8] B.J. Feinberg, G.Z. Ramon, E.M. Hoek, Thermodynamic Analysis of Osmotic Energy Recovery at a Reverse Osmosis Desalination Plant, Environmental Science & Technology, 47 (2013) 2982-2989.

[9] J. Veerman, M. Saakes, S.J. Metz, G.J. Harmsen, Reverse electrodialysis: A validated process model for design and optimization, Chemical Engineering Journal, 166 (2011) 256-268.

[10] D.A. Vermaas, J. Veerman, N.Y. Yip, M. Elimelech, M. Saakes, K. Nijmeijer, High Efficiency in Energy Generation from Salinity Gradients with Reverse Electrodialysis, ACS Sustainable Chemistry & Engineering, 1 (2013) 1295-1302.

[11] S. Kim, E. Hoek, Modeling concentration polarization in reverse osmosis processes, Desalination, 186 (2005) 111-128.

[12] L. Song, S. Hong, J. Hu, S. Ong, W. Ng, Simulations of full-scale reverse osmosis membrane process, Journal of environmental engineering, 128 (2002) 960-966.

[13] L. Song, S. Yu, Concentration polarization in cross‐flow reverse osmosis, AIChE journal, 45 (1999) 921-928.

[14] W. Zhou, L. Song, T.K. Guan, A numerical study on concentration polarization and system performance of spiral wound RO membrane modules, Journal of membrane science, 271 (2006) 38-46.

[15] E.M.V. Hoek, J. Allred, T. Knoell, B.-H. Jeong, Modeling the effects of fouling on full-scale reverse osmosis processes, Journal of Membrane Science, 314 (2008) 33-49.

[16] G. Guillen, E.M.V. Hoek, Modeling the impacts of feed spacer geometry on reverse osmosis and nanofiltration processes, Chemical Engineering Journal, 149 (2009) 221-231.

[17] W.J. Hamer, Y.C. Wu, Osmotic Coefficients and Mean Activity Coefficients of Uni‐univalent Electrolytes in Water at 25° C, Journal of Physical and Chemical Reference Data, 1 (1972) 1047-1100.

[18] K.S. Pitzer, J.C. Peiper, R. Busey, Thermodynamic properties of aqueous sodium chloride solutions, Journal of Physical and Chemical Reference Data, 13 (1984) 1-102.

[19] N.Y. Yip, A. Tiraferri, W.A. Phillip, J.D. Schiffman, L.A. Hoover, Y.C. Kim, M. Elimelech, Thin-Film Composite Pressure Retarded Osmosis Membranes for Sustainable Power Generation from Salinity Gradients, Environmental Science & Technology, 45 (2011) 4360-4369.

[20] J. Veerman, R.M. de Jong, M. Saakes, S.J. Metz, G.J. Harmsen, Reverse electrodialysis: Comparison of six commercial membrane pairs on the thermodynamic efficiency and power density, Journal of Membrane Science, 343 (2009) 7-15.

[21] J.N. Weinstein, F.B. Leitz, Electric power from differences in salinity: the dialytic battery, Science, 191 (1976) 557-559.

[22] Y.C. Kim, Y. Kim, D. Oh, K.H. Lee, Experimental Investigation of a Spiral-Wound Pressure-Retarded Osmosis Membrane Module for Osmotic Power Generation, Environmental Science & Technology, 47 (2013) 2966-2973.

[23] A. Tiraferri, N. Yin Yip, A.P. Straub, S. Romero-Vargas Castrillon, M. Elimelech, A Method for the Simultaneous Determination of Transport and Structural Parameters of Forward Osmosis Membranes, Journal of Membrane Science, 444 (2013) 523–538.

[24] S. Loeb, Large-scale power production by pressure-retarded osmosis, using river water and sea water passing through spiral modules, Desalination, 143 (2002) 115-122.

[25] T.Y. Cath, M. Elimelech, J.R. McCutcheon, R.L. McGinnis, A. Achilli, D. Anastasio, A.R. Brady, A.E. Childress, I.V. Farr, N.T. Hancock, Standard methodology for evaluating membrane performance in osmotically driven membrane processes, Desalination, 312 (2012) 31–38.

[26] S. Loeb, One hundred and thirty benign and renewable megawatts from Great Salt Lake? The possibilities of hydroelectric power by pressure-retarded osmosis, Desalination, 141 (2001) 85-91.

4 TOWARD IMPROVING PRESSURE RETARDED OSMOSIS EFFICIENCY USING A STAGED APPROACH

4.1 Introduction

Salinity gradient power (SGP) technology could provide continuous, renewable power through the mixing of feeds with different salinity. Recently, our group developed full-scale process models for the two most popular SGP technologies, pressure retarded osmosis (PRO) and reverse electrodialysis (RED) [1]. The developed models are more comprehensive than simpler mixing models and likely reflect a truer measure of achievable power densities and efficiencies. The power densities reported by the process model highlight the need for innovative module and flow design in order to improve the feasibility of SGP. While there has been significant research into RED module design [2-4], there has been less focus on optimizing PRO process configurations.

A PRO system can be designed, at the extremes, with many short modules in parallel or a small number of longer modules. Given the same total membrane area in both cases (and the same flow channel crossflow velocity), the parallel configuration will necessarily require more total flow into the system. As a result of this higher flow rate, pump, pretreatment, and other ancillary costs will be greater. This impact is compounded by the fact that many feed streams are not available in infinite supply (diluted wastewater, brine, etc.). It may, therefore, be prudent to operate at higher efficiency than otherwise assumed given these considerations. Thus, maximizing efficiency is a valid and important goal of any research work into PRO.

From previous research [5] we know that, in an ideal system where equal volumes of dilute and concentrated flow are mixed, efficiency and power density are both maximized at $\Delta p = \Delta\pi/2$, where Δp is the applied pressure difference and $\Delta\pi$ is the osmotic pressure difference between the concentrated and dilute feeds. In a real system, there is some deviation from this ideal condition [1]. An important point, nevertheless, is that as mixing proceeds in PRO the concentration (and therefore $\Delta\pi$) changes. At points downstream from the module inlet Δp is

now mismatched from the local ideal operating condition of $\Delta\pi/2$. The main goal of this study is to identify an operational configuration wherein this effect can be managed. This so called *staged PRO configuration* is depicted in Figure 1 and is designed to improve process efficiency (and power density) relative to the standard configuration by re-setting the applied pressure at the inlet of different flow segments. Note that in the modeled scenarios, membrane area is kept constant between the standard and staged configurations, and an increase in efficiency necessarily results in an increase in power density. Therefore, only efficiency changes are shown but power density changes can be assumed by the reader.

Many potential configurations can be envisaged using this intermodule arrangement. Here, the flow fed into the concentrated feed channel of each downstream segment is the same as at the entrance to the system. In practice, this means that excess (permeate) flow after each segment is combined and fed directly to a single excess flow hydroturbine. Note that the configuration of the turbines as suggested in **Figure 4.1** is not a commonly applied design approach for hydroturbines in power generation. Often, hydroturbines are operated in such a way as to recover as much energy from the flow as possible. Therefore, the full pressure of the flow is transferred to kinetic energy in the turbine blades (minus some unavoidable losses), and little pressure is retained in the flow relative to the inlet pressure. The hydroturbine mode suggested here instead implies only partial recovery of the pressure. Kinetic energy of the hydroturbine blades should be managed by increasing rotational resistance of the hydroturbine. Obviously, research into the feasibility of such a design and the most efficient operational method for employing such a configuration must still be conducted. For the purposes of this study, the same operational efficiency was taken for the excess flow and intermodule hydroturbines.

The aim of the work discussed herein is to identify how a staged flow configuration may improve PRO efficiency. To accomplish this task, the process model developed in an earlier paper was modified to suit the configuration of interest. For the purposes of this study, membrane properties (Oasys TFC membrane) and module geometry were taken from **Chapter 3**.

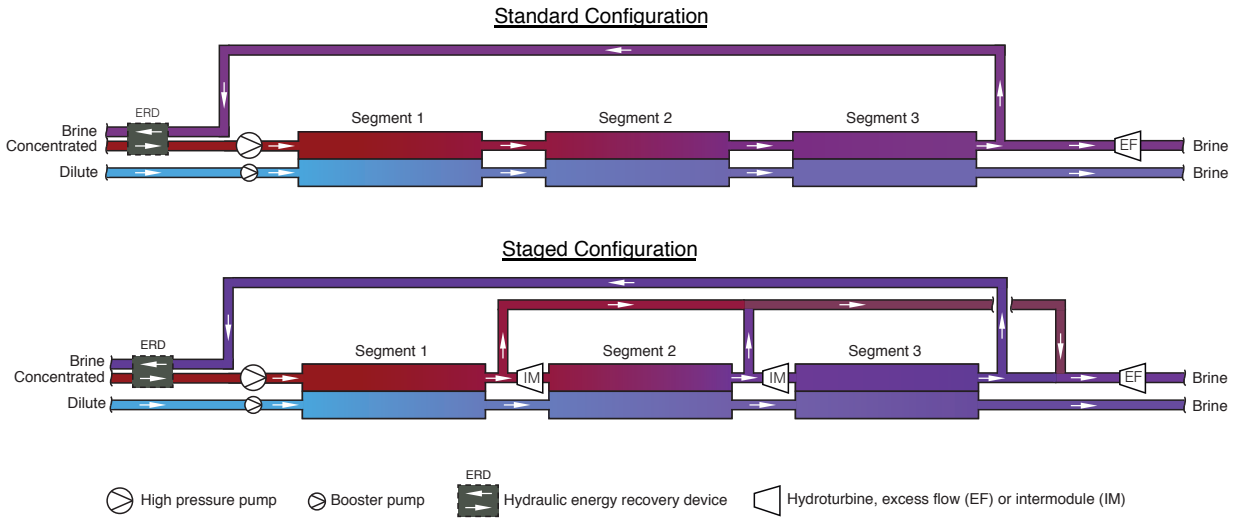

Figure 4.1. Graphical representation of a standard configuration (top) and a staged configuration (bottom) for PRO. Note the staged configuration has intermodule hydroturbines placed between each segment, which modulate the applied pressure at the inlet to the following segment. Excess flow (relative to the initial flow rate) from the outlet of each segment is combined and fed through a final excess flow hydroturbine.

4.2 Model Formulation

The process model applied in this study was previously developed by the co-authors in order to evaluate scale-up characteristics of salinity gradient power [1]. Briefly, a one-dimensional process model was applied, accounting for longitudinal changes in concentration, velocity, and pressure. Algebraic correlations are used to correlate bulk concentrations to the membrane interface concentrations necessary for calculating water flux. The system of differential and

algebraic equations is then solved using an appropriate solver (APMonitor) [6]. Since we are interested in how process performance scales over a large area, this approach is preferable to more computationally exhaustive 2D and 3D computational fluid dynamics (CFD) techniques. Note that this type of approach has been successfully applied in the past studies, with good experimental agreement. Mass and momentum balances applied to each channel yield the system of governing ordinary differential equations for transport in each process. **Eq.** 4.1, 4.2, and 4.3 describe changes in crossflow velocity *u(x)*, solute concentration *c(x)*, and pressure *p(x)*, with position *x* (module length) in the dilute and concentrated channels, *viz*.

$$\frac{du}{dx} = \pm\frac{2J_w}{h} \tag{4.1}$$

$$\frac{d(uc)}{dx} = \pm\frac{2J_s}{h} \tag{4.2}$$

$$\frac{dp}{dx} = -\frac{\lambda\rho u^2}{2d_h} \tag{4.3}$$

Friction factor coefficients used in determining the hydraulic losses within each channel were calculated using correlations described in **Appendix A**. Water flux in PRO is a function of many parameters, including bulk solute concentrations, salt diffusivity *D*, external mass transfer coefficient k_c, universal gas constant *R*, temperature *T*, and membrane permeability to water *A*, and salt *B*. Details of the calculation of the water flux in PRO, assuming non-ideality in the osmotic pressure calculation, as well as the salt flux (or "salt leakage"), which is assumed to be purely diffusive in PRO, is also discussed in **Chapter 3**. The total power in PRO can determined by subtracting the contribution of the pumping energy demand for the dilute and concentrated feeds from the power generated by the hydroturbine, i.e. $P_{net} = P_{ht} - P_{p,}$ where

$$P_{ht} = \eta_{ht} b h_c p_{c,L} \int_0^L J_w dx \tag{4.4}$$

and

$$P_p = \frac{q_{c,i}}{\eta_p}(p_{c,i} - \eta_{her} p_{c,L}) + \frac{q_{d,i}}{\eta_p}(p_{d,i} - p_{d,L}), \tag{4.5}$$

where η_{ht}, η_p and η_{her} denote the efficiencies of the hydroturbine, pump and, hydraulic energy recovery device, respectively, and b is the width (hereafter taken as unity). The first term on the right hand side of **Eq.** 4.5 is the power necessary to pump the concentrated feed, where the energy consumption is reduced due to the contribution of the hydraulic energy recovery device (HER) device. Here we define the total process efficiency as the total generated power (or work) divided by the theoretical power (or work) available with completely reversible mixing

$$\eta = \frac{P_{net}}{P_{rev}}. \tag{4.6}$$

Note that this value corresponds to the fraction of the reversible work, and not the available work, that is recovered through mixing [7].

4.3 Results and Discussion

Figure 4.2 depicts the water flux, pressure and concentration variation along system length for standard and staged PRO configurations. For the analysis conducted in **Figure 4.2**, we assume three segments of equal length (0.5 m each) for both cases. Note that for the standard configuration this arrangement is considered to be functionally the same as a single, 1.5 m long segment, and the length of each segment has been chosen in order to demonstrate most clearly

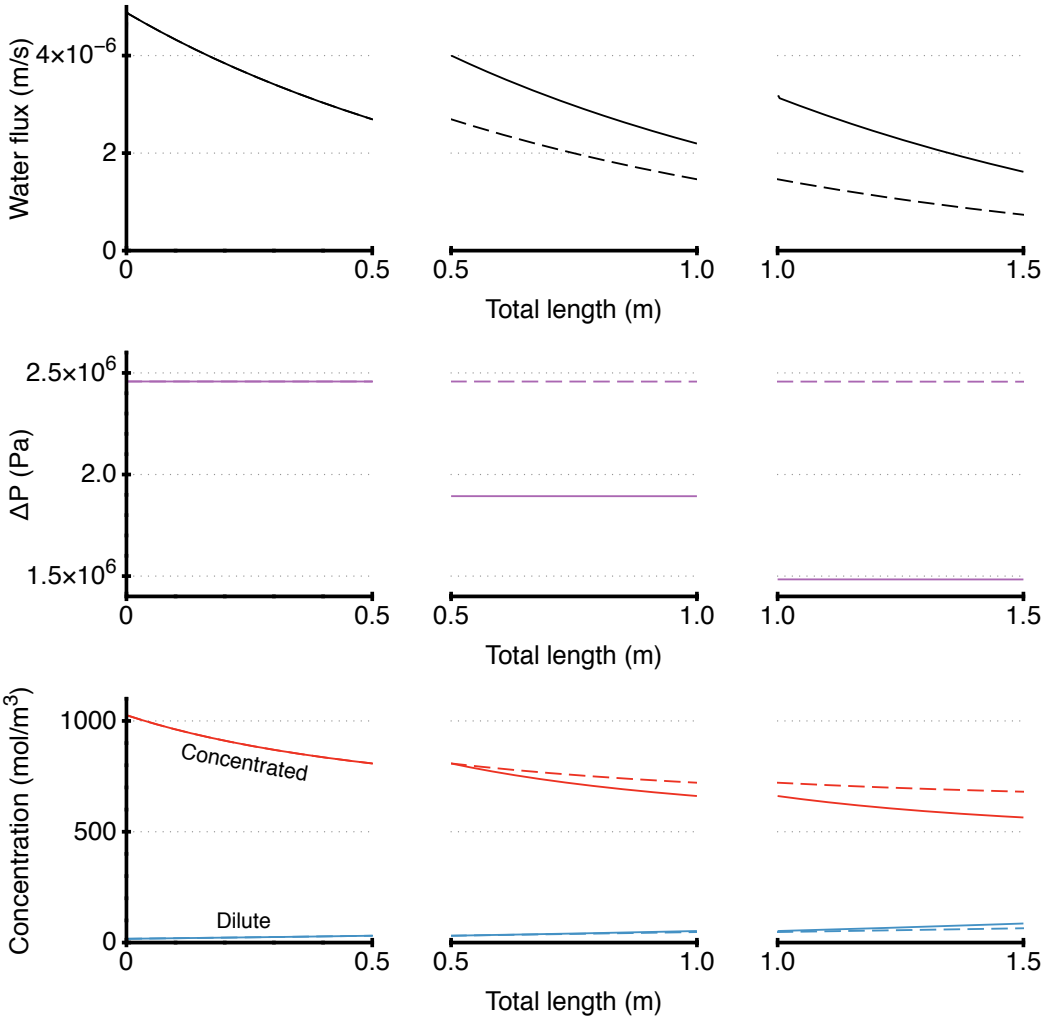

Figure 4.2 The change in water flux (top), pressure difference (middle) , and concentration (bottom) with total system length for the standard (dashed line) and staged (solid line) configurations. This output corresponds to the scenario depicted in Fig.1, with pressure modulated at the entrance to each segment for the staged configuration. Note how water flux increases dramatically at the entrance to downstream segments (0.5 m and 1.0 m). The modelled scenario is for brine (1026 mol/m^3) and river water (17 mol/m^3) mixing.

the differences between the staged and standard configurations. The length of each segment is not meant to correspond to a specific module length currently available on the commercial market. It is clear from **Figure 4.2** that, as expected, water flux for the standard configuration at

is highest at the module inlet where the thermodynamic driving force is greatest between the concentrated and dilute feeds. For the staged configuration, we note that the water flux is increased versus the standard configuration at the inlet to Segments 2 and 3.

The increased flux in the staged configuration is a direct consequence of the diminished pressure difference between the concentrated and dilute feeds. For the standard configuration, the pressure difference between the concentrated and dilute feeds remains relatively constant along the system length due to the relatively small pressure change from viscous dissipation. With respect to concentration change using the standard configuration, most of the concentration change occurs over the first third of the total system length due to the lower overall productivity of later segments. However, with staging the outlet concentration difference between the two feeds is diminished versus the standard configuration case, indicating increased overall mixing.

Figure 4.3 shows the change in efficiency with the number of PRO stages for two different crossflow velocities and three mixing scenarios (seawater-river water, brine-river water, brine-seawater). The results are also depicted for three total system lengths (1m, 2m, and 3m) in order to evaluate the impact of staging with increased overall mixing. Staged PRO appears to offer significantly improved efficiency over the standard configuration for brine-river water and seawater-river water mixing at lower crossflow velocities, with efficiency increases from 31% to 44% and 34% to 50%, respectively, versus the standard PRO configuration. It is also clear, however, that the bulk of the efficiency improvement is achieved using just a single additional hydroturbine. Thus, improved efficiency may be possible with only a marginal increase in capital cost.

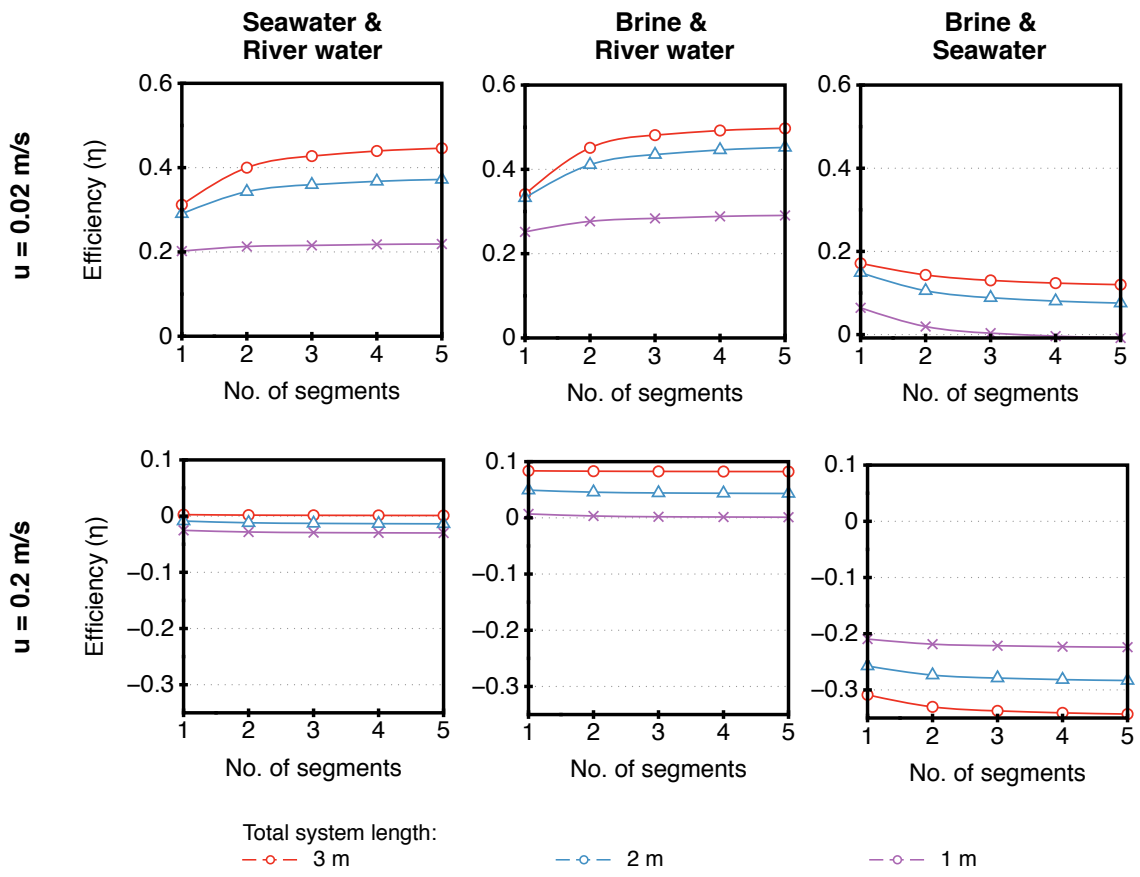

Figure 4.3 Change in PRO efficiency for three different mixing regimes and two crossflow velocities, The three colored lines on each subplot correspond to different total system length for staged PRO.

For other mixing scenarios, staged PRO does not appear to offer improved efficiency, and in some cases, staging actually results in decreased efficiency with increasing number of segments. Irrespective of crossflow velocity, brine-seawater mixing does not demonstrate an improvement in performance with segmentation. Since the initial thermodynamic driving force is lower in this case, decreasing the pressure difference between the concentrated and dilute feeds does not serve to radically improve the overall flux, particularly in light of the increased overall machine inefficiency from the additional hydroturbine. Similarly, the higher velocity case (u = 0.2 m/s) for all mixing scenarios results in either the same or decreasing efficiency with staging.

As the number of PRO stages increases, greater energy is lost in the higher velocity case than if a lower velocity is applied.

Finally, we must acknowledge the PRO process cost that will necessarily increase due to additional hydroturbine capital cost. However, if we take RO as an analogy, we know that pumps account for only around 7% of the total capital cost of the plant [8]. Furthermore, amortized capital cost itself accounts for just 56% of the total operating cost ($/m^3) of an RO plant (neglecting the contribution of electrical electricity demand, since PRO is net positive power). This further decreases the relative contribution of the pumps to the total cost. It is possible that hydroturbines will be valued at the same price as the pumps, however there is evidence to suggest hydroturbines may actually scale lower in price [4]. Additional hydroturbines, therefore, are not likely to shift the installed cost much, but may lead to significantly greater power generation. Ultimately, it seems prudent to invest in the staged configuration if the goal is to reduce the cost of electricity production ($/kWh).

4.4 Conclusion

In order to improve the overall efficiency of the PRO process, a novel process configuration has been suggested in this study. Using a comprehensive process model for PRO developed in a prior study, we have shown that the efficiency of PRO can be dramatically improved using a relatively simple modification to the standard configuration. However, in some cases the impact of staging actually resulted in efficiency decreases due to compounding machine inefficiency and low mixing potential. Ultimately, the rationale for introducing staging will depend on criteria pertaining to the specific site and mixing regime. In future work, the optimization of staging with

respect to segment length, crossflow velocity, turbine efficiency, and other operational parameters can be investigated.

4.5 References

[1] B.J. Feinberg, G.Z. Ramon, E.M. Hoek, Scale-up characteristics of membrane-based salinity-gradient power production, Journal of Membrane Science (Submitted) (2014).

[2] J. Veerman, M. Saakes, S. Metz, G. Harmsen, Reverse electrodialysis: performance of a stack with 50 cells on the mixing of sea and river water, Journal of Membrane Science, 327 (2009) 136-144.

[3] J. Veerman, M. Saakes, S. Metz, G. Harmsen, Reverse electrodialysis: A validated process model for design and optimization, Chemical Engineering Journal, 166 (2011) 256-268.

[4] J. Veerman, M. Saakes, S.J. Metz, G.J. Harmsen, Electrical power from sea and river water by reverse electrodialysis: a first step from the laboratory to a real power plant, Environmental science & technology, 44 (2010) 9207-9212.

[5] N.Y. Yip, M. Elimelech, Thermodynamic and Energy Efficiency Analysis of Power Generation from Natural Salinity Gradients by Pressure Retarded Osmosis, Environmental Science & Technology, 46 (2012) 5230-5239.

[6] J.N. Weinstein, F.B. Leitz, Electric power from differences in salinity: the dialytic battery, Science, 191 (1976) 557-559.

[7] B.J. Feinberg, G.Z. Ramon, E.M. Hoek, Thermodynamic Analysis of Osmotic Energy Recovery at a Reverse Osmosis Desalination Plant, Environmental Science & Technology, 47 (2013) 2982-2989.

[8] G.W.I. (GWI), Desalination Markets 2010, (2010).

5 COST ANALYSIS FOR PRESSURE RETARDED OSMOSIS

5.1 Introduction

In previous chapters, we highlighted the potential performance from standalone and hybrid salinity gradient power technologies. However, in order to access the feasibility of a process, and thus, the practical potential for full-scale deployment of the technology, cost data must be incorporated into the analysis. In order to assess the competitiveness of SGP against other power generation processes, the cost of energy generation (i.e. the dollar sum required to produce a given amount of energy) can be calculated using cost correlation equations. Ultimately, using the cost data, one can determine the ideal system size, which may be distinct from points of optimum power density or efficiency.

Numerous cost correlations appear in the literature, including those from a recently published paper on a hybrid PRO/RO process [1]. Using this method, pumps, hydroturbines, and pressure exchangers are priced based on the design flow rate and pressure required for each component. However, due to the age of the correlations present in the literature, it is important to also develop new empirical relationships based on more current costing data. Correlations for plant components were developed by contacting manufacturers, suppliers, and engineering firms.

In this chapter, literature correlations (ECs) and developed correlations (DCs) are applied in order to determine the cost of energy produced by PRO. The cost of individual plant components is profiled for different operational scenarios. Furthermore, the impact of future improvements in membrane performance on energy cost is evaluated.

5.2 Methodology

5.2.1 Determining capital cost

The total cost of a plant is the sum of the capital cost (CAP EX) and operation cost (OP EX) over the lifetime of the facility. PRO is likely to share some similar equipment such as high-pressure pumps and pre-treatment with RO. However, certain plant components, such as the membrane modules, may scale differently for PRO. Here, we have based our analysis on the capital cost calculations for a seawater reverse osmosis (RO) facility as presented in the literature, as well as newer correlations developed using more current data.

The total CAP EX (CC_{tot}) is defined by

$$CC_{tot} = CC_{pre} + CC_{pump} + CC_{her} + CC_{ht} + CC_{mem} + CC_{pv} + CC_{other} \tag{5.1}$$

where CC_{pre} is the pre-treatment and seawater intake cost, CC_{pump} is the high pressure pump capital cost, CC_{her} is the hydraulic energy recovery device cost, CC_{ht} is the hydroturbine cost, CC_{mem} is the membrane module cost, CC_{pv} is the pressure vessel cost, and CC_{other} is other indirect costs and construction costs. In order to calculate the plant pump capital cost (CC_{pump}), empirical relationships were used as cited in the literature [1, 2] or formulated from manufacturer or supplier pricing information. High-pressure pump cost, as defined by the LCs, is dependent on both the flow rate and the required fluid pressure. In order to meet the total flow and pressure demand, a combination of pumps from the three classes listed below may be required,

$$CC_{pump,LC} = \begin{cases} 393{,}000 + 10{,}710\,p & \text{for q} = 450\ \text{m}^3/\text{h} \\ 81(pq)^{0.96} & \text{for } 200\ \text{m}^3/\text{h} < \text{q} < 450\ \text{m}^3/\text{h} \\ 52(pq) & \text{for q} < 200\ \text{m}^3/\text{h} \end{cases} \tag{5.2}$$

where p is the applied pump pressure (in bars) and q is the flow rate under pressure (in m^3/h), and subscript LC denotes that the value applies only to the literature correlations. **Eq.** 5.2 is presented in 1995 dollars, and therefore must be corrected to 2013 values by multiplying by the inflation factor (1.53). The DCs, which were compiled based on total pump load (power demand) rather than specific pressure or flow rate requirements, are defined as

$$CC_{pump,DC} = \begin{cases} 0.4744P^2 + 606.76P + 663998 & \text{for } P > 550 \text{ kW} \\ -0.617P^2 + 1576.58P + 350323 & \text{for } 350 \text{ kW} < P < 550 \text{ kW} \\ -1.7084P^2 + 2546.4P + 36648 & \text{for } P < 350 \text{ kW} \end{cases} \quad (5.3)$$

where P is the product of the pump pressure and flow rate required. In determining the hydroturbine capital cost (CC_{ht}), it was not possible to find appropriate literature correlations since hydroturbines are not used in RO. Therefore, the empirical relationships used for the high-pressure pumps were also applied for the hydroturbines due to assumed construction similarity (i.e. $CC_{ht,DC} = CC_{pump,DC}$). It was possible, however, to procure information from suppliers for a DC for hydroturbine cost as follows

$$CC_{ht,DC} = 0.0009P^2 + 204.9P^2 + 127049 \quad (5.4)$$

where P is the load (i.e. the product of the pressure and flow rate passed through the hydroturbine). The LC cost of the hydraulic energy recovery device (HER, or ERD) is [1, 3],

$$CC_{her,LC} = 19802.4(q_{brine})^{0.58} \quad (5.5)$$

where q_{brine} is the flow passed through the hydraulic energy recovery device in m^3/h. **Eq.** 5.5 is presented in 2006 dollars, and therefore must be corrected to 2013 values by multiplying by the inflation factor (1.16). The DC cost is calculated at $CC_{her,DC} = 614q_{brine}$, and is based on the provided cost for an Energy Recovery PX-300 unit with a capacity of 55 m^3/h. The LC and DC membrane module cost is calculated through

$$CC_{mem} = m_{mem} \times (\text{area}) \times \left(\frac{\text{plant life}}{\text{membrane life}} \right) \tag{5.6}$$

which is a modified form of the equation appearing in the literature [1, 4], and where m_{mem} is the per area membrane cost ($/m^2). In the LC case, the literature assumes m_{mem} = \$13.05/m^2, however this value must be multiplied by 1.27 in order to account for inflation. For the DC case, membrane cost has been identified for two cases with different operating pressures. At pressures below 27.5 bar, we assume the use of brackish water RO membranes with m_{mem} = \$13.4/m^2, while at higher pressures seawater RO membranes are assumed to be necessary with m_{mem} = \$19.6/m^2. Here, we have assumed a plant life of 20 years and a membrane life of 5 years. An additional contribution of the pressure vessel, which can be calculated (as a function of the membrane area) by

$$CC_{pv} = m_{pv} \times (\text{area}) \tag{5.7}$$

Eq. 5.7 is modified from an equation appearing in the literature [1], where m_{pv} is the per membrane area pressure vessel cost and m_{pv} = \$6.06/m^2 for the LC. The LC value must be multiplied by 1.08 to account for inflation from 2008 figures. As in the case of the membrane module, the DC pressure vessel cost varies based on operating pressure with m_{pv} = \$6.00/m^2 below 27.5 bar and m_{pv} = \$8.50/m^2 at higher pressures. In accordance with the literature [2], the site development *indirect costs* (CC_{other}) have been assumed to be an additional 41% of the equipment capital costs. Note that, although pre-treatment and intake costs for the dilute and concentrated feed have been identified in the literature [1, 2, 5], the large variability and site specific nature of pre-treatment make it difficult to include here. For example, pre-treatment costs may be significantly lower in PRO than RO due to lower pressure operation. This may seem, in light of the inclusion of CC_{other} to be nonsensical. However, since indirect costs are

simply a multiple of total equipment cost, its inclusion simply shifts all values to higher cost but does not change the location of minimum cost.

5.2.2 Determining operating cost

Based on a cost-breakdown for reverse osmosis desalination [6], operating costs (parts and labor) were taken as 41% of the total annual cost (ATC). To arrive at this value, we have neglected the contribution of the pump electricity cost to the operating cost since these processes, unlike RO, are power generating rather than power consuming.

5.2.3 Calculating total cost of energy production

The total energy produced is simply the power produced by the facility multiplied by the lifetime of the plant. To account for downtime and maintenance of the plant, a utilization rate (r_u) of 0.90 has been assumed. The annual total cost (ATC) is calculated from the annual capital cost (ACC) and annual operating cost (AOC) [2]. The ACC is determined by multiplying the total capital cost by the capital charge (r_{cc}, assumed here to be 8%), i.e. $ACC = r_{cc} CC_{tot}$. The ATC is defined by [2]

$$ATC = ACC + AOC, \text{ where } AOC = 1.14\,ATC \tag{5.8}$$

The present value of the ATC is

$$PV_{ATC} = \frac{ATC\,[(i+1)^n - 1]}{i(i+1)^n} = 14.87\,ATC \tag{5.9}$$

where i is the discount rate (assumed here to be 3% per annum) and n is the plant lifetime. Therefore, the energy cost (in \$/kWh) equals

$$\text{Energy cost } (\$/kWh) = \frac{PV_{ATC}}{r_u \times P_{net} \times n} \tag{5.10}$$

where P_{net} is the net power. The energy cost serves as a useful basis of comparison for different operational scenarios. For example, in theory, different crossflow velocities may yield the same energy costs at different system lengths. This does not mean that the power produced in each case is the same. In one case, the system may produce 500 W and in another, 1000 W, but the energy cost in both cases may be \$0.30/kWh. If the number of cells is doubled in the 500 W case to match the power achieved in the 1000 W, the energy cost is still the same since both energy and cost are calculated in the same way.

All simulations assume the same number of "cells," with crossflow velocity (i.e. flow rate) and system length varying between the four cases. The number of cells (n = 12,400) corresponds to approximately 150,000 m^3/d brine discharge from a 300,000 m^3/day seawater RO plant, when operating the process at a cross flow velocity at 0.2 m/s. This arrangement assumes another 150,000 m^3/d of river water or treated wastewater is also available for mixing. Here, "feed" refers to the dilute solution and "draw" refers to the concentrated solution.

In all cases, the membrane properties are taken from the Oasys TFC membrane (as described in **Chapter 3**), unless otherwise noted. In order to simplify the analysis, membrane water permeability (A) and structure factor (S) are varied but membrane salt permeability (B) is held constant. Note that the energy cost values discussed in this chapter are the breakeven energy costs which correspond to a zero profit/loss scenario.

5.3 Results and Discussion

Figure 5.1 shows the change in the capital cost of individual plant components for the literature-based empirical correlations (LCs) as well as the developed correlations (DCs) from this study, based on two different system lengths (2 m and 5 m) and at two different crossflow velocities (a) 0.02 m/s and (b) 0.2 m/s. From comparing (a) and (b), it is clear that a higher crossflow velocity across the membrane modules results in significant changes to the cost of some plant components. Pump, hydroturbine, and energy recovery device (ERD) cost change dramatically with operation at a higher crossflow velocity. Since higher velocity corresponds to higher flow rate, more and larger pumps, hydroturbines, and ERDs are necessary to accommodate the increased load. Despite the higher overall cost for the higher velocity case, the cost per kilowatt hour may scale differently than the change in capital cost due to the differences in power generated using different crossflow velocities. Note also that membrane module and pressure vessel cost change little with crossflow velocity. This is because a system of a certain length will have a fixed cost for these components, regardless of the hydraulics within the system itself. At a given crossflow velocity, longer systems have higher membrane cost and pressure vessel cost, but very similar pump cost and ERD cost to the lower velocity case. In practice, there seems to be little impact of channel viscous dissipation in increasing the pump size (and cost) requirement.

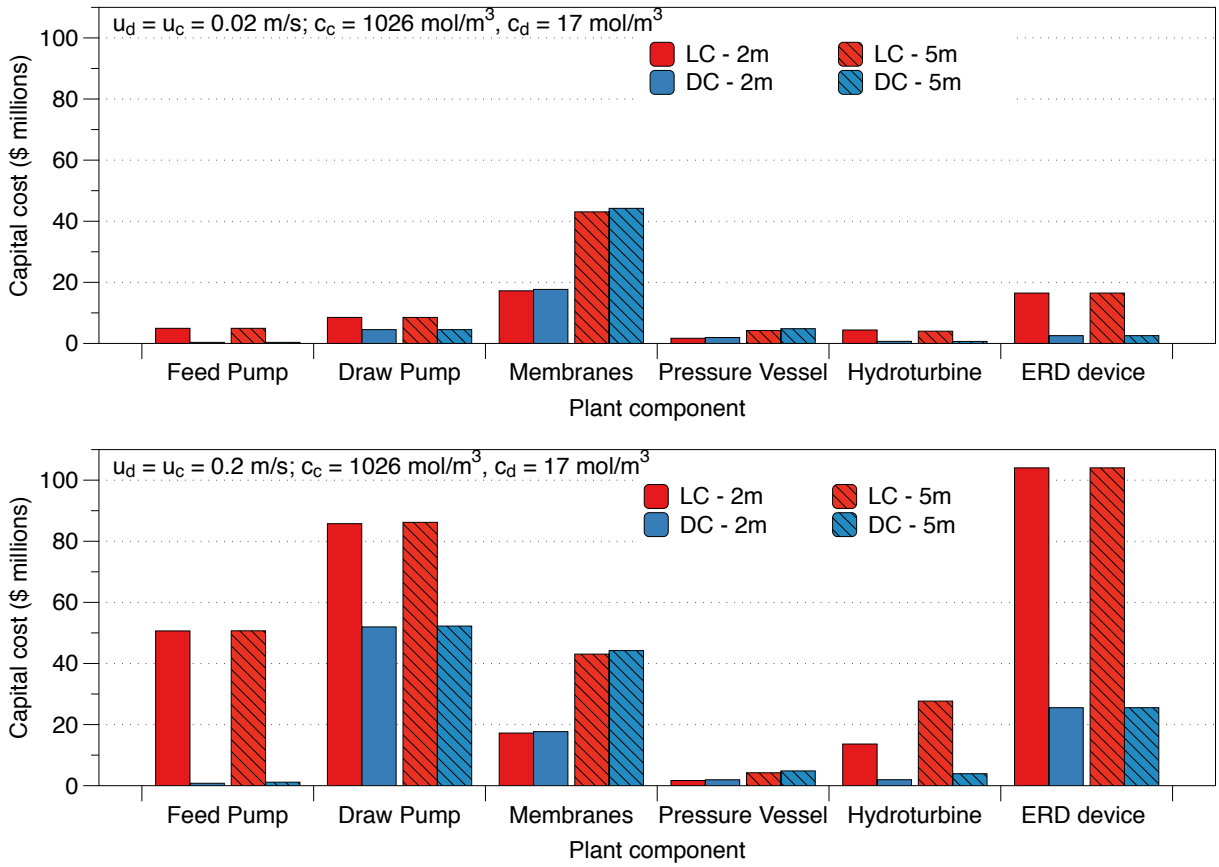

Figure 5.1 The cost of different plant components for two different crossflow velocities, (a) 0.02 m/s (top) and (b) 0.2 m/s (bottom), for two different system lengths (2 m and 5 m) when mixing RO brine with river water over a system length. Note the large change in pump, hydroturbine, and ERD device cost with higher crossflow velocity (i.e. flow rate).

When comparing the results for the LCs and DCs, it is clear that the biggest difference is in cost of the feed pump. This difference results from the way in which pump cost is calculated using each method. For the LCs, there is a base cost for each large pump, with additional cost arising from increased pressure demand (that is, $CC_{pump} = 393{,}000 + 10{,}710\,p$, for q = 450 m^3/h). The DCs calculate pump cost solely on the power required, i.e. the product of the pump pressure demand and pump flow rate demand. This results in a significant disparity in pump cost due to the very low pressure

required for the feed pump. The draw pump, on the other hand, does not exhibit such a pronounced difference using the two methods since the high pressure demand leads to high pump costs in both cases.

The cost of the ERD is significantly higher using the LCs. ERD cost will vary based on the type of technology employed as well as the device efficiency. Improvement in ERD performance over the last few decades has substantially reduced the cost of these devices. Still, the DCs applied in this study must be refined in order to fully capture the wide array of ERD models available.

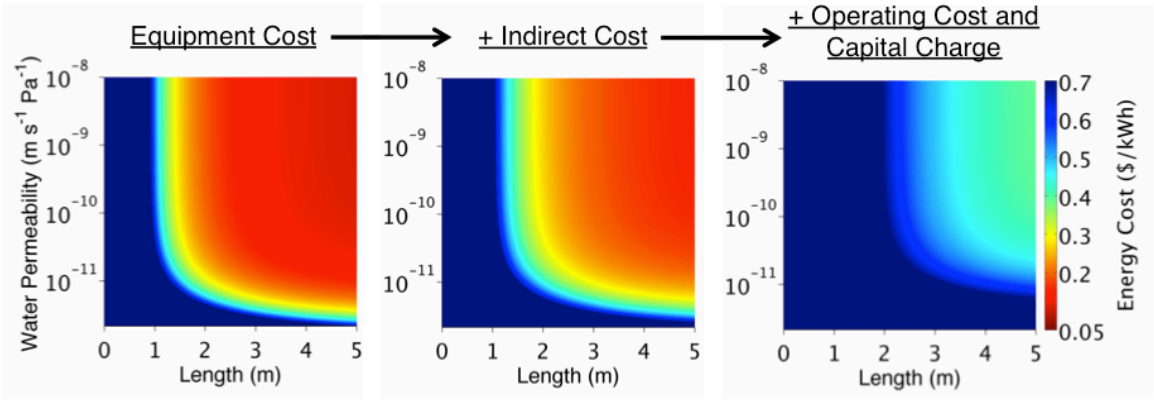

Figure 5.2 The change in cost along the system length for different membrane water (hydraulic) permeabilities, accounting for just the equipment cost, the equipment cost with indirect costs, and equipment cost with indirect costs, operating costs, and the capital charge and discounting over the life of the plant. The calculation is conducted for the Oasys TFC membrane (S = 434 microns, $B = 1.3 \times 10^{-7}$ m s^{-1}) at a crossflow velocity of u = 0.2 m/s, for brine-river water mixing.

Figure 5.2 shows how incorporating indirect cost and operating costs with capital charge significantly increases the cost of energy for the given mixing conditions (concentrated feed: 1026 mol/m^3, dilute feed: 17 mol/m^3, crossflow velocity = 0.2 m/s). At longer system lengths, where costs appear to be lowest, improvement in membrane water permeability beyond the current Oasys TFC value ($A = 9.56 \times 10^{-12}$ m s^{-1} Pa^{-1}) correlates with little equipment cost reduction. However, when incorporating additional costs,

improvement in water permeability has a clear impact. This effect is observed because any difference in equipment cost will be amplified once other costs are incorporated.

Figure 5.3 shows how changes in membrane water permeability (A) and structure factor (S) impact the minimum energy cost ($/kWh) for two different crossflow velocities and two different mixing regimes (brine-river water and seswater-river water). Here, minimum energy cost correlates to the lowest (positive) value for energy cost achieved over a total system length of 5 m. For different combinations of structure factor and permeability, this minimum value will occur at different system length. The modeling results show that, for both mixing regimes, a higher crossflow velocity (u = 0.2 m/s) leads to lower overall minimum energy cost. However, in the case of seawater-river water mixing, a low minimum energy cost can only be achieved at very low structure factor and high membrane hydraulic permeability. Therefore, if we assume the use of the current state-of-the-art Oasys TFC membrane, operating at the lower crossflow velocity (u = 0.02 m/s) is more practical than the higher crossflow velocity (u = 0.2 m/s). The same is true for brine-river water mixing, however it appears that minor improvement in membrane parameters will favor the higher velocity case. As expected, brine-river water mixing appears to be much more favorable than eawater-river water mixing.

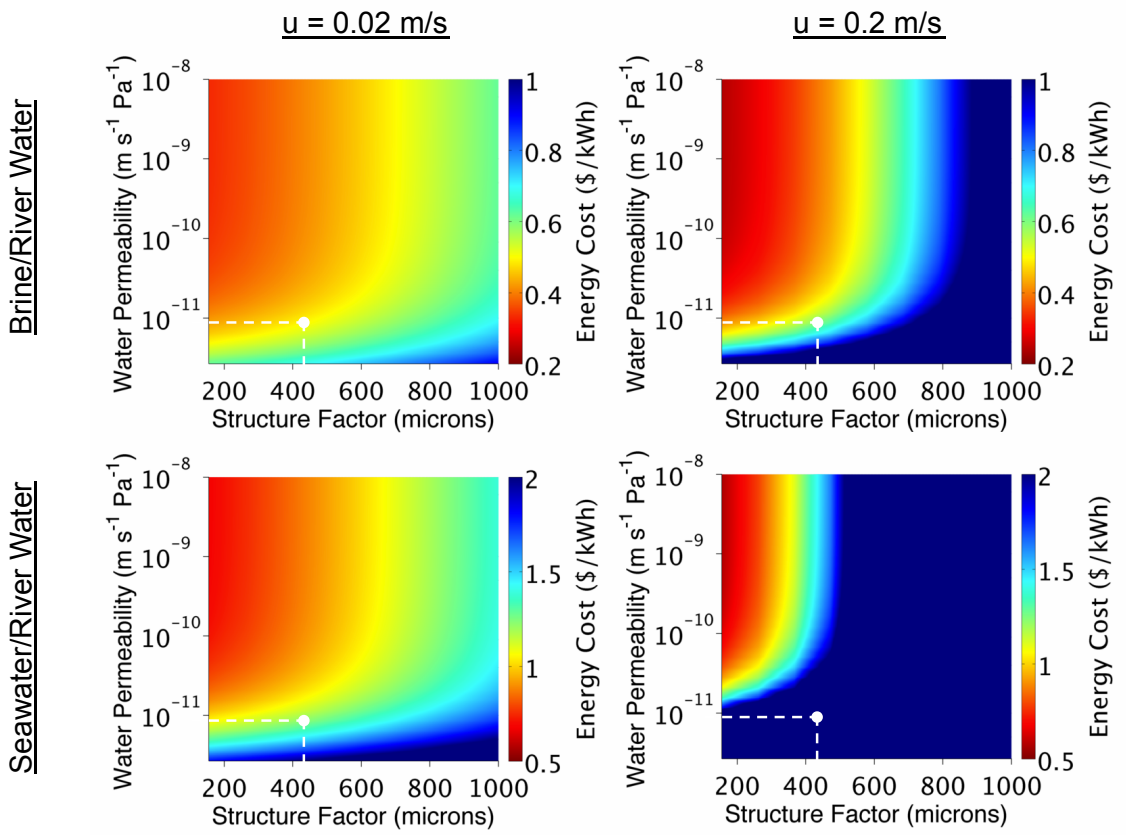

Figure 5.3 The minimum cost of energy ($/kWh) for four different mixing scenarios. The white mark on each plot denotes the properties of the Oasys TFC membrane. Note how a higher crossflow velocity corresponds a much faster increase in cost with increasing structure factor.

In **Figure 5.4**, the location for minimum energy cost along the module length is shown for brine-river water mixing at two different crossflow velocities. Note how the crossflow velocity significantly changes the location of minimum energy cost. A lower crossflow velocity correlates to a longer residence time, and thus, increased mixing over shorter lengths than a higher velocity case. While a higher velocity may lead to lower overall energy cost, it could require much more total membrane area.

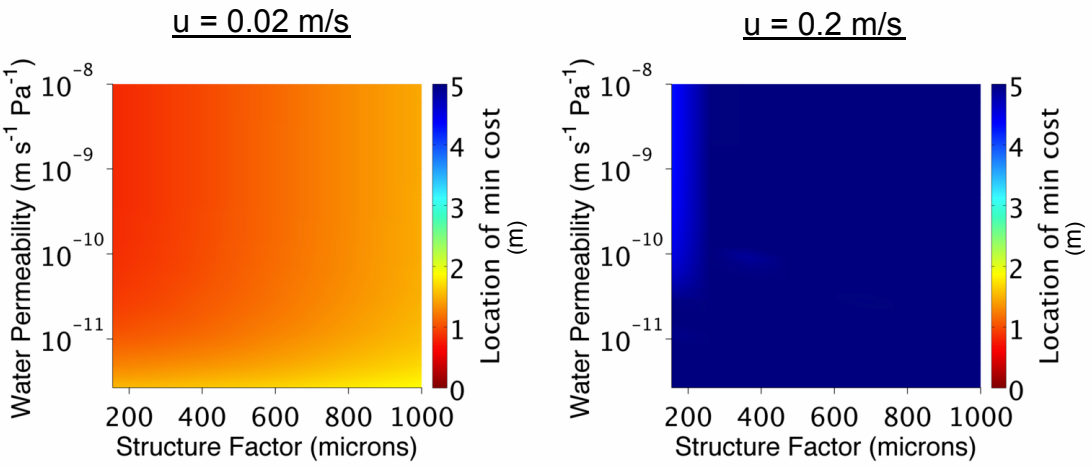

Figure 5.4 The change in the location of minimum energy cost along the system length for brine-river water mixing at two different crossflow velocities.

5.4 Conclusions

The work discussed in this chapter serves as a useful guide to the development of PRO. The most significant drivers of PRO plant cost have been highlighted, with draw (concentrated solution) pump cost representing the single largest contributor to the total capital cost. As system length increases, membrane cost becomes more contributory to the overall capital cost. As expected, brine-river water mixing corresponds to much more favorable economics than seawater-river water mixing. Change in velocity has a significant impact on energy cost, particularly for seawater-river water mixing, and reduction in membrane structure factor yields noticeably lower cost for all mixing scenarios. In light of the significant cost increases from incorporating operating costs, improvements in membrane water permeability are important for lowering energy cost.

The correlations used in this study are only an approximation of PRO cost. In actual practice, many more factors must be considered than those accounted for in this work. For

example, it has been shown that municipal and industrial application of RO can have significantly different costs depending on the relevant standards and codes. Furthermore, although the model discussed here accounts for varied cost based on the load through different plant components, some economics of scale may be neglected in this analysis. Thus, it is important to view these results within the appropriate context, and to continue to improve the model as new costing data, and costing methods, become available. Ultimately, the cost of PRO relative to other energy technologies, such as solar and wind, is the most important criterion in determining the feasibility of large-scale implementation of PRO.

5.5 References

[1] V.S. Sim, Q. She, T.H. Chong, C.Y. Tang, A.G. Fane, W.B. Krantz, Strategic Co-Location in a Hybrid Process Involving Desalination and Pressure Retarded Osmosis (PRO), Membranes, 3 (2013) 98-125.

[2] A. Malek, M. Hawlader, J. Ho, Design and economics of RO seawater desalination, Desalination, 105 (1996) 245-261.

[3] Y.-y. Lu, Y.-d. Hu, D.-m. Xu, L.-y. Wu, Optimum design of reverse osmosis seawater desalination system considering membrane cleaning and replacing, Journal of membrane science, 282 (2006) 7-13.

[4] L. Song, S. Hong, J. Hu, S. Ong, W. Ng, Simulations of full-scale reverse osmosis membrane process, Journal of environmental engineering, 128 (2002) 960-966.

[5] N. Wade, RO design optimisation, Desalination, 64 (1987) 3-16.

[6] G.W.I. (GWI), Desalination Markets 2010, (2010).

6 CONCLUSION

6.1 Conclusions and Future Work

In **Chapter 1**, an overview of SGP technology was provided, and the research hypothesis and objectives were outlined. Governing equations, mass transfer limitations, and current state-of-the-art technology were discussed in detail. Furthermore, a parametric study was conducted using the existing maximum power density models for PRO and RED in order to identify areas of potential improvement. The results of the study identified that module design, as opposed to membrane improvement, would result in the most meaningful enhancement in RED power density. For PRO, increased membrane water permeability correlated with significantly improved process. While maintaining salt rejection is an important consideration, a decrease in rejection can be tolerated if the membrane structure factor is concurrently reduced. Ultimately, although the power density models used in the study provided important insight, it was determined that a more robust analysis would be necessary to fully evaluate process performance.

Chapter 2 discussed both general thermodynamics of salinity gradient power as well as the potential for reduction in reverse osmosis specific energy consumption using osmotic energy recovery. In osmotic energy recovery, PRO or RED is placed before and/or after the desalination step. When placed before RO, PRO and RED serve to reduce the RO feed salinity, thus lowering the energy demand for desalination. Post-RO stage PRO or RED recovers energy from the mixing of high salinity brine with a lower salinity solution such as treated wastewater. The potential for energy savings using osmotic energy recovery is significant, with a coupled process possibly reducing the demand of seawater desalination to below the theoretical minimum for RO. However, since the analysis was purely thermodynamic, all losses (other than those that are configurational in nature) were ignored.

In **Chapter 3**, full-scale process models were developed for both PRO and RED to identify preferred operating conditions. The models provide an indication of the change in important process metrics such as power density and efficiency with system size. Importantly, energy recovery device efficiency was shown to limit PRO power density at full-scale, and lab-scale PRO cross-flow velocities were non-optimal for full-scale deployment. For both PRO and RED, optimal load factors identified in other literature were shown to be non-ideal for maximizing process performance. The developed models serve as valuable tools for process designers in scaling up salinity gradient power technologies in the future.

Chapter 4 applied the process model developed in the third chapter to a novel PRO process configuration. In this configuration, inter-module hydroturbines are placed between module segments in order to improve process performance. In effect, the pressure over the length of the system is modulated in order to increase the driving force across downstream segments. This staged configuration was shown to have significantly improved performance over the standard PRO configuration. In fact, staged PRO resulted in 47% higher efficiency than standard PRO for brine-river water mixing.

In **Chapter 5**, through the integration of process models with cost data, we have provided a simple analysis of PRO economics. Of course, as with all modeling work, the results are only an approximation of the real-world application of the technology. Developed cost correlations give dramatically different cost estimates than cost correlations derived from the academic literature. Using these correlations, the variation in energy cost with solution concentration and crossflow velocity has been highlighted. There appears to be value in improving both the membrane permeability and membrane structure factor in order to realize lower energy cost, however after some degree of improvement there is little benefit.

This work has focused on the power densities, efficiencies, and energy costs that can be theoretically achieved in PRO. Although we do produce a brief comparison with experimental data for PRO in **126,** future work should seek to validate the results discussed here over a wider range of operating conditions, as well as for the RED process. Furthermore, the novel process configuration discussed **Chapter 4** requires further investigation into the feasibility of the hydroturbine arrangement. As new module designs are proposed, modification of the existing model could serve as a useful tool for researchers and process designers.

While this work emphasizes how operating conditions contribute significantly to process performance, membrane and module improvement is also an extremely important research goal. In particular, improvement in PRO membrane water permeability and structure factor can be drive process cost much lower. Nevertheless, as shown in **Chapter 5,** at some point further improvement in some membrane properties has little impact on process performance. Membrane parameters not discussed here, such as chemical and physical stability, will also need to be further refined and developed if PRO and RED are to be economy viable.

APPENDIX A

A.1 Chapter 3 supporting information

A.1.1 Model validation

It is inherently difficult to compare the model results with data from other published reports because existing laboratory data is on a relatively small scale. That is, there is no literature data for a large-scale system (many meters) and thus we cannot compare our results in full. Although industrial companies such as Statkraft have developed pilot scale implementations of PRO, the performance data is not publicly available. Furthermore, available data for a 50-cell RED stack still constitutes a short system and does not approach the size of a full-scale implementation of RED [1].

For PRO, however, there does exist a recent publication reporting experiments on a 1 meter long PRO module [2]. Since there are some inherent geometrical differences between our modeled scenario and the experimental work (e.g., details of the spiral wound, U-shaped dilute feed path), a direct comparison between the two works is difficult. However, a comparison of the data is an extremely useful exercise, providing a general indication if model predictions are within a reasonable range of the experimental measurements.

In order to simulate the PRO module described in the literature by Kim et al, module geometry and membrane properties were taken from the paper directly or extrapolated from provided data. **Table A.1** lists the parameters used as input for the PRO model. The mass transfer correlation was taken from the literature, as outlined in the next section, however the pressure drop correlation used here was taken specifically for the Tricot permeate spacer used for the experimental PRO study. Since the PRO module comprises a U-shaped flow path for the dilute solution, the dilute solution crossflow velocity must be modified in order to account for the longer path length versus our simpler, plate-and-frame model. Therefore, the dilute solution

crossflow velocity (0.02 m s^{-1}) is divided by a factor of 2.45, since a single leaf is 0.725 m in width and the flow path comprises approximately two leaf widths and one leaf length. Of course, this approach is a rough approximation as there are inherent differences in mixing since our model assumes co-current mixing while the U-shaped path is a combination of co-current and cross-current mixing.

Figure A.1 shows the change in water flux with different trans-membrane pressure difference. The data shows that the water flux data from our model corresponds very well with the experimental data at lower applied pressures. In fact, the experimental data shows slightly higher water flux than the modeled data at the lowest pressure (0.3 bar) This disparity is likely the result of different flux resulting along the initial leg of the U-shaped flow channel due to the cross-current rather than co-current arrangement here. Interestingly, the difference between the modeling results and reported experimental data appears to become greater with increasing applied pressure. This behavior likely arises from the "shadow effect" discussed in the literature for PRO modules operating at higher pressure [2]. In effect, the high concentration solution pressure deforms the dilute solution channel dimensions, reducing the effective area for osmotic flux. Such effects cannot be accounted for in the process model presented here.

Table A.1 List of parameters for model validation.

Parameter	Value	Units	Given or Extrapolated?
Membrane hydraulic permeability (A)	2.22×10^{-12}	m s^{-1} Pa^{-1}	Extrapolated
Membrane salt permeability (B)	6.67×10^{-8}	m s^{-1}	Extrapolated
Concentrated (draw) channel height	800	microns	Given
Dilute (feed) channel height	400	microns	Given
Total membrane area	29	m^2	Given
Module length	1	m	Given
No. of leaves	20		Given
Width of each leaf	0.725	m	Extrapolated
Concentrated (draw) crossflow velocity	0.032	m s^{-1}	Extrapolated
Dilute (feed) crossflow velocity	0.020	m s^{-1}	Extrapolated
Concentrated (draw) NaCl concentration	597	mol m^{-3}	Given
Dilute (feed) NaCl concentration	1	mol m^{-3}	Given

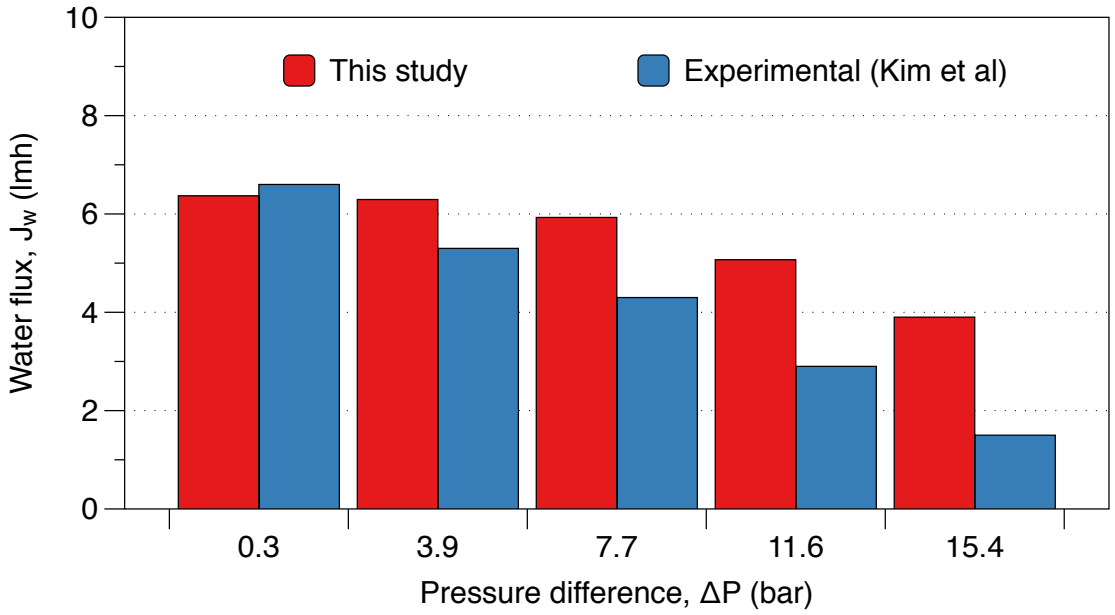

Figure A.1 Change in water flux with applied pressure difference for the model developed in this study and the experimental data for a 1 meter long PRO module.

A.1.2 Viscous dissipation – correlation for pressure drop

Many correlations, both empirically derived and produced from CFD modeling, have been proposed for viscous dissipation (i.e. pressure drop) in osmotic processes. These correlations, however, necessarily predict different dissipation depending on flow channel geometry and crossflow velocity. Some correlations (particularly those that are empirically derived) apply only over a certain range of Reynolds number. Thus, in formulating the process model used in this study, the selection of an appropriate correlation was thoughtfully considered.

Figure A.2 depicts the impact of pressure drop per unit length ($\Delta p/L$) versus the flow Reynolds number. The correlations extracted from a CFD study for reverse osmosis by Guillen et al [3] are shown for three different cases of spacer filament diameter to channel height, and apply for $10 < Re < 400$. Schock and Miquel (S+M) [4] presented numerous correlations for use in reverse osmosis, including a smooth channel (turbulent) and channels with different permeate and feed spacers (laminar). These correlations were empirically derived for approximately $100 < Re < 1000$ for the FilmTec feed spacer, and approximately $10 < Re < 100$ for the FilmTec permeate spacer. Finally, Koutsou et al [5] conducted a three dimensional CFD study, with experimental validation, for different spacer filament spacing (L/D) and flow orientations (β). The two cases correspond to the highest and lowest pressure drop cases in nine potential flow arrangements, and the authors showed good agreement with Schock and Miquel, with application over a slightly smaller range of Reynold numbers ($40 < Re < 400$).

It is clear that the case of turbulrnt flow in a smooth channel should not apply to the laminar flow regime modeled in this paper. Furthermore, the Koutsou case with large filament spacing ($L/D = 12$) may not be applicable here. For all other cases, there is very good agreement over the range of Reynolds numbers examined, particularly at $Re > 100$. Given the wider range

of applicability of the Guillen correlations at lower Reynolds number, and the similarity between the Guillen, Schock and Miquel, and Koutsou correlations at higher Reynolds numbers, the middle range Guillen case (i.e. $d_f/h_c = 0.5$) was chosen for the purposes of this study.

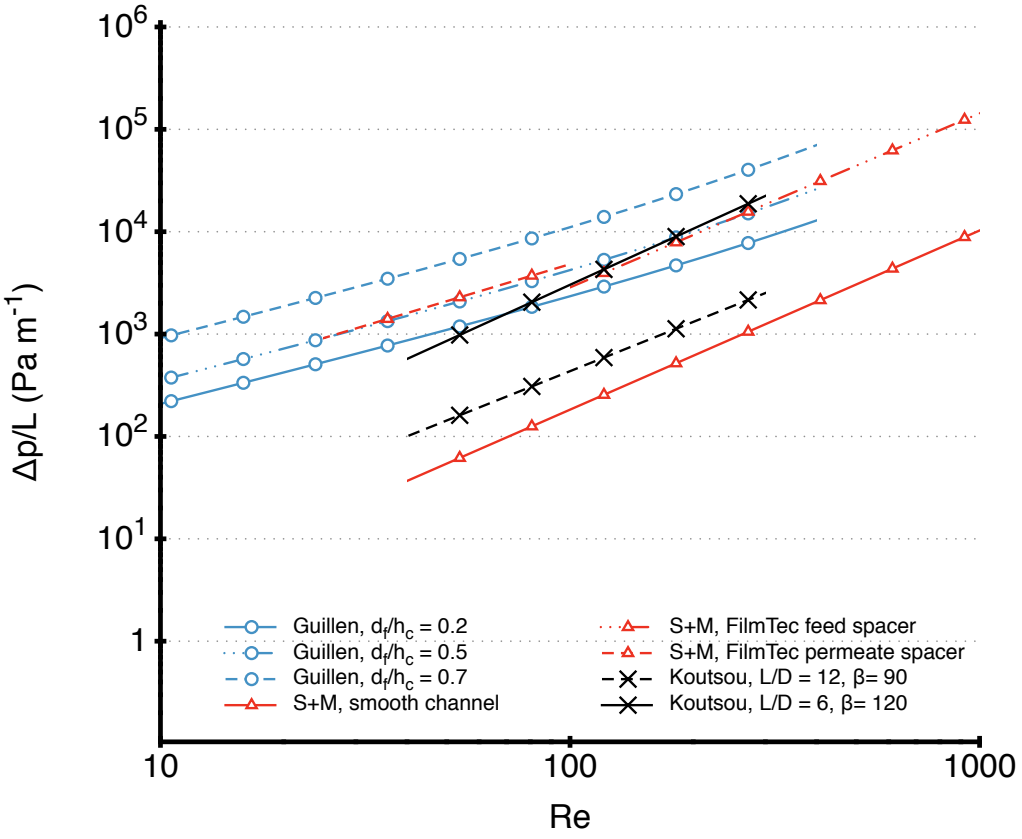

Figure A.2 Change in pressure drop scaled by system length (Δp/L) versus Reynolds number using different viscous dissipation correlations. For the Guillen correlations, d_f is the diameter of the spacer filament and h_c is the channel height. For Koutsou et al, L/D is the ratio of the modeled area length to the filament diameter, and β denoted flow orientation.

A.1.3 Mass transfer coefficient

Mass transfer correlations have been applied in order to determine the mass transfer coefficient (k) in the concentrated feed channel. As in the case of viscous dissipation, numerous correlations exist in the literature [3, 4]. Here we have evaluated the change in mass transfer coefficient with changing Reynolds number for three different cases (**Figure A.3**). We see that, as in the case of viscous dissipation, the Schock and Miquel and Guillen cases converge somewhat at higher

Reynolds number. Also, as with pressure drop, we do not consider the smooth channel (turbulent) regime to be an accurate representation of the flow conditions here. Since the Guillen correlation has greater applicability at lower Reynolds number, we apply it for the purposes of this study.

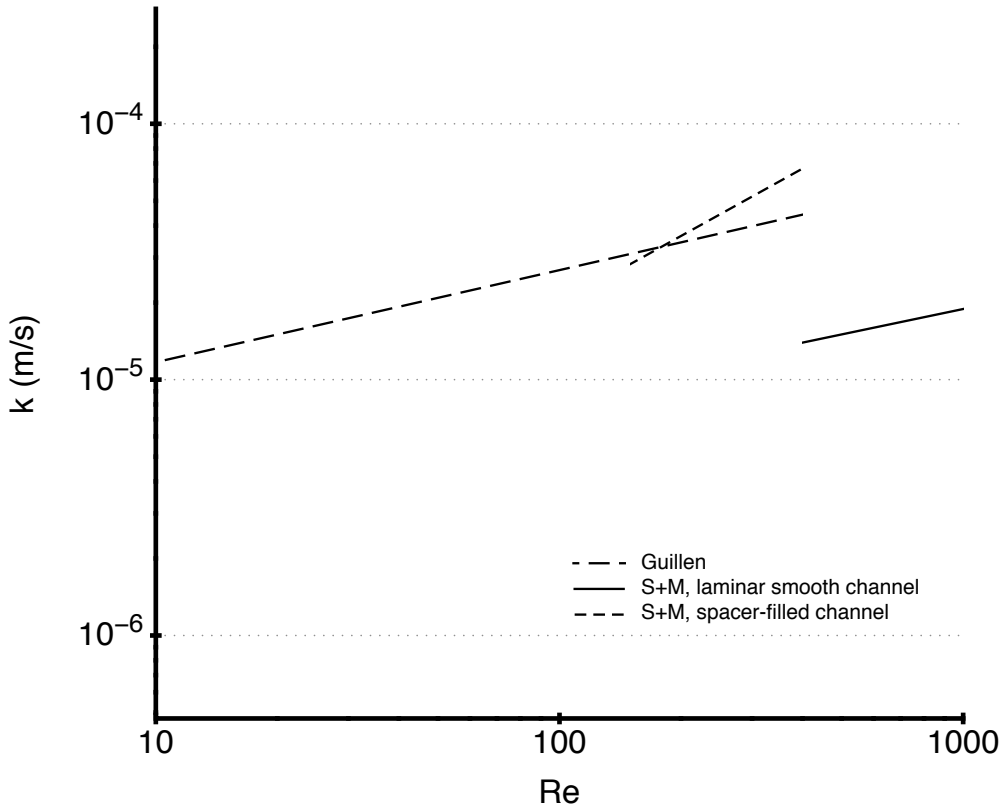

Figure A.3 Change in mass transfer coeffcient (k) with Reynolds number using different mass transfer correlations.

A.1.4 Accounting for non-ideality

As outlined in the main text, using published experimental data for the change in osmotic coefficient of water with concentration [6, 7], it is possible to construct a correlation to link with the existing mass transport model in order to account for non-ideality in the PRO osmotic pressure.

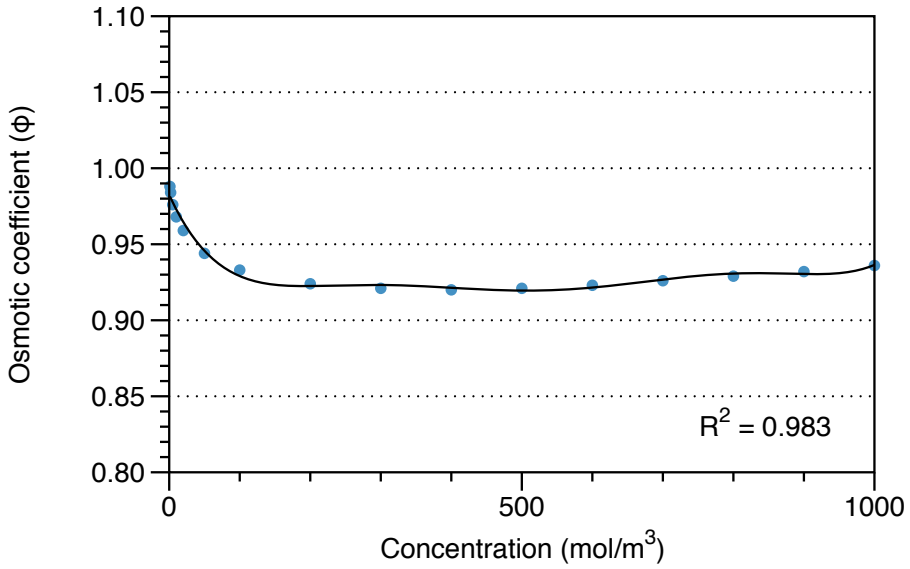

Figure A.4 Change in osmotic coefficient (ϕ) with concentration.

Figure A.4 depicts a sixth-order polynomial fit for the experimental data, where there is good agreement between the fit and the literature values (R^2 = 983). The exact correlation applied is

$$\begin{aligned}\phi = {} & 0.98244 - 0.0010176c + 6.6073\times10^{-6}c^2 \\ & - 2.078\times10^{-8}c^3 + 3.3387\times10^{-11}c^4 \\ & - 2.6244\times10^{-14}c^5 + 8.0018\times10^{-18}c^6\end{aligned} \tag{A.1}$$

and applies over the salinity range 1 mol/m^3< c <1000 mol/m^3. Although this range accounts for all mixing scenarios modeled in this paper, different correlations must be applied for salinities outside this range. We can then calculate the osmotic pressure of each feed using the membrane interface concentrations as described in the main text. Similarly, for RED, we account for non-ideality through the use of salt activity coefficients. The exact correlation applied is

$$\begin{aligned}\gamma = {} & 0.94248 - 0.0026202c + 1.1404\times10^{-5}c^2 \\ & - 2.3622\times10^{-8}c^3 + 2.2483\times10^{-11}c^4 - 7.9339\times10^{-15}c^5\end{aligned} \tag{A.2}$$

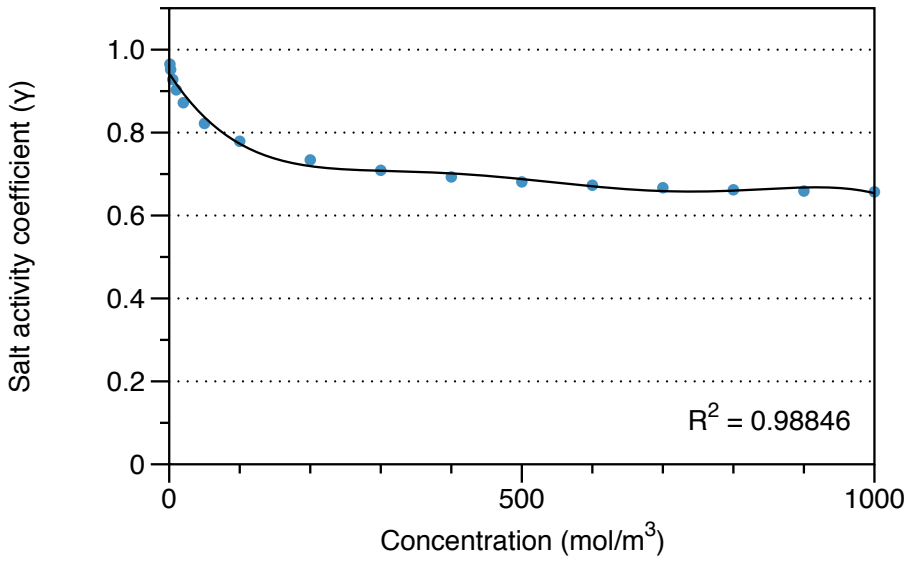

Figure A.5 Change in NaCl salt activity (γ) with concentration.

A.2 References

[1] J. Veerman, M. Saakes, S. Metz, G. Harmsen, Reverse electrodialysis: performance of a stack with 50 cells on the mixing of sea and river water, Journal of Membrane Science, 327 (2009) 136-144.

[2] Y.C. Kim, Y. Kim, D. Oh, K.H. Lee, Experimental Investigation of a Spiral-Wound Pressure-Retarded Osmosis Membrane Module for Osmotic Power Generation, Environmental Science & Technology, 47 (2013) 2966-2973.

[3] G. Guillen, E.M.V. Hoek, Modeling the impacts of feed spacer geometry on reverse osmosis and nanofiltration processes, Chemical Engineering Journal, 149 (2009) 221-231.

[4] G. Schock, A. Miquel, Mass transfer and pressure loss in spiral wound modules, Desalination, 64 (1987) 339-352.

[5] C.P. Koutsou, S.G. Yiantsios, A.J. Karabelas, Direct numerical simulation of flow in spacer-filled channels: Effect of spacer geometrical characteristics, Journal of Membrane Science, 291 (2007) 53-69.

[6] W.J. Hamer, Y.C. Wu, Osmotic Coefficients and Mean Activity Coefficients of Uni‐univalent Electrolytes in Water at 25° C, Journal of Physical and Chemical Reference Data, 1 (1972) 1047-1100.

[7] K.S. Pitzer, J.C. Peiper, R. Busey, Thermodynamic properties of aqueous sodium chloride solutions, Journal of Physical and Chemical Reference Data, 13 (1984) 1-102.